Atomic scale exploration of natural and self-assembled quantum structures

Citation for published version (APA):
Bocquel, J. (2013). *Atomic scale exploration of natural and self-assembled quantum structures*. [Phd Thesis 1 (Research TU/e / Graduation TU/e), Applied Physics and Science Education]. Technische Universiteit Eindhoven. https://doi.org/10.6100/IR762787

DOI:
10.6100/IR762787

Document status and date:
Published: 01/01/2013

Document Version:
Publisher’s PDF, also known as Version of Record (includes final page, issue and volume numbers)

Please check the document version of this publication:

• A submitted manuscript is the version of the article upon submission and before peer-review. There can be important differences between the submitted version and the official published version of record. People interested in the research are advised to contact the author for the final version of the publication, or visit the DOI to the publisher's website.
• The final author version and the galley proof are versions of the publication after peer review.
• The final published version features the final layout of the paper including the volume, issue and page numbers.

Link to publication

General rights
Copyright and moral rights for the publications made accessible in the public portal are retained by the authors and/or other copyright owners and it is a condition of accessing publications that users recognise and abide by the legal requirements associated with these rights.

- Users may download and print one copy of any publication from the public portal for the purpose of private study or research.
- You may not further distribute the material or use it for any profit-making activity or commercial gain
- You may freely distribute the URL identifying the publication in the public portal.

If the publication is distributed under the terms of Article 25fa of the Dutch Copyright Act, indicated by the “Taverne” license above, please follow below link for the End User Agreement:

www.tue.nl/taverne

Take down policy
If you believe that this document breaches copyright please contact us at:

openaccess@tue.nl

providing details and we will investigate your claim.

Download date: 05. Oct. 2023

Atomic scale exploration of natural and self-assembled quantum structures

PROEFSCHRIFT

ter verkrijging van de graad van doctor aan de
Technische Universiteit Eindhoven, op gezag van de
rector magnificus, prof.dr.ir. C.J. van Duijn, voor een
commissie aangewezen door het College voor
Promoties in het openbaar te verdedigen
op woensdag 4 december 2013 om 16.00 uur

door

Juanita Bocquel

geboren te Nantes, Frankrijk

Dit proefschrift is goedgekeurd door de promotoren en de samenstelling van de promotiecommissie is als volgt:

voorzitter: prof.dr.ir. G.M.W. Kroesen
1e promotor: prof.dr. P.M. Koenraad
2e promotor: prof.dr. Henri Mariette (Institut Néel Grenoble)
leden: prof.dr. M.E. Flatté (University of Iowa)
prof.dr. B.L. Gallagher (University of Nottingham)
dr. S. Sanguinetti (Politecnico di Milano)
prof.dr.ir. H.J.M. Swagten
prof.dr.ir. H.J.W. Zandvliet (University of Twente)

A catalogue record is available from the Eindhoven University of Technology Library.

Atomic scale exploration of natural and self-assembled quantum structures, by
Juanita Bocquel
ISBN: 978-94-6191-971-7

The work described in this thesis has been carried out in the group of Photonics and Semiconductor Nanophysics, at the Department of Applied Physics of the Eindhoven University of Technology, The Netherlands. The research leading to the presented results was carried out within the network SEMISPINET, and has received funding from the European Community's Seventh Framework Programme (FP7/2009-2012) under the grant agreement number PITN-GA-2008-215368.

Printed by Ipskamp Drukkers.

Cover: Anisotropic decrease in conductivity around a single Fe atom in GaAs.

Contents

chapter 1

Introduction

Over centuries, the human mind has been confronted with and challenged by the nature surrounding it. Necessity and curiosity led people to explore the natural world in order to gain knowledge, understanding and control. For a long time, this enterprise, first called natural philosophy, was confined to a small number of domains and remained the privilege of few individuals. As these studies became more systematic, natural science was born. Among all natural sciences, physics has ostensibly the widest scope, from infinitely large to infinitely small, from visible to invisible. Accordingly, some branches of physics are found at the intersection of several disciplines, as it is the case for condensed matter physics. At the boundaries of chemistry and material sciences, this large field of research is dedicated to the study of different states of matter and the physical laws governing them. Solid-state physics, in particular, studies the relation between the macroscopic and microscopic properties of solid materials. The investigation of the atomic scale properties of these materials is guided by a recent field in the history of physics: quantum physics. The understanding of microscopic properties is, for a large part, based on quantum mechanics, which has proven to be an extremely rich and robust framework. Developed at the beginning of the 20th century to explain a large number of experimental observations, quantum physics rapidly led to a complete description of the fundamental structure of matter and the associated interactions. This theory defines successfully atoms and their nucleus, molecular structures, conduction of electrons in solids as well as many others microscopic properties of matter. This revolution transformed the vision on fundamental processes at the atomic scale. From that point in history, quantum mechanics added a new dimension to both physics and chemistry, opening prospects of new applications.

In the last 50 years, quantum physics predicted numerous physical effects resulting in an unexpectedly large field of applications. As new ways of designing functional devices emerged, many technological sectors underwent major changes. More than ever, the driving forces behind today's scientific progress are for a large part aiming at changing the every day life of millions. Applied physics research is consequently carried out by a large number of scientists and engineers reaching a broader audience. Engineering materials from the atomic scale, where quantum physics account for most of the phenomena, to create specific macroscopic electronic, magnetic or thermal properties allows for a high versatility. In particular, giant technological steps have been achieved following the rapid development of semiconductor physics. As it turns out, semiconductor materials are flexible and versatile media, subject to numerous quantum effects and perfectly adapted to the perpetual scaling down of devices. New technologies based on quantum physical effects are in accord with the modern world of miniaturization, communication and information. Semiconductor devices are build from nanostructures displaying quantum mechanical properties which can also be referred to as quantum structures. In particular, quantum confinement effects, resulting in quantized or discrete energy levels in nanostructures, are of specific interest. Quantum confinement in a nano-object is typically determined by the dimensions of this object, which have to be comparable to the wave function of a discrete electronic state, *i.e.* approximately 10 nm or less.

The interest in fabricating and studying semiconductor quantum structures is manifold. Three specific reasons are described here.
i) Quantum confinement found in nanostructures is closely related to the macroscopic electronic and optical properties of nanostructures. The energetic position of the discrete levels determines for example the optical emission energy. It is now clear that the confinement is largely determined by the structural properties of the nanostructures, providing a dynamic way of creating specific optoelectronic functionalities. Lasers, first build in the 1960's, are an example of an early application making direct and intentional use of a quantum phenomenon, here the stimulated emission[1]. The first solid-state laser system exploited the energy levels related to transition metal impurities (Cr) in a sapphire crystal. Later, semiconducting laser diodes were developed where the optical emission was based first on p-n junction[2] but most importantly on heterostructures, like quantum wells[3], especially designed for this purpose. The range in optoelectronics applications of semiconductor quantum structures is very broad due to the large variety of semiconductors and doping impurities.
ii) The field of quantum computing and communication has been growing fast in the last 20 years due to the development of experimental tools operating at the nanoscale. A quantum system consisting of two discrete energy levels can be regarded as a potential qubit, the unit of quantum information. Among others, quantum dots[4] and single impurities in crystals[5] are potential hosts for the creation of qbits[6]. These two approaches and their limits are currently being extensively investigated[7]. Recent achievements include the demonstration of a two-qubit gate based on quantum dots[8], a single quantum dot hole qubit[9], the manipulation, the coherent storage of the electron spin[10] and the entanglement of N-vacancy centers[11] or a single-atom electron spin qubit in silicon[12].
iii) Last but not least, semiconductor quantum structures give the unique opportunity to explore new quantum phenomena. If quantum physics gives a united vision of the fundamentals of matter answering thereby many questions, a larger number of problems arise continuously. It is therefore important to have a way to not only verify past ideas but also test new physical hypotheses. Here again,

the diversity and tunability of semiconductor quantum structures provide the rich and flexible environment required for such investigations.

These three motivations share common challenges. One of the greatest and most fundamental is achieving a deep understanding along with a high control of growth of the material system. This includes predicting the energy associated with the different states and their relation to the environment or the possibility of integrating a large number quantum structures. In this respect, there are definite differences between self-assembled and natural quantum structures. Self-assembled nanostructures can be fabricated in great quantity and their properties are very flexible. This versatility is the result of the strong relation between the morphology and the energy levels associated with the quantum structure[13,14]. The down-side of this strong dependence is the difficulty in accurately reproducing a morphology. Consequently from one nanostructure to another, the optical or electronic properties may vary. On the contrary, a specific impurity in given semiconductor crystal gives rise to levels with the exact same energy. This is however only valid for impurities in pure bulk crystals. Interfaces between materials or with vacuum as well as any other change in electrostatic environment of these impurities are known to influence their energy levels. Besides, up to now the integration of a large number of individual impurities in a device remains challenging. Clearly, any prospective application based on such systems requires systematic studies of their organization and their interactions with the environment.

The work presented in this thesis aims at addressing these designated issues for natural and self-assembled quantum structures. In the case of self-assembled nanostructures, the relation between structural properties of nanostructures, like dimensions, chemical composition and interfaces and their conditions of assembly is investigated. The main goal is progressing towards homogenous and reproducible systems composed of several identical nanostructures. In the case of impurities in semiconductor crystals, the influence of electrostatic conditions on the electronic configuration of these dopants is investigated. The main challenge is to find the relation between the intrinsic properties of the impurities and their interactions with the environment.

The core of the investigations reported here were carried out at the atomic scale using Scanning Tunneling Microscopy (STM) and Spectroscopy (STS). This technique, representing by itself a direct application of a quantum effect called tunneling, is one of the most powerful tool developed to probe structures and single impurities at the nanoscale. STM and STS experiments were performed in cross-sectional geometry allowing the study of buried nanostructures and subsurface impurities. The principles of Scanning Tunneling Microscopy on semiconductor surfaces are presented in chapter 1 and the applied experimental techniques are presented in chapter 2. The rest of the thesis is divided in three exhaustive chapters dedicated to different quantum systems, addressing thereby different questions.

A natural quantum system is presented consisting of single Fe atoms in GaAs in chapter 3. The main reasons for studying this particular system are the core spin of Fe impurities and the large binding energy of their acceptor level. Transition metals like Cr, Mn or Fe have partially filled *d*-shells, an attractive characteristic along the line of learning more about magnetic interactions at the atomic scale. Traditionally, transition metals are incorporated in semiconductors materials for one of the following reasons. They bring localized magnetic moments in the crystals which may interact and give rise to ferromagnetism. Several mechanisms are proposed, like carrier-mediated ferromagnetism[15]. Fe impurities in GaAs were found to interact antiferromatically and therefore do not represent of system of interest in the field of diluted magnetic semiconductors. Transition metals atoms are also found in semiconductors materials in order to give them a semi-insulating properties. Transitions metals impurities introduce deep levels in the bandgap of most semiconductors which act as charge traps[16]. The most common cases are Cr impurities in GaAs or Fe impurities in InP which are available as commercial wafers. Similarly, Fe impurities in GaAs reduce the conductivity. That being said, the main motivation for studying Fe in GaAs remains the exploration of fundamental physical processes. So far, only relatively shallow dopants have been investigated by STM and STS. Until now, Mn dopants in GaAs, with a binding energy of 113 meV, were the deepest dopants studied with these techniques. Their spatially distribution but also the spatial structure of their acceptor wave function were determined[17]. Despite a higher binding energy, it appears from the X-STM studies that the Mn acceptor state has, like shallow acceptors, a relatively strong host-like character. Fe dopants in GaAs, with a binding energy of 510 meV, are the first deep and subsurface impurities for which an impurity-like character is expected. Another difference with previous studies is the multivalent character of Fe acceptors in GaAs. This system represents therefore an opportunity to establish the relation between a large binding energy and higher localization of the impurity states and the possibility a electronic or magnetic manipulation of these states. Besides, the manipulation of a single Fe impurity falls into the scope of the emerging field of solotronics. In this chapter, it is shown that a dilute distribution of the Fe impurities allows for imaging and manipulating the core d-states of a single Fe impurity. The electronic manipulation of the Fe states leads to STM observations similar to those on shallower dopants. Interestingly however, it was determined that the initial and final state not only have different charge states but also different valence states and spins. Furthermore, the crystal field split states of e and t_2 symmetry of the $3d$-states of a single Fe impurity in GaAs were imaged by means of spatially resolved STS. Additionally, evidence of internal transitions involving those core states are shown which are supported by theoretical predictions.

In chapter 5 and chapter 6, two different self-assembled quantum systems are presented. These semiconductor nanostructures were grown by Molecular Beam Epitaxy. The two type of structures differ by the dimensionality of the quantum confinement pursed as well as by the material system: quantum dots in III-V semiconductors in the first case and multiple quantum wells in II-VI semiconductors in the second case. The study of self-assembled GaAs strain-free quantum dots in AlGaAs is presented in chapter 5. The major reason for investigating this specific structures is finding and assessing a reproducible method to grow quantum dots with specific optical emission. The conventional Stranski-Krastanov growth method can not be used here because GaAs and AlGaAs are lattice matched materials. Instead a more recent epitaxial technique is used called Droplet Epitaxy.

Droplet Epitaxy is based on the kinetically limited processes of crystallization and diffusion[18]. Consequently, a large number of degrees of freedom are available. This method has led to fabrication of a large variety of nanostructures like quantum dots, disc and rings[19–24]. The absence of strain in GaAs/AlGaAs heterostructures is an particularly interesting characteristic considering that strain can not only shift the position of the energy levels in a quantum dot but also strongly influences the quantum dot formation. The systematic study reported here shows the change in morphology of the strain-free GaAs/AlGaAs quantum dots as a function of several growth parameters, like crystallization temperature, As flux and volume of Ga deposited. The experimental results are in good agreement with the analytical model proposed based on Ga diffusion dynamics and crystallization during the exposure of the Ga liquid droplet to the As flux. Furthermore, the chemical composition and the interfaces of these quantum dots is analysed in detail, giving insights in the crystallization process and its limitations. Finally an effort has been made to achieve the precise height control of these GaAs/AlGaAs quantum dots by engineering the capping layer. The method used for that purpose, called flushing, resulted in a very promising and high control over the quantum dot height.

The investigations by STM of II-VI semiconductor structures are presented in chapter 6. The initial interest in analysis II-VI nanostructures was to study the incorporation of Mn impurities inside CdTe quantum dots. This system has been investigated thoroughly by means of optical spectroscopy but lacks the structural characterization at the nanoscale[25]. Unfortunately, II-VI semiconductors turned out to be difficult to prepare for cross-sectional STM measurements. CdTe quantum dots were imaged poorly preventing any useful observations. In this chapter, this exotic class of semiconductors which are the selenium and tellurium based II-VI semiconductors is first presented. Then, a study of the p-type doping of ZnTe achieved by introducing N atoms is presented, which was meant as first step towards the study of Mn doping of ZnTe. The complete absence of segregation or diffusion of N atoms incorporated in ZnTe in a temperature range of 300°C to 360°C is reported. However, the creation of a large number of point defects along with the incorporation of N in ZnTe was also revealed, which will strongly affect the electrical and transport properties of N-doped ZnTe crystals. Finally, a full study of CdSe/ZnTe and CdSe/ZnCdTe multiple quantum wells is presented, focusing on the quality of the interfaces between the selenide and telluride compounds. These specific systems are fabricated for their optoelectronic properties. The type-II band alignment expected in these multiple quantum wells structures should allow for the efficient absorption of light in a tunable energy range[26]. This prospect are however dependent on the quality of the heterostructures and in particular of the interfaces. From these STM studies presented here, it clearly appears that the growth conditions of CdSe determine the structural quality of the interfaces which do not share common anions or cations. The interfaces of the CdSe/ZnTe MQW with CdSe grown under excess of Cd appeared to be sharp and well-defined within one bilayer. On the contrary, the CdSe/ZnCdTe interfaces grown under excess of Se are not abrupt. Consequently, it is suggested that the growth conditions for CdSe should be chosen according to the desired functionality of the heterostructure.

chapter 2

Scanning Tunneling Microscopy on semiconductors

This chapter presents an introduction to Scanning Tunneling Microscopy (STM) on semiconductor surfaces. The physical process behind STM and its theoretical framework are introduced. Emphasis is put on specifically relevant aspects of STM on semiconductor systems, like the phenomenon called Tip Induced Band Bending (TIBB). The different contributions to the STM signal are outlined in order to explain the chemical sensitivity of the technique, necessary to investigate the structural properties of nanostructures. Wave-function imaging mechanisms and I(V)-spectroscopy required to study the electronic structure and properties of single dopants are described.

2.1 STM principles

2.1.1 Theoretical background of tunneling

Scanning Tunneling microscopy (STM) is a experimental technique invented in 1981 by Binning and Rohrer[27,28]. This invention came as a response to a growing demand of physicists and chemists to be able to investigate phenomena at the atomic scale. The development of this powerful tool, awarded by a Nobel prize in 1986, came long after theoretical predictions of such capabilities had been formulated. STM is based on the detection of the tunneling current between a metallic tip and conductive surface with a high spatial resolution. Its experimental implementation required to overcome technical challenges like the ability to control the tip position and motion with an extremely high accuracy. This difficulties were solved by the development of piezoelectric ceramic materials, like lead zirconate titanate (PZT,) as well as advances in noise isolation. The working principle of an STM setup is presented in Fig. 2.1.

The STM junction consists in two conductive materials separated by a vacuum barrier, as schematically illustrated in Fig. 2.2. Electron conduction through

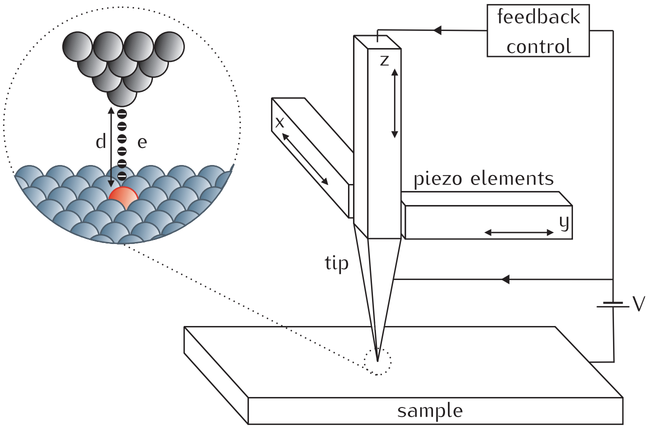

Figure 2.1: Working principle of a Scanning Tunneling Microscope. A feedback loop keeps the tunnel current constant by adjusting the tip height. The x, y and z displacement of the tip are controlled by piezoelements.

a classically forbidden potential barrier is not allowed. However, if the energy barrier is reduced, e.g. by reducing its height or width, the system falls into the domain of quantum mechanics and there exists a probability for electrons to tunnel from a conductive material to the other. This ability of the electrons to tunnel through an finite potential barrier originates from the aptitude of electrons wave function to penetrate the potential barrier. The fraction of electrons tunneling through this barrier is given by the transmission coefficient T which depends on the barrier height ϕ and width d. In one dimension, it is approximated by:

$$T \propto e^{-2d}\sqrt{\frac{2m_e}{\hbar^2}(\phi - E)} \tag{2.1}$$

with m_e the electron mass and E its energy[29]. The transmission coefficient depends exponentially on the barrier width.

STM exploits this concept of quantum mechanical tunneling to achieve a high spatial resolution. A metallic tip is brought in close proximity to the conductive surface, ≈ 1 nm, and a bias voltage is applied between the two. The magnitude of the electron tunneling process is there determined by the spatial overlap between the two-dimensional sample surface states and the state of the atom at the tip apex. The description of a real tunnel junction in a quantitative fashion has been the object of many studies. However, this problem remains particularly complex as interactions between tip and sample have to be taken into account.

The tunneling process is described here within the one-dimensional formalism established by Bardeen[30]. Bardeen's equation gives the tunnel current I over the STM junction:

$$I = \frac{2\pi e}{\hbar}\sum_{s,t}\left[f_t(E_t) - f_s(E_s + eV)\right]\left|M_{s,t}\right|^2 \delta(E_t - E_s), \tag{2.2}$$

where s and t refer respectively to the sample and the tip. V represents the voltage applied between the sample and the tip, e the electron charge. eV is the difference between the sample $E_{F,s}$ and tip $E_{F,t}$ Fermi levels. f is the Fermi distribution function. M is the tunneling matrix element describing the effect of the barrier on the tunneling process. M determined by the overlap between the wave function of the tip apex state Ψ_t and the surfaces states Ψ_s of the sample at energies E_t and E_s respectively, described by :

$$M_{s,t} = \frac{\hbar}{2m_e} \int_S (\Psi_s^* \Delta \Psi_t)(\Psi_t \Delta \Psi_s^*) d\vec{S}, \tag{2.3}$$

with m_e the free electron mass and S a surface in the vacuum barrier between tip and sample.

Reasonable approximations can be made which reflect the experimental application of equation 2.2 and allow a simpler physical description of tunneling process.

- In the limit of low temperatures and small bias voltages, the Fermi functions can be considered as step functions:

$$I = \frac{2\pi e^2 V}{\hbar} \sum_{s,t} |M_{s,t}|^2 \, \delta(E_s - E_{F,s}) \delta(E_t - E_{F,t}), \tag{2.4}$$

- Within the Tersoff-Hamann model, the metallic tip is considered as a point-like probe at a position r on the sample surface[31,32]. The tip state is described as a localized s type wave function with a relatively flat density of states near the Fermi energy. Consequently, the tip LDOS is approximated as a constant over energy and the matrix element is proportional to the state of the sample Ψ_s. In those conditions, the current is:

$$I(r, V) \propto \rho_t(E_{F,t}) \sum_s |\Psi_s| \, \delta(E_s - E_{F,s}), \tag{2.5}$$

  where the quantity on the right can be defined the sample local density of states at the Fermi energy $\rho_{s,E_{F,s}}$.

This relation however only holds for small applied voltages and this condition is not respected in the case of STM on semiconductors. In this case, the modified Bardeen's formula is used[33].

$$I = \frac{4\pi e}{\hbar} \int_0^{eV} \rho_s(E_{F,s} - eV + \epsilon) \times \rho_t(E_{F,t} + \epsilon) \, |M|^2 \, d\epsilon, \tag{2.6}$$

- An additional simplification is to only consider tunneling between sample and tip states of same energy, e.g. elastic tunneling is considered. The initial and final states have equivalent tunneling probabilities and the matrix element M, constant in energy, is given by:

$$|M|^2 = exp(-2\kappa d), \tag{2.7}$$

where d is the distance between sample and tip and κ is the inverse decay length of the wave function in the classical forbidden vacuum barrier given by:

$$\kappa = \frac{\sqrt{2m_e\phi}}{\hbar}, \tag{2.8}$$

with m_e the free electron mass and ϕ the effective barrier height (considered independent from bias voltage). κ has a typical value of 1×10^{10} corresponding to one order of magnitude variation in the tunnel current for 0.1 nm variation in the tip-sample distance and is considered as approximately constant in time and space.

Under all the above mentioned assumptions, equation 2.2 reduces to

$$I \propto \int_0^{eV} \rho_s(E_{F,s} - eV + \epsilon) exp(-2\kappa d) d\epsilon, \tag{2.9}$$

Finally,

$$I \propto exp(-2\kappa d), \tag{2.10}$$

implies that keeping the tunnel current constant, while scanning over the surface by adjusting the distance d between tip and sample, results in recording an atomically resolved surface of constant LDOS.

2.1.2 (110) surfaces of III-V and II-VI semiconductors

The experiments presented in this thesis were performed on cleaved III-V and II-VI semiconductor compounds. This STM approach is known as cross-sectional STM where the surface of interest is obtained by cleaving the semiconductor crystals along their natural cleavage plane. In the case of zinc-blende III-V and II-VI semiconductor compounds, it has been shown that the natural cleavage planes are the non-polar (110) and $(1\bar{1}0)$ orthogonal planes. The (110) plane consists of zigzag rows of alternating cations and anions in equal number along the $[1\bar{1}0]$ direction, as illustrated in Fig. 2.3. The $(1\bar{1}0)$ present the same arrangement with reverse symmetry. These surfaces show a 1 × 1 reconstruction. To reach thermodynamical stability, the atoms at the surface relax[34,35]. The relaxation consists almost exclusively in a bond rotation leading to buckled surface bonds. Bond length remains almost unchanged and the dimensions of the unit cell are not affected[36–38]. As in bulk, the distance between the rows of the (110) surface are equal to a lattice constant a along the [001] direction and to $a\sqrt{2}$ along $[1\bar{1}0]$ direction. The displacement of cations and anions respectively inwards and outward lower the surface energy, as illustrated in Fig. 2.4.

Consequently, the states associated with the two dangling bonds per unit cell of the cleaved surface are driven out of the semiconductor band gap. The

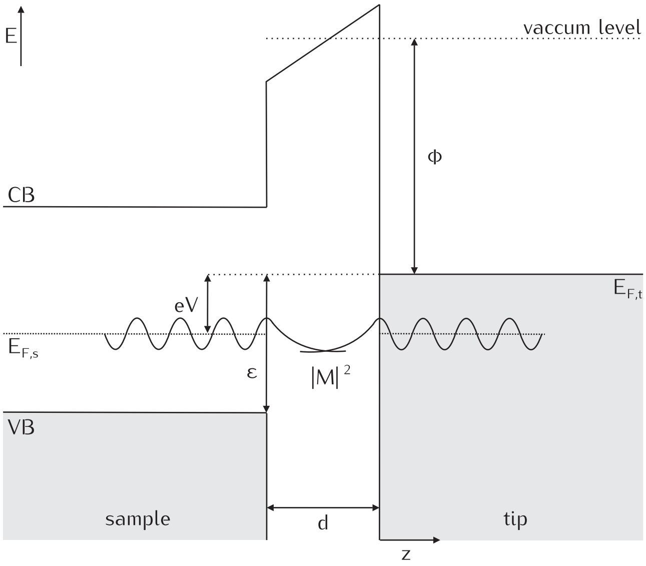

Figure 2.2: Schematic energy band diagram for the tip-sample system. At positive voltage, electrons tunnel from the tip to empty tip states through a barrier with height Φ and and width d. The overlap and decay of the tip and sample wave function are schematically indicated by the tunneling matrix element $|M|^2$.

absence of surface states in the bandgap of (110) and $(1\bar{1}0)$ surfaces make possible the probe of the LDOS of subsurface defects. The Fermi level is therefore not pinned at the surface but determined solely by the bulk doping of the crystal[39,40]. Furthermore the top of valence band consists of p-like A_5 filled states localized on the anion sites, while the bottom of conduction band consists of s-like C_3 empty states localized on the cation sites. This configuration gives a bias dependent chemical sensitivity, where different sub-lattices are imaged depending on the voltage polarity. Tunneling at positive bias voltages correspond to the injection of electron in the empty states and the topographic image reflects therefore the LDOS of the cation sites. Tunneling at negative bias voltages corresponds to the extraction of electron from the sample filled states and the topographic image reflects therefore the LDOS at the anion sites. An example of this chemical sensitivity of the STM is shown in the empty and filled states topography images in Fig. 2.4. The clean atomic lattice of GaAs is resolved which gives an excellent calibration source for the x and y scanner piezo-elements. The type of corrugation that is visible depends strongly on the states involved in the tunneling process and therefore strongly depends on the bias voltage[41]. Along the [001] direction, bilayers are resolved and the spacing between the rows of anions or cations is equal to a lattice constant.

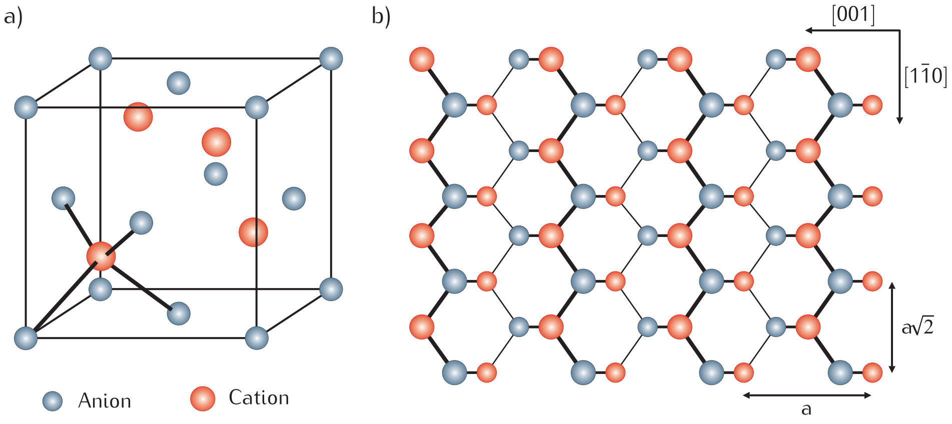

Figure 2.3: a) Zinc-blende crystal structure of the III-V and II-VI semiconductors compounds investigated in this thesis. b) Schematic top view of the (1$\bar{1}$0) cleavage plane. The anion and cation site are respectively in blue and red. a represents the lattice constant of the semiconductor crystal.

2.1.3 Tip Induced Band Bending

An inherent effect of the close proximity between the the sample surface and the metallic tip during STM measurements is the creation of an electric field across the tunnel junction. This electric field arises from the initial energy difference between sample and tip Fermi levels relative to the vacuum level, e.g. the electron affinity χ and the tip work function Ψ_t respectively. In response charge carriers in the sample (free carriers, ionized impurities) shield the electric field by creating space charge regions near the surface. This phenomenon is of major importance for STM measurements on semiconductor surfaces. The lower density of states in semiconductors compared to metals results in larger screening regions. Those regions correspond to an effective bending of the conduction and valence band of the semiconductor near the surface in order to align sample and tip Fermi level. This effect is called tip-induced band bending (TIBB). The configuration where semiconductor and metal are in physical contact is called a Schottky barrier. The presence of space charge regions modifies considerably the carrier distribution close to the sample surface making them extremely relevant for STM as they can significantly change the width of the tunneling junction. The spatial extent and the magnitude of the TIBB depend mainly on the doping level of the semiconductor material, the tip-sample distance, the polarity and the magnitude of the bias voltage. For carrier concentrations in the range of $10^{17} - 10^{19}\,\text{cm}^{-3}$, the spatial extent is isotropic and in the order of tens of nanometers, as schematically illustrated in Fig. 2.5a[42]. The TIBB correspond to an electrostatic potential located at the semiconductor directly below the tip. At given tunneling conditions and doping level, variations are explained by influence of the tip geometry.

Applying a voltage between tip and sample changes the electric field and further affects the band bending. At the so-called flat band voltage V_{FB}, the initial

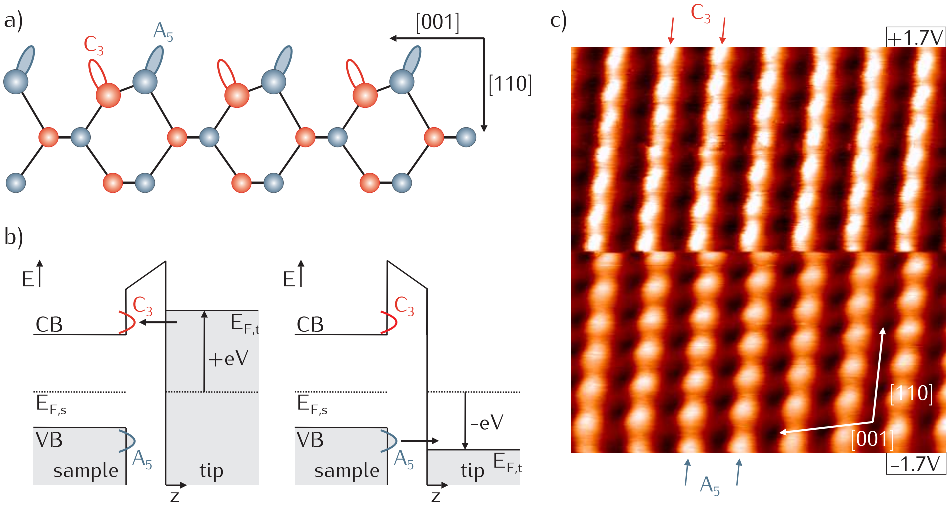

Figure 2.4: a) Schematic side view of the $(1\bar{1}0)$ cleavage plane. Cations and anions in the top most layer are relaxed and the adjacent bonds are buckled. b) Schematic energy band diagram for the tip-sample system for different voltage polarity. The surface states C_3 and A_5 respectively associated with the dangling bonds of cations and anions are found outside of the fundamental bandgap. The flow of electrons is indicated by arrows. c) 4 nm × 5.5 nm filled states (V=-1.7 V),nm and empty states (V=+1.7 V) topographic image of the (110) plane of GaAs. At negative voltage, the anion sub-lattice is imaged. At positive voltage, the cation sub-lattice is imaged.

TIBB is perfectly counteracted as illustrated in Fig. 2.5b. The nature of the TIBB varies with the type of doping, applied bias voltage polarity and amplitude. For voltages above and below V_{FB}, bands are bent upwards and downwards respectively. Depending on the applied voltage, accumulation, depletion, or inversion regions can be created which affect the tunneling process at different voltage windows. Different TIBB configurations are presented in Fig. 2.5c–f for the case of an intrinsically doped semiconductor sample. Fig. 2.5d and f show accumulation layers obtained for high bias voltage at both polarities, when the conduction band or valence band is pulled across the Fermi level and leads to an accumulation of respectively electrons or holes under the tip. The presence of these free charges results in additional tunneling channels. Fig. 2.5c and e show depletion layers obtained for low applied bias voltage at both polarities. Consequently, the width of the tunneling barrier is increased by this local decrease of free charge carrier density. Inversion layers, not depicted here, are accumulation layers resulting in an inversion of the majority and minority carriers close to the surface. In other words, n-type semiconductors locally exhibit an accumulation of holes while p-type semiconductors locally exhibit an accumulation of electrons.

TIBB affects significantly STM measurements on III-V and II-VI semiconductors surfaces by inducing a strong and complex dependence of the tunneling conditions on the bias voltage. Among others, the presence of space charge re-

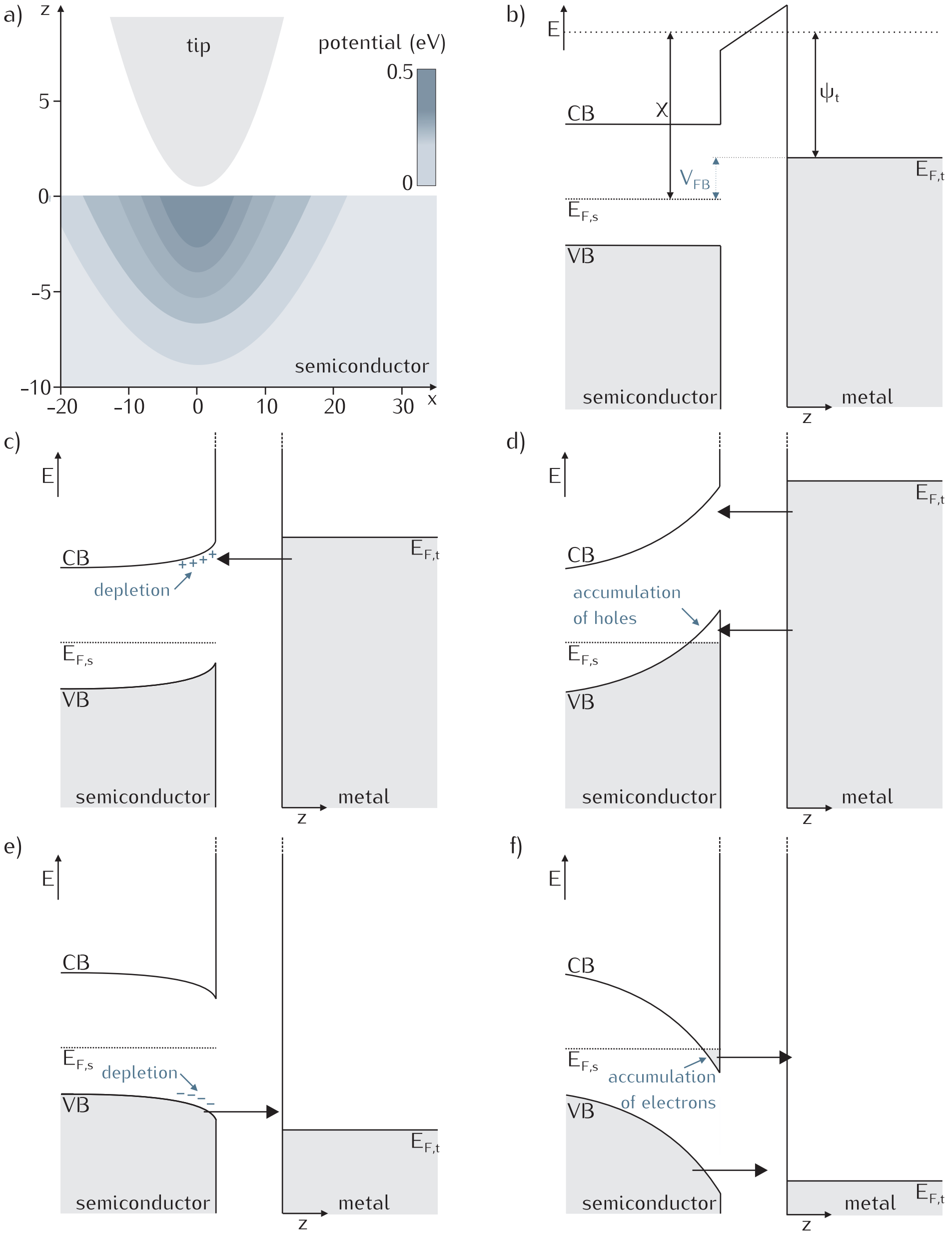

Figure 2.5: a) Schematic illustration of the spatial extension and magnitude of the TIBB for the doping levels and tunneling conditions of the experiments reported in this thesis. Different TIBB configurations are presented for an intrinsically doped semiconductor sample and different applied bias voltages. b) Flat band conditions. The applied voltage V_{FB} counteracts exactly the initial TIBB. Low voltages result in a depletion of free charge carriers, c) holes and e) electrons, close the surface. High voltages result in an accumulation or inversion of free charge carriers, d) electrons and f) holes, close the surface.

gions shifts the band onsets and give rise to an apparent semiconductor bandgap larger than the bulk value. Furthermore, TIBB changes the electrostatic environment of impurities and consequently shifts the corresponding energy levels. The TIBB magnitude is difficult to calculate as it derives from several estimated parameters. However, the trends observed in the experiments as well as the relative numbers are typically reflected correctly.

2.2 Imaging nanostructures

X-STM is a powerful technique to investigate self-assembled nanostructures, like quantum dots, quantum wells and superlattices. The atomic resolution provides important properties such as dimensions and morphology with great accuracy. The structural characterization of heterostructures is made possible by the chemical sensitivity of the STM technique. Determining the chemical composition is however not straight-forward and requires careful analysis as well as prerequisite knowledge about the material properties. The contrast obtained by STM has two origins. Standard images are acquired at constant current by adjusting the height of the tip while scanning. The STM image is a map of the tip height variation. The contrast reflects therefore the actual topography of the surface as well as the variation in LDOS as stated in earlier in this chapter. Both electronic and topographic components play a role when determining the characteristics of nanostructures, interface roughness or chemical fluctuations.

2.2.1 Electronic contrast

The first contribution to the STM contrast discussed here is the electronic contribution, as the surface is generally atomically flat. The bulk states of the semiconductor located between E_F and $E_F + eV$ participate to the tunneling current. The variation in band alignments across the semiconductor heterostructures influence the tunnel current, e.g. the electronic contrast. In a first consideration, the conduction (CBO) and valence (VBO) band offsets determine the difference in the amount of states available for tunneling from one material to the other. The CBO and VBO are determined by the chemical composition of the crystals. A general trend is that, common cations crystals have a small CBO while common anions materials have a small VBO. Materials with a large number of states available for tunneling appear brighter in the STM images. Semiconductors with a small bandgap appear typically brighter at both bias voltage polarities, proving that the band alignment is type I as shown in Fig. 2.6. In case of a type II band alignment, the contrast switches when changing the bias voltage polarity. The amplitude of the electronic contrast depends however significantly on effects related to the magnitude and the polarity of the applied bias voltage. The general rules mentioned above are modulated by the exponential decay of the tunneling probability with the effective barrier height as described by the transmission coefficient and indicated in red in Fig. 2.6. As presented in equation 2.1, in vacuum the penetration of the states decreases at lower energy. The higher energy states experience a smaller effective barrier and therefore contribute stronger to

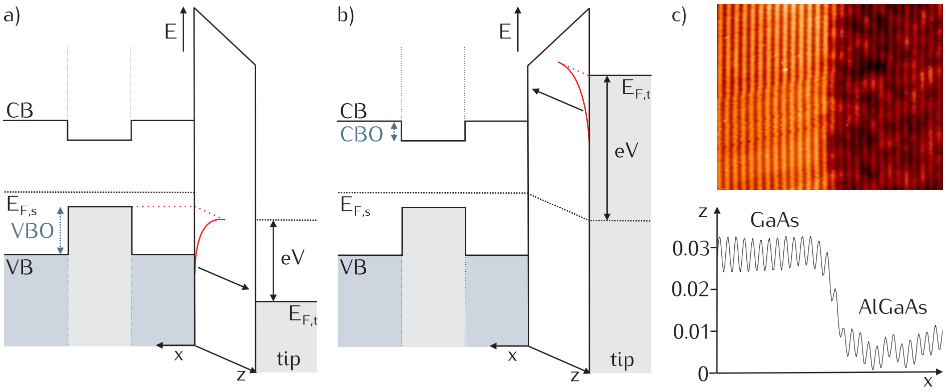

Figure 2.6: Energy band diagram for tunneling at a) negative and b) positive applied voltage. The conduction and valence band offset are indicated by the blue arrows. The exponential decay of the tunneling probability with the effective barrier height is depicted in red. c) 16 nm×14 nm filled states images of the interface between GaAs and AlGaAs and the corresponding height profile. The contrast arises from VBO between the materials.

the tunnel current. This is particularly important at positive bias voltages, as the sensitivity to the bottom of the conduction band is greatly diminished. This way, the CBO between materials is less apparent. The highest contrast is then obtained by using relatively low positive bias voltage. At negative sample voltages however, the exponential decay enhances the differences in VBO, as most of the tunneling occurs at the top of the valence band.

2.2.2 Strain relaxation

All embedded nanostructures are investigated in cross-section by cleaving the semiconductor crystal along one of their (110) or (1$\bar{1}$0) planes. The topographic component of the contrast plays a role in case of strained heterostructures made of crystals with different lattice parameters grown epitaxially. In that case the cleaved surface relaxes at the position where the crystal is under tensile or compressive strain, as illustrated in Fig. 2.7. The nature and the extent of the relaxation, outwards or inwards, depends on the sign and the magnitude of the lattice mismatch between crystals. The relaxation scales with the lattice mismatch. The lattice parameters of binary crystals are known and in the case of alloys scale with their chemical composition, according to Vegard's law. This allows to indirectly determine the chemical composition profile of these nanostructures.

Once the relaxation of the surface across the nanostructure has been experimentally determined corrected with calibration, it can be compared to the outcome of calculations based continuum elasticity theory[43] to establish the chemical composition profile. The calculations require prerequisite knowledge about the binary semiconductors crystals, like lattice parameters, Young modulus, Poisson ratio and thermal expansion coefficient. The dimensions and the morphology

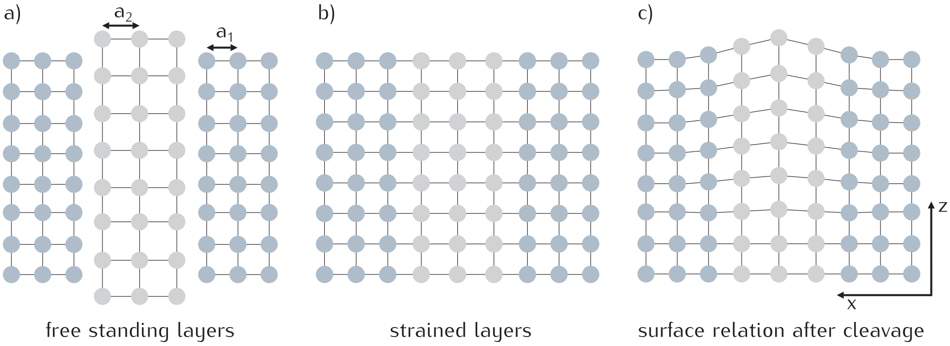

Figure 2.7: Side view of the compressive strain relaxation at the cleaved surface.

of the nanostructures are used to make a model which is subsequently used as an input for the calculation. The only variable is the chemical profile, which is determined when a reasonable fit is found between experimental and calculated profiles. The finite element calculations are performed within MEMS module of the software package COMSOL Multiphysics. For accurate measurement of the surface relaxation, the tunneling conditions must be chosen carefully in order to suppress the electronic component of the contrast. Following the arguments mentioned earlier, this is typically achieved for high applied bias voltages. Finally the composition profile extracted with this method can be compared to the profiles based on the direct measurement of the spacing between rows of atoms in the raw STM images and if the resolution allows, the direct counting of the atoms of different elements[44].

2.3 Studying impurities

In addition to nanostructure characterization, STM measurements can probe the local density of states (LDOS) around dopants and defects. Those measurements are not restricted to atoms at the surface, but are extended to subsurface dopants up to 10 monolayers below the surface. Measurements of dopants and other defects in III-V semiconductors have been extensively performed and reported by several groups since the 1990s[45–47].

2.3.1 Shallow dopants

Dopants with binding energies lower than 35 meV are typically referred to as shallow. Those dopants are normally introduced in semiconductors materials in order to tune their electronic properties. Shallow centers can be thermally activated, adding extra charge carriers in the semiconductor crystals. As a consequence they have drawn a lot of interest and have been widely studied. The following subsections described the state of the art in imaging shallow dopants by X-STM.

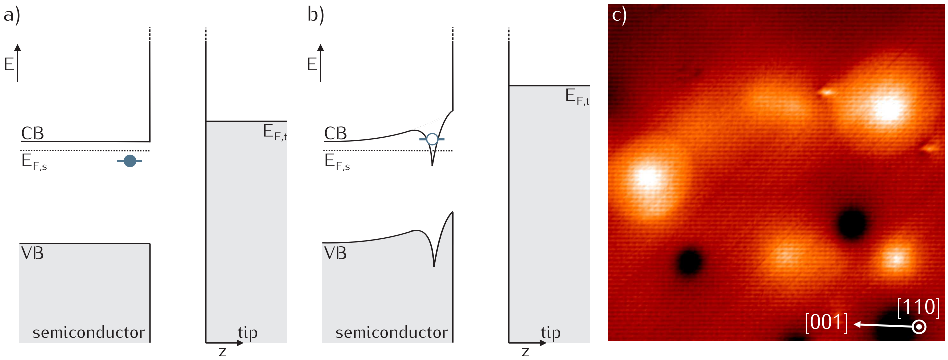

Figure 2.8: Ionization of single Si donors in GaAs by the STM tip at positive applied bias voltages a) At low voltages, the donor is in its neutral state. b) At higher voltages, the donor is brought in its ionized state resulting in the presence of a Coulomb field and additional states available for tunneling. c) 28 nm×28 nm empty state image (V=+0.5 V, i=70 pA) of Si atoms in GaAs. Signature of this ionization process in the empty states images of Si-doped GaAs. A bright disc which sharp edges appears around each ionized Si impurity.

2.3.1.1 Donors

A donor is an atom with more valence electrons than the atom it substitutes for in the crystal. For doping levels in the range of $10^{18} - 10^{19}\,\mathrm{cm}^{-3}$, donors bring the Fermi level of the bulk semiconductor very close to the conduction band edge. Popular donors in III-V semiconductor compounds are Te, Sn or Si with binding energies around 6 meV[48,49]. Si has the particularity to be an amphoteric atom but for concentrations below $10^{19}\,\mathrm{cm}^{-3}$ it substitutes mainly for cations and acts as a donor. The electronic configuration of donors is mainly studied at positive applied bias voltage. At low temperatures the charge state of single shallow donors can be manipulated, as shown for Si in GaAs. This is achieved by changing the electrostatic environment of the impurities by tuning the TIBB. As explained earlier, varying the magnitude of the applied voltage, as depicted in Fig. 2.8, is an efficient way to change the TIBB. Alternatively, the tip-sample distance can be adjusted (by changing the current setpoint) . At low voltages, the energy level associated with the donor is found below the Fermi level (Fig. 2.8a). The donor is in its neutral state and a very localized bright contrast is visible. When applying a large positive voltage, this level, following the bending of the bands, can be pulled above the Fermi level and above the conduction band edge in the bulk. In that configuration, the additional electron escapes in the conduction band resulting in the ionization of the donor center. The positive charge remaining on the donor center induces an isotropic Coulomb field locally enhancing the number the states available for tunneling (Fig. 2.8b). The signature of this ionization process in the empty states images of Si-doped GaAs is the presence of a bright disc around each ionized Si impurity, as shown in Fig. 2.8c. The sharp edges of the disc correspond to the distance at which

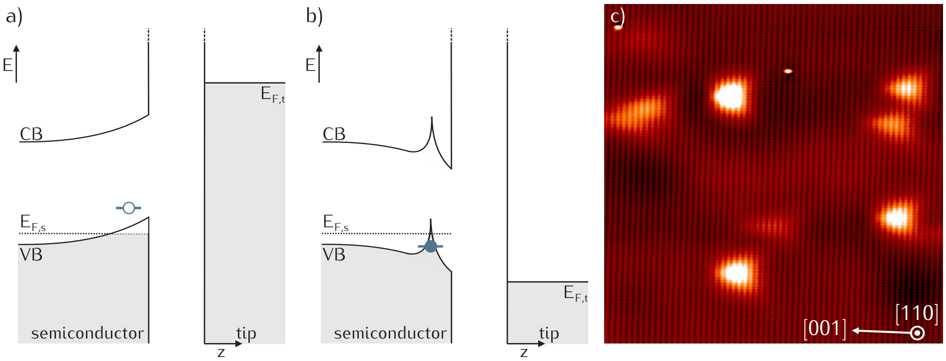

Figure 2.9: Wave function imaging mechanism for holes bound to single acceptors. a) At positive voltage, the acceptor is in its neutral state. Electrons can be injected in acceptor level thereby mapping the wave function of the bound hole b) At negative voltage, the acceptor is brought in its ionized state resulting in the presence of a Coulomb field and additional states available for tunneling. c) 33 nm×33 nm empty state image (V=+1.55 V, i=150 pA) showing the wave function of holes bound to C dopants in GaAs (bright triangular contrasts).

the TIBB is sufficient to align the donor level with the bulk conduction band edge[50]. The dependence of this process on different tunneling parameters has been extensively studied and allowed insightful discoveries on the behavior of Si dopants, like the enhancement of their binding energy close to the surface[51].

2.3.1.2 Acceptors

An acceptor is an atom with less valence electrons than the atom it substitutes for in the crystal. For doping levels in the range of $10^{18} - 10^{19}$ cm^{-3}, acceptors bring the Fermi level of the bulk semiconductor very close to the valence band edge. Popular acceptors in III-V semiconductor compounds are Zn, Be or C with binding energies around 25–30 meV. The electronic configuration of acceptors depends on the polarity of the applied bias voltage. It was shown that changing the polarity of the voltage results in the manipulation of the charge state of single acceptors. Here again, it originates from the change of the electrostatic environment of the impurities by TIBB. At positive voltage, the energy level associated with the acceptor is found above the Fermi level (Fig. 2.9a). The acceptor is in its neutral state and electrons can be injected in the level thereby giving an image of the wave function associated with the bound hole. The anisotropic wave function of holes bound to C atoms in GaAs are shown in Fig. 2.9c. At negative voltages, the acceptor level is pulled downwards along with the semiconductor bands, crossing the Fermi level and aligning with the top of the valence band in the bulk. In that configuration, an electron can populate the acceptor state resulting in the ionization of the acceptor. The negative charge remaining on the acceptor center induces an isotropic Coulomb field locally enhancing the number the states available for tunneling (Fig. 2.9b). Ionization discs in filled states images have not

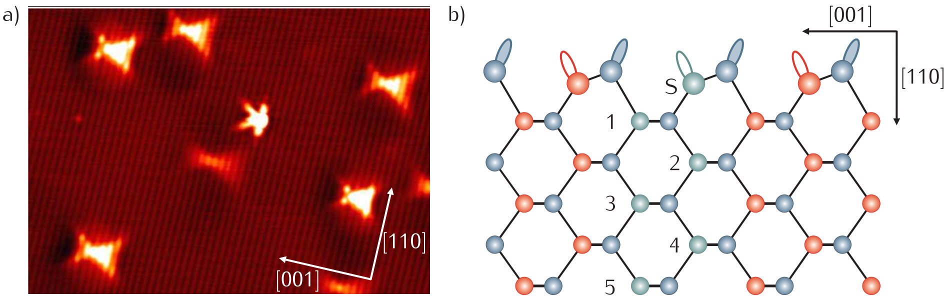

Figure 2.10: a) 6 nm×6 nm empty states images of Mn-doped GaAs[56]. The bright anisotropic features are wave functions images of holes bound to the Mn^{2+} ions. b) Schematic side view of the $(1\bar{1}0)$ cleavage plane. Possible positions for Mn^{2+} ions are highlighted in green. Each position correspond to a different asymmetry of the bound hole wave function as shown in a).

been reported for shallow acceptors yet. The reason seems to be the initial flat band conditions. At low negative voltage, the impurities are ionized at distances larger than the scale of typical STM images. A large number of studies on shallow acceptors in III-V semiconductors by X-STM have been done, mainly focusing on understanding the anisotropy of the bound hole wave functions and its dependance on the tunneling conditions[52–54].

2.3.2 Deep dopants

The intentional doping of III-V semiconductors with deep impurities is fairly restrained. In general, such dopants are used to give semi-insulating properties to the semiconductor crystals, as they behave as deep hole or electron traps. Deep defects have been the center of attention in the 1980's. Only from the late 1990's, the interest in dilute magnetic semiconductors has been reviving the attention on deep acceptors like transitions metals (TM) in III-V and II-VI semiconductors. TM impurities in III-V semiconductors have been investigated thoroughly in the perspective of understanding the mechanisms behind the resulting ferromagnetism and its limits. X-STM brought insights in that field by determining not only the distribution of those dopants in the crystal but also by mapping the wave functions of single deep transition metal acceptors[17]. Additionally the interactions between dopants pairs were investigated[17,55].

The most studied system was undoubtedly Mn-doped GaAs for it had the highest prospect of room temperature ferromagnetism. Among all TM, Mn dopants in III-V semiconductors have a privileged place, stemming from the electronic configuration of the free atom. A Mn has the [Ar] $4d^2$ $3d^5$ electronic configuration. Like most TM, Mn substitutes for cations in III-V semiconductors, that is Ga in GaAs. To perfectly replace a Ga atom, Mn has to give away 3 electrons, becoming the isoelectronic Mn^{3+}, $3d^4$. This configuration is however energetically less favorable than the Mn^{2+} configuration with a $3d^5$ half-filled d shell. It has been demonstrated that Mn indeed incorporate at the acceptor Mn^{2+} with a bound

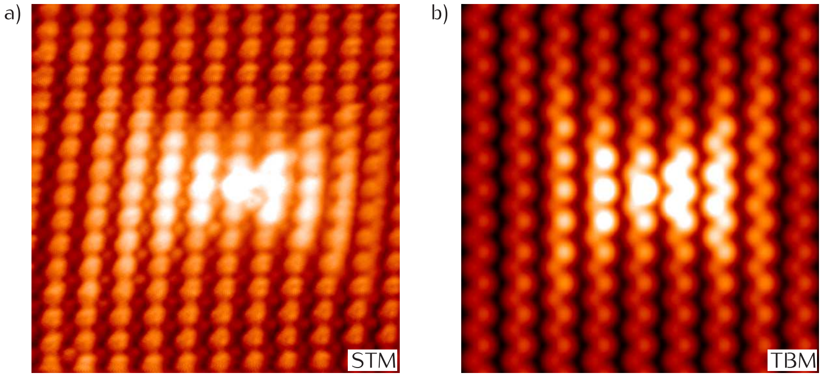

Figure 2.11: a) Empty states images of a single Mn^{2+} acceptor in GaAs[17]. The symmetry indicates that the Mn^{2+} ion located 5 ML below the surface b) Tight Binding calculation of the LDOS of a Mn^{2+} ion located 5 ML below the surface.

hole h^+. The binding energy of this hole is 113 meV. This complex has a 5/2 core spin interacting antiferromagnetically with the bound hole that is responsible for carrier mediated ferromagnetism.

This $Mn^{2+} + h^+$ complexes in GaAs have been seen by X-STM as illustrated in the empty-states image of Fig. 2.10a. It is worth noting that Mn^{2+} ions can be ionized in the same manner as shallow dopants by tunneling at negative applied bias voltages. The shape of the deep acceptor wave function is found to be highly anisotropic and asymmetric . In first considerations, the cubic symmetry of the semiconductor host and the nature of the hole ground state are responsible for the observed anisotropy. The asymmetry along the [110] direction is related to the asymmetry of the buckled surface and is reversed when imaging the (110) or $(1\bar{1}0)$ planes[57]. For this reason the variation in asymmetry of the features related to Mn^{2+} ions in Fig. 2.10a is attributed to the difference in their position (distance) below the cleaved surface[56] (Fig. 2.10b) . It had been shown that Mn^{2+} ions can be detected up to 10 monolayers below the surface. Among many others, studies have been carried on in an effort to understand the relation between the acceptor binding energy and the anisotropy of the wave function.

It is important to underline the crucial and decisive role of theory in determining the origin of the anisotropy and its variations, as well as the asymmetry of deep acceptors. Theoretical approaches include variety of methods like envelop function effective mass model, atomistic tight-binding model and density functional theory. Along the years, this vast enterprise resulted in an increasing match between experimental observations and theory[17,58]. A good example of these accomplishments is shown in Fig. 2.11.

2.3.3 I-(V)Spectroscopy

An powerful extension of STM is the I(V)-spectroscopy or Scanning Tunnel Spectroscopy (STS)[59]. It can directly address the LDOS at a specific voltage while

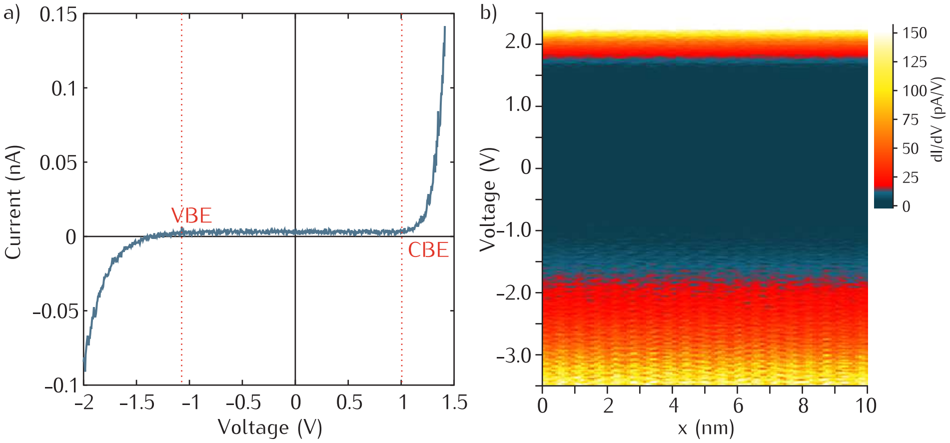

Figure 2.12: a) Example of an I(V) curve taken on semi-insulating GaAs. The band edges are indicated in red. b) Example of an 10 nm long $dI/dV(x,V)$ cross-section taken along the [001] direction on semi-insulating GaAs. The large apparent bandgap is the result of TIBB in low doped semiconductors.

with standard STM the current is integrated over the large energy windows between E_F and $E_F + eV$. Single I(V) curves are performed at a specific position by sweeping the voltage and recording the current variation (see Fig. 2.12a). During this procedure, the feedback loop is switched off and the tip stays at the same distance from the surface. This is an efficient way to learn about the electronic structure of dopants. When a discrete energy level is addressed, the resulting tunneling channel induces a peak in the measured I(V) curve at a specific voltage. Spatially resolved I(V)-spectroscopy is obtained by acquiring an I(V) curve at every pixel of the STM image.

The LDOS at a specific energies is accessible by numerically taking the derivative of an I(V) curve. Under the approximations mentioned earlier, the relation between the differential tunneling conductance dI/dV and LDOS is given by the derivative of Eq. 2.9:

$$\frac{dI}{dV} \propto \rho_s(E_{F,s} - eV)exp(-2\kappa d). \tag{2.11}$$

It is possible to visualize the variation in LDOS along a line and in maps, giving the spatial distribution of acceptor and donor related states at the atomic scale. An example of an 10 nm long $dI/dV(x,V)$ cross-section taken along the [001] direction on semi-insulating GaAs in displayed in Fig. 2.12b. The slight oscillations of the LDOS in the valence band is due to the corrugation of the surface. In this thesis, LDOS cross-sections and maps have been acquired on single Fe impurities in GaAs as presented in chapter 4.

chapter 3

Experimental techniques

The main investigations presented in this thesis were done by means of cross-sectional scanning tunneling microscopy (X-STM) and spectroscopy experiments. X-STM refers to STM experiments carried out on cross-section planes of the sample of interest. The (110) and ($1\bar{1}0$) planes are the natural cleavage planes of zinc-blende semiconductors. This geometry allows the study of embedded nanostructures and dopants. This approach requires a specific sample preparation while the tip preparation and the STM setups are standard among the broader STM community. This chapter presents the behind the scenes of X-STM experiments.

3.1 STM setup

Two Omicron STM setups were used which are operated at different temperatures: room-temperature and low temperature (77 or 5 K) depending on the cryogenics used LN_2 or LHe). Both setups are UHV setups combining 3 separated chambers at different pressures. The loading chambers are at $p \approx 5 \times 10^{-7}$ mbar, the preparation chamber at $p \approx 5 \times 10^{-10}$ mbar, and the STM chamber at $p \approx 2 \times 10^{-11}$ mbar. This very low pressure in the STM is required in order to protect the cleaved surfaces from contaminants. At room-temperature, this conditions allows typically for two consecutive days of measurements, while at low-temperature, the additional cryo-pumping allows for several weeks of measurement on the same surface. Those low pressures are obtained by a combination of turbo-molecular pumps and ion getter pumps. The latter are the only pumps operational during the vibration sensitive STM experiments. Mechanical noise is further reduced by springs, an internal eddy-current damping stage, an active damping platform and the location of the setup on an island decoupled from the building. The room-temperature STM setup has a simpler design than the low-temperature STM setup. Both are equipped with the essential tools to finalize *in-situ* the preparation of samples and tips: a heater and an Ar ion sputtering

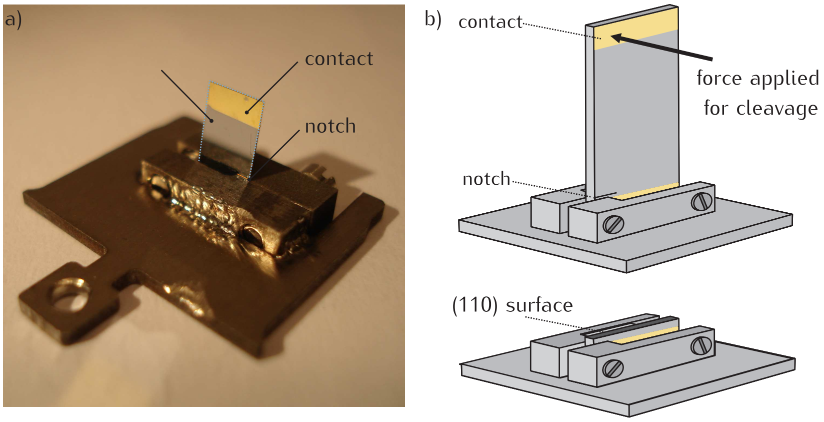

Figure 3.1: a) Picture of mounted sample. The notch is located just above the clamping bars. b) Schematics of a mounted sample before and after cleavage..

unit. The LT-STM additionally has a high temperature heater (T≈ 2500 K), a glowing stage, a field-emission setup and transition metal (Fe, Cr) evaporators.

3.2 Surface preparation

Small rectangular pieces (4x10 mm2) are cleaved from the semiconductor wafer containing the structure of interest. For STM measurement, it is essential to have good electric contact to the sample. As a simple contact between the semiconducting sample and the metallic holder may not be sufficient, contacts are deposited on top of the sample above the epilayers. This is done by thermal evaporation. The samples are placed on a holder and a mask is protects the position of the cleavage. Depending on the sample doping, different type of metallic contacts are deposited: for an n-type contact Ni(5nm)/Ge(15nm)/Au(150nm) layers and for grown p-type Zn(10nm)/Ni(10nm)/Au(150nm) layers. The Ohmic contact is created by a short annealing step at 300°C. The wafers are usually about 350-600 nm thick. To readily achieve an atomically flat surface by cleavage, the thickness is reduced to 375-575 nm. This is done by mechanically polishing the substrate with an aluminum oxide/silicon carbide powder. After grinding the sample is carefully cleaned with isopropanol and a scratch is made at the preferred cleavage position. The scratch is 1 mm long and creates a V-notch at the edge of the sample providing a starting point for the propagation of the cleavage plane. Finally the sample is mounted in a holder as shown in Fig. 3.1a. The sample edge is clamped between two metallic bars. The load on the sample is made even by adding indium in between the sample and the clamping bars. The indium is melted while the screws are carefully tightened.

The mounted sample is then loaded in the UHV system and heated at 150°C for 20 min in the preparation chamber, to remove water and other organic compounds. On the day of the experiment, the sample is cleaved in the STM chamber by pushing the top part of the sample with the wobble-stick (see Fig. 3.1b). The quality of the cleavage depends not only on the accuracy of the preparation but also on the strain present in the epilayers and the semiconductors materials. The yield close to 90% on III-V semiconductors drops to 5-10% on II-VI semiconductors

3.3 Tip preparation

The reproducible elaboration of sharp and stable metallic tips is an essential part of STM technique. In this thesis only W tips have been used. Alternatives are Pt/Ir or Au tips. A well-established electrochemical method is employed to fabricate sharp W tips[60]. The 0.25 mm thick pure poly-crystalline W wires are electrochemically etched in a 2.0 molar KOH solution. This process is schematically represented in Fig. 3.2a. First the W wire is fixed/welded on the commercial Omicron holders. Then ≈ 8 mm out the 10 mm of the W wire is dipped vertically in the KOH solution. A positive voltage (6 volts) is applied between the W wire (anode] and the Pt/Ir cathode. In these conditions, the following reaction takes place:

$$W(s) + 2OH^{-}(aq) + 2H_2O(l) \rightarrow WO_4^{2-}(aq) + 3H_2(g), \qquad (3.1)$$

A glass plate between anode and cathode prevent the bubbles of H_2 created at the cathode gas to interfere with the dissolution of the W wire. The product of the reaction WO_4^{2-} sinks down along the wire. Consequently the W wire is partially shielded of the W wire and the highest etching rate is found at the meniscus. The reaction can either be followed by monitoring the decrease in current or by eye as the refractive index of the solution changes upon etching. A neck appears at the position of the meniscus which breaks abruptly under the weight of the lower part leaving a very sharp tip as shown in the Scanning Electron Microscope (SEM) image in Fig. 3.2b and c. The radius of the tip apex is typically around 50 nm. At drop-off, the current drops and triggers a very fast switch off the applied voltage to prevent further etching of the sharp tip apex.

The tip is then loaded in the UHV system and heated at 200°C for 20 min in the preparation chamber to remove water and other organic compounds. The oxide layer formed on the tip during etching is removed by Ar ions sputtering with an ion energy of about 1 keV for 20 min. This step additionally stabilizes the tip apex. An optional step is to bring the tip to glowing by driving a high current through it. At a temperature above 1000 K, the oxide is layer removed thoroughly. The quality of the tip preparation can be checked by field emission of the tip against a spherical electrode. The radius of the apex scales with the onset voltage of the field emission current. Reproducible I(V) characteristics of the emission indicate a high stability of the tip apex. The yield on the tip preparation is close to 90%.

3.4 Experimental conditions

The experimental conditions are slightly different from one setup to the other.

At room temperature, the absence of cryogenics allows for faster operations. However, the stability of the tip during the measurements is reduced compared to low temperatures. For example, tunneling at positive bias voltages is more

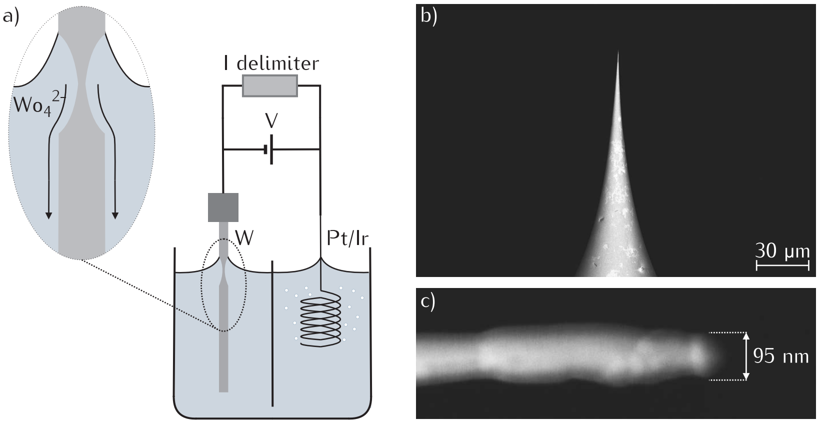

Figure 3.2: a) Schematics of the electrochemical etching of the W tips. The arrows in the inset indicate the flow of products sinking along the wire. b) SEM image of an etched W tip. The tapered shape is the result of the necking during etching. c) SEM image of the W tip apex. The radius of the tip apex is ≈ 50 nm.

cumbersome. Furthermore, thermal drift requires to reduce the scanning range or to manually compensate by adjusting the scanning area after each image. As a result, most of the images acquired are slightly distorted. Finally, the pressure of $p \approx 2 \times 10^{-11}$ mbar keeps the cleaved surface clean of adsorbates for 48 h only.

At low temperature, the samples are kept clean for weeks. Another advantage is the low amount of drift and the high stability of the tip apex. This allows to perform spatially resolved I-(V) spectroscopy. Those experiments typically last between 5 and 12 h and are performed overnight. Unfortunately, the LT setup suffers sometimes from noise of unknown origin. The choice of cryogenics, LN_2 or LHe, depends mainly on the physical phenomena investigated. Because of their differences, the two STM setups have different usage. The study of nanostructures is mainly done at room temperature while the study of single dopants is mainly done at low temperatures.

chapter 4

A comprehensive study of single Fe impurities in GaAs by X-STM

This chapter presents the X-STM and STS study of deep Fe acceptors in GaAs. A dilute distribution of the Fe dopants allowed for imaging and manipulating the core d-states of a single Fe. The crystal field split states of e and t_2 symmetry of the 3d states of a single Fe impurity in GaAs were imaged by means of STS. Additionally, evidence of internal transitions involving those core states is shown which are supported by theoretical predictions.

Control and measurement of the electronic, magnetic and optical properties of a single electronic state in a semiconductor have advanced rapidly over the past several years[61], and are approaching the point of significant technological importance[12,62–64]. Achievements include controlled positioning of small numbers of dopants within the semiconducting host[55,64–67] with quantitative theoretical descriptions of their wave functions[68,69], as well as local perturbations of their properties including optical orientation of their spin[70], electrical control of their charge state[17,50], and electrical probing of their spin excitations[71]. Since its invention, STM techniques have been probing the local density of states around dopants and defects in semiconductors[45]. STM measurements have been mostly carried out on single impurities on surfaces. STM in cross-sectional geometry is a less common approach allowing the investigation of impurities buried up to 10 monolayers below the surface of zinc-blende semiconductors. Such studies have been extensively performed and reported by several groups.[45–47]. Up to now however, these studies have been limited to shallow impurities. Shallow donors and acceptors represent the majority of dopants used for technological purposes, as they increase and modulate the conductivity in semiconductor crystals. Consequently, they draw large interest. Electronic manipulation of dopant charge states using STM has been predominately limited to ionization of these Coulombically-bound (shallow) donor and acceptor levels[50,72], although switching a Si dopant between a substitutional and interstitial position with an associated charge change has also been demonstrated recently[73]. From the years 2000, an interest arises for deeper dopants in semiconductor: transition metals atoms. The prospect of ferromagnetic semiconductors motivated the atomic scale study of transition metal impurities in semiconductors, in particular Mn atoms in GaAs. In these years, X-STM experiments allowed the determination of not only the spatially distribution of Mn atoms but also the spatial structure of the Mn acceptor wave function. The charge manipulation of Mn acceptor in GaAs, with a binding energy of 113 meV, was also reported[17]. Following which, the hole mediated interactions were visualized[55], as well as the effect of strain on the Mn acceptor wave function[74] and the crystal/vacuum interface on the Mn binding energy[75]. Despite a higher binding energy, it appears from the X-STM studies that the Mn acceptor state has a relatively strong host-like character. While a Mn impurity in GaAs can not be considered as shallow dopant, it gives rise to bound state which should be distinguished from an impurity-like state. Electronic manipulation of tightly bound states, especially the spin-polarized core *d* electrons of transition-metal dopants would permit a wider range of novel phenomena, including changing the core spin and magnetic interactions of a dopant. Such transitions have been measured optically for ensembles of transition-metal dopants in semiconductors[76], and there is evidence of multiple *d*-states associated with single transition-metal dopants embedded in the surface layer[77]. Direct electrical manipulation of the charging of these core states, however, has not been demonstrated, especially for a single dopant that is tetrahedrally bonded with the host, and hence has the symmetry of a bulk substitutional site. Fe impurities act as deep acceptors in GaAs with a binding energy of 510 meV and are found in different valence state. Studying Fe impurities in GaAs represents therefore an opportunity to explore the relation between a large binding energy and higher localization of the impurities states as well as the possibility an electronic or magnetic manipulation of these states. The study of Fe dopants in GaAs presented in the following sections is therefore the first study on deep sub-surface dopants.

4.1 Incorporation of Fe impurities in GaAs

4.1.1 Spatial distribution

Data presented in this chapter is the result of X-STM measurements performed on different GaAs:Fe samples grown by Molecular Beam Epitaxy (MBE) by Richard Campion at the University of Nottingham. Those samples, especially designed for X-STM experiments, were grown on a Si-doped GaAs substrate with $Al_{0.3}Ga_{0.7}As$ markers indicating the regions of interest. Each sample contains a 100 nm Fe-doped GaAs layer (nominal concentration: 2×10^{18} cm^{-3}) and a single Fe monolayer (ML) incorporated in GaAs. The nominal layer structure is GaAs substrate/100nm Fe:GaAs/200nm GaAs spacer /1 Fe ML/≈400nm GaAs. The growth temperature was 580°C during the entire growth procedure of the first sample. For the second and third sample, the growth temperature was lowered to 480°C to favor the incorporation of Fe. Additionally, the third sample includes carbon co-doping of the Fe-doped regions in order to locally improve the conductivity. Each growth was monitored *in-situ* by Reflection High Energy Electron

Diffraction (RHEED). The growth at 580°C showed the streaky RHEED pattern of the 2D growth of GaAs through the whole structure. The growth at 480°C showed the streaky RHEED pattern before the incorporation of Fe. The Fe doping (2×10^{18} cm^{-3}) resulted in a spotty RHEED pattern pointing towards a rough growth front. Subsequently, the 200 nm spacer layer allowed, to a certain extent, for the smoothing of the growth front before the deposition of the single Fe monolayer. At 480°C, the growth of the single Fe monolayer led to a complete and fast transformation of the RHEED pattern into rings characteristic of polycrystalline surfaces. Transition metal dopants are know to have a low solubility in III-V semiconductors. Furthermore, their incorporation at high temperatures leads to strong segregation[78]. This issue is often circumvented by reducing the growth temperature as low as 200°C. At low temperature however, the GaAs host presents a large number of structural defects, like As anti-sites which can hinder the functionality of the layers.

The degree of incorporation of Fe impurities in those three samples was investigated by Secondary Ions Mass Spectrometry (SIMS). The concentration of Fe as a function of the sample depth is plotted in Fig. 4.1. The detection limit is around 5×10^{15} cm^{-3}. The nominal position of Fe is indicated by the arrows. The observations are as follows. First, the intended 2×10^{18} cm^{-3} Fe concentration in the doped layers is not reached. As expected, lowering the temperature allows for a higher incorporation of Fe. More unexpected, the simultaneous incorporation of C dopants results in a stronger solubility of Fe. The mechanism behind this fact remains unclear. Possibly, a different Fermi level at the growth front may favor the incorporation of multivalent impurities like Fe in GaAs. The limited solubility of Fe comes with a large scale segregation. At 480°C, a fraction of the Fe content is found in the spacer layer. Besides, in all samples, at the nominal position of the single Fe ML, an Fe concentration of 5×10^{17} cm^{-3} is found which seems to be the solubility limit for these growth conditions. From that position and towards the surface, the excess Fe segregates strongly over hundreds of nanometers. In the case of Mn δ-doped layers in GaAs a strong segregation occurs and SIMS[79] and X-STM investigations[78] have demonstrated segregation over distances of several tens of nanometers, which depends on the growth temperature and scales with the nominal Mn concentration. Here, the segregation length and intensity are thus larger than the one observed for Mn in GaAs. In all three samples, the Fe concentration is found to increase strongly in the 100 nm from the surface. Considering the great range of the segregation, it is reasonable to think that a large amount of Fe is indeed accumulated at the surface of the sample. However the tail observed is considered to be an artifact of the SIMS measurements. In these first 100 nm Fe atoms located in a larger surface area are detected.

The segregation profile was characterized at the atomic scale by X-STM. The detection limit is around 5×10^{16} cm^{-3}. In Fig. 4.2a two typical filled states images of the GaAs layer directly above the Fe monolayer are shown. Every single feature which is dark and anisotropic corresponds to a single Fe atom, as it will be explained in section 4 of this chapter. The nominal position of the Fe monolayer is indicated by the black dotted lines at the right edges. No Fe atoms are detected at this position; instead they have strongly segregated along the

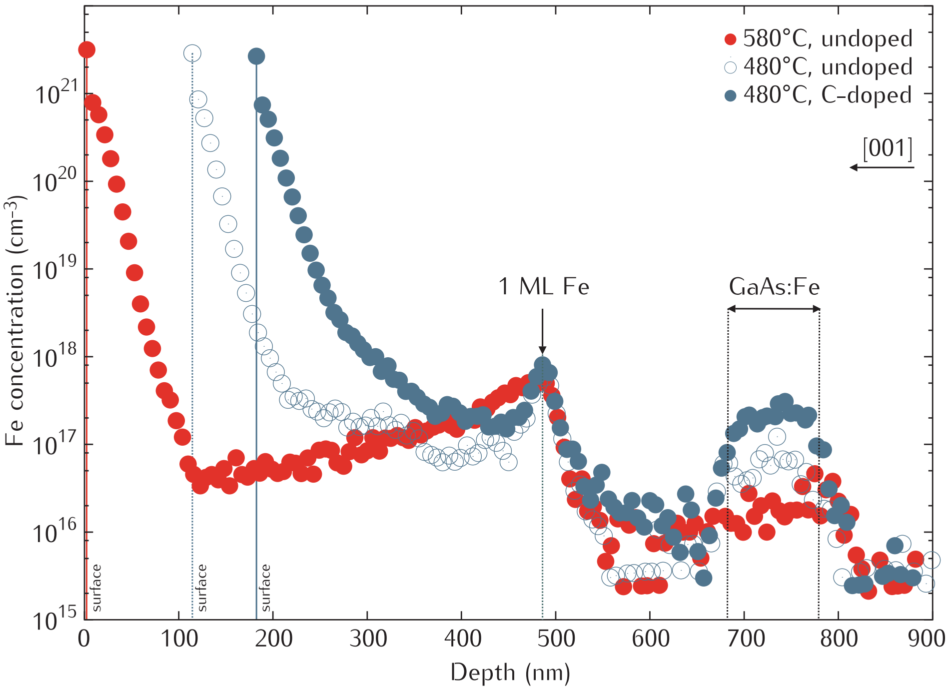

Figure 4.1: Fe concentration profile over the three GaAs:Fe samples obtained by SIMS. The intended position of the Fe doping is indicated by arrows and the sample surface by the dotted lines. The high concentration of Fe close to the surface is considered as an artifact of the SIMS measurement. Fe impurities are found to segregate over hundreds of nanometers. The incorporation of Fe is the most efficient at lower temperatures and upon C co-doping.

growth direction. Here Fe atoms are found as far as 150 nm from the intended position of the Fe monolayer. However, no clear Fe concentration gradient is observed and an accurate doping profile could not be determined due to poor statistics. This inhomogeneous incorporation of the Fe atoms suggests that Fe acts as a surfactant during the growth of the GaAs capping layer. Such behavior is consistent with the low solubility reported for Fe in GaAs. An alternative explanation could be the pinning of the Fermi-level of the growth surface. The presence of an electric field at the surface can lead to the redistribution of the impurities during growth[80].

More surprisingly, the segregated Fe atoms in the capping layer are not distributed randomly. In Fig. 4.2b, regions with high concentrations of Fe are visible. These Fe-rich regions consist of Fe atoms that group together during epitaxy. The change in RHEED patterns from 2D to 3D after the growth of the Fe monolayer agrees with this picture. No nano-precipitates or secondary crystallographic phases are detected. It is important to stress that the Fe atoms are not in nearest neighbor positions but form dilute Fe clusters which do not seem to influence the crystal structure of the semiconductor host. The tendency of

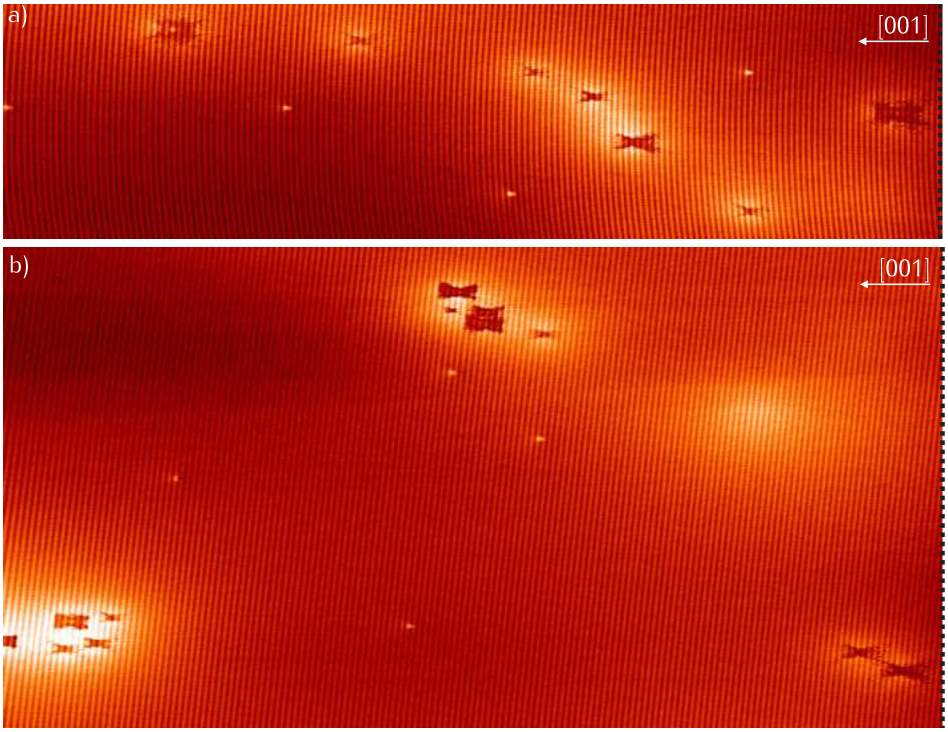

Figure 4.2: a) 90 nm×25 nm and b) 90 nm×50 nm filled states image of the region above the nominal position of the Fe ML, indicated by the black dotted lines. Dark and anistropic features indicate single Fe atoms. Fe atoms are found to segregate strongly and form dilute clusters.

transition metal atoms to aggregate during the epitaxial growth of III-V semiconductors has already been established[81]. The mechanisms behind this are long range attractive forces between magnetic atoms and defects, due to Coulombic interactions or strain field interactions combined with the low solubility of those atoms. The local density chemical fluctuations we observe falls into the definition of the so-called spinodal alloy decomposition observed in some dilute magnetic semiconductors[82,83]. Dietl et al. suggested that this phenomenon is a generic property of the number of diluted magnetic semiconductors[84]. Spinodal decomposition can take different forms and is generally difficult to detect experimentally if coherent nanocrystals are not formed, like in the present case of Fe in GaAs. Here, the nanoscale areas of high Fe concentration can be seen as isolated dilute clusters extending in three dimensions. It is interesting to note that these dilute clusters of Fe have been only observed in the sample without C co-doping. This is counter intuitive, since the incorporation of shallows acceptors should promote the aggregation of the magnetic ions by increasing the free carriers screening. This observation might indirectly indicate the unintentional creation of donors defects leading to self-compensation effects.

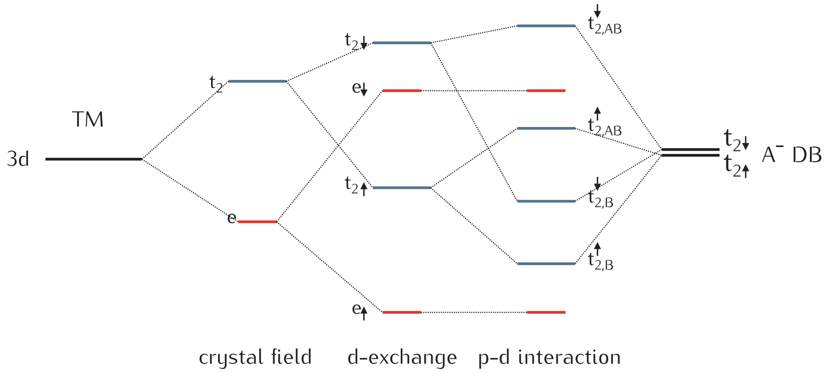

Figure 4.3: Splitting of the 3d energy levels of transitions metals by a tetrahedral crystal field, the exchange interaction and their hybridization with the neighboring anions A^-dangling bonds (DB). *e* levels, impurity-like t_2 and host-like t_2 are respectively indicated in red, blue and green.

The concentration of Fe closer to the sample surface was not imaged. These regions were not cleaved properly or exhibited poor conductivity. These experiences are consistent with the presence of structural defects and in agreement with the RHEED observations (ring patterns). The dilute distribution of Fe made allows for probing single Fe atoms, thereby determining the local electronic contrast induced by each impurity and exploring new phenomena presented in the following sections.

4.1.2 Electronic configuration

The most general picture of 3*d* transition metal atoms (TM) in III-V and II-VI semiconductors is that they largely substitute for cations in cubic crystals. Their electronic configuration as free atoms are [Ar] s^2d^n with n electrons in the d-shell. In order to replace cations with an s^2p^1 electronic configuration and act as isoelectronic impurities in the host crystal, TM atoms should release 3 electrons, two 4s electrons and one 3d electron. Their electronic configuration is then TM^{3+} (d^{n-1}) with $n-1$ electrons in their d-shell. The 3*d*-shell is partially filled and the 4*s* is the outermost shell. Deviations from this common rule are however observed. Some TM ions are in an energetically more favorable and stable configuration if they do not give away their d-electrons. This is in particular the case of Mn in small bandgap III-V semiconductors for example. In this case, Mn keeps its 5 electrons to keep a half-filled d-shell and become the Mn^{2+} acceptor.

At a substitutional position, a TM atom bonds to the four neighboring anions preserving the tetrahedral symmetry of the host crystal. Consequently, the atomic *d*-levels of TM ions in a cubic crystal field split into *e* and t_2 levels with different symmetries. *e* levels are double degenerated and t_2 levels are triple degenerated. Additionally, exchange interaction is taken into account which split the *e* and t_2 states by spin. The neighboring anions dangling bonds have s and p orbitals which form sp^3 hybridized orbitals with t_2 symmetry. As only orbitals

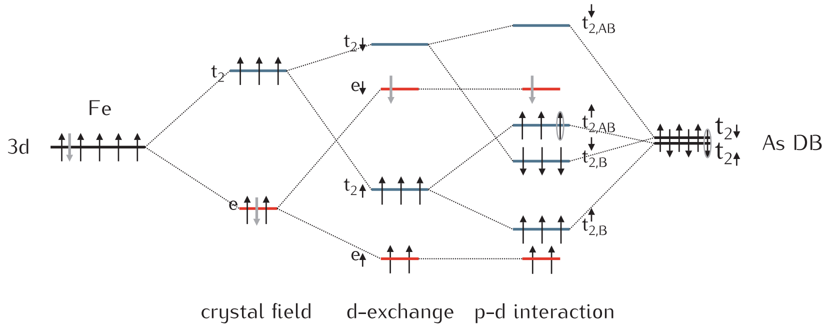

Figure 4.4: Splitting of the 3d energy levels of Fe by the tetrahedral crystal field of GaAs, the exchange interaction and their hybridization with the neighboring As dangling bonds. *e* levels, impurity-like t_2 and host-like t_2 are respectively indicated in red, blue and green. Black and gray symbols indicate respectively the occupation for Fe^{3+} (d^5) and Fe^{2+} (d^6) + h$^+$.

with similar symmetry interact efficiently, only the TM atom t_2 levels hybridize, producing bonding and antibonding orbitals. The *e* states remain mainly unperturbed. Although group theory plays a major role in determining the degeneracy and the symmetry of the impurity electronic levels in the crystalline field, it however does not provide any information about the position of the levels. In a tetrahedral environment, the *e* level is lower on energy than the t_2. The splitting of the 3*d* energy levels of transitions metals in the tetrahedral crystal field and their hybridization with the neighboring anions A$^-$dangling bonds (DB) is schematically represented in Fig. 4.3. Levels created upon hybridization have a different character. The t_2 bonding states can be described as transition-metal localized levels with impurity-like character, while the t_2 antibonding states can be seen as delocalized host-like states (in green in Fig. 4.3). The *e* states keep their impurity character. The occupation of the impurity-like states, *i.e.* *e* and bonding t_2 states, determines the core spin of the TM ion in the host crystal.

In the following paragraph, this model of the electronic structure of 3*d* impurities in small bandgap semiconductors is applied to the case of Fe in GaAs. The splitting of the 3d energy levels of Fe in the tetrahedral crystal field of GaAs and their hybridization with the neighboring As dangling bonds is represented schematically in Fig. 4.4. The free Fe ion has 6 electrons in its d-shell. When substituting for Ga in GaAs, it should release 3 electrons, two 4s electrons and one 3d electron to act as isoelectronic impurity. If it gives those 3 electrons to complete the As dangling bond, its electronic configuration is Fe^{3+} (d^5) with 5 electrons in its d-shell (half-filled). The occupation of the d-levels in this Fe^{3+} configuration is depicted by the black arrows in Fig. 4.4. Another configuration can arise if the Fe impurity does not give away 3d electrons to complete the As dangling bond. It becomes a neutral acceptor with the electronic configuration Fe^{2+} (d^6) with 6 electrons in its d-shell and a hole h$^+$ bound in the host-like t_2 antibonding state. The occupation of the d-levels in this Fe^{2+} configuration is illustrated using gray arrows for electrons and ellipses for holes in Fig. 4.4.

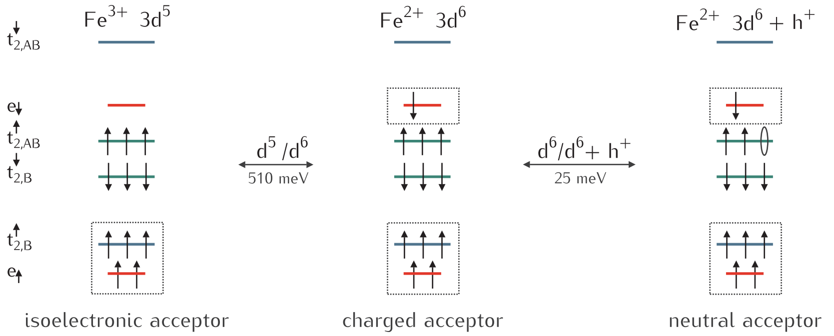

Figure 4.5: Known electronic configurations of an Fe atom in GaAs. *e* levels, impurity-like t_2 and host-like t_2 levels are respectively indicated in red, blue and green.

Depending on the electrostatic environment of the Fe^{2+} impurity, the hole state can be filled and the Fe^{2+} acceptor is ionized.

These are the three electronic configurations reported for an Fe atom in GaAs[85,86] and are summarized in Fig. 4.5. The core spin for each configuration is highlighted by the dotted boxes. Fe^{3+} (d^5) is the isoelectronic acceptor, Fe^{2+} (d^6) is the charged acceptor and the Fe^{2+} (d^6) + h^+ complex forms the neutral acceptor. The transition from Fe^{3+} to Fe^{2+} corresponds to a change in the population of the core states of Fe and of the core spin consequently. The energy required for this transition is 510 meV. The transition from Fe^{2+} to Fe^{2+} + h^+ corresponds to a change of the charge state (binding a hole) of the Fe acceptor and does not affect the core spin of the impurity. The energy required for this ionization is 25 meV.

The stable electronic configuration is determined by the position of the Fermi level in the semiconductor relative to the Fe electronic levels. The position of these levels in the GaAs band is presented in Fig. 4.6a. The position of the *e* impurity-like level in the bandgap is particularly important. Its occupation and thus its position relative to the Fermi level determines whether the Fe impurity is in its Fe^{3+} or Fe^{2+} core state. The level which indicates a change in core state is called charge transfer level (CTL). Here, if the Fermi level is found above the CTL found 510 meV above the GaAs valence band edge, Fe will be in its the Fe^{2+} state. If the Fermi level is found below this CTL, Fe will be in its Fe^{3+} state.

Moreover a charge transfer level located deep in the semiconductor bandgap acts as a charge trap and recombination center, pinning the Fermi level at this energy. Such deep acceptor states and CTL are common for TM ions in III-V semiconductors and explain the semi-insulating properties of most of the TM-doped III-V semiconductor, like GaAs:Cr or InP:Fe. A typical I(V) curve acquired at room temperature on the Fe-doped GaAs region (5×10^{17} cm^{-3} in this area) of the investigated samples is displayed in Fig. 4.6b. The Fermi level is found high in the GaAs bandgap, probably mid-gap. The larger apparent bandgap for GaAs is the result of TIBB (particularly strong in low-doped samples) and does not allow for a quantitative estimation of the Fermi level position.

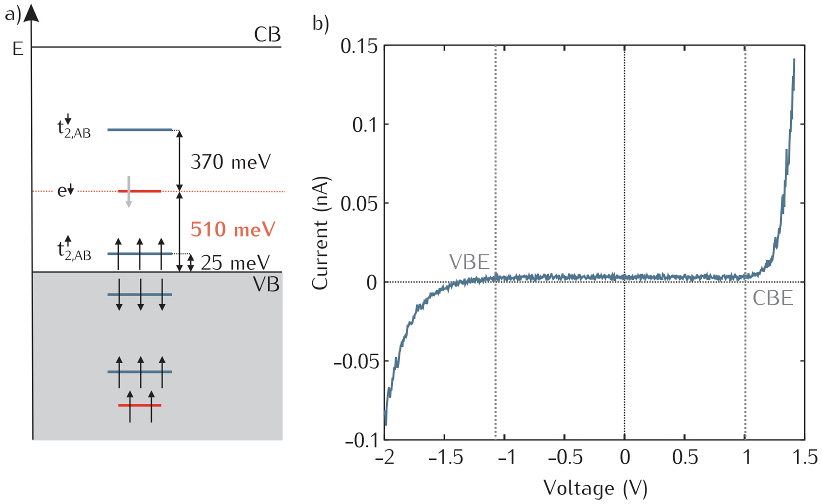

Figure 4.6: a) Energy levels related to Fe ions in GaAs relative to the GaAs semiconductor bands. The *e* impurity-like level can be seen as a charge transfer level (CTL). Its occupation and thus its position relative to the Fermi level determines whether the Fe impurity is in its Fe^{3+} or Fe^{2+} state. b) I(V) curve acquired at room temperature on the clean GaAs surface in the Fe-doped region. This plot is consistent with the Fe-doping (5×10^{17} cm^{-3} in this area) of the otherwise intrinsically doped GaAs: the sample Fermi level is found deep in the bandgap. The shift of the I(V) curve from 0 is a known effect of the I-V converter.

4.2 Core state manipulation of single Fe impurities in GaAs

4.2.1 Experimental observations and mechanism

As explained in chapter 2, changing the voltage in the STM experiments affects the TIBB which results in a change the electrostatic environment of the impurities. The electronic contrast appearing in the STM images can then be interpreted to determine the electronic configuration of the impurities. The first X-STM investigations on single Fe impurities in GaAs were performed at 77 K on the otherwise intrinsically doped GaAs epilayers, where the Fermi level is found close to midgap. A strong TIBB with a large spatial extent is expected due to the low doping level.

Figure 4.7 shows constant current empty and filled states topography images taken at different voltages at a position where three Fe atoms can be identified. The local electronic contrast induced by each Fe impurity is strongly dependent on the applied voltage. A clear identification of those Fe impurities is achieved at low negative voltages. This regime is presented in section 5 of this chapter. Here two regimes can be distinguished which give rise to very different electronic contrasts and shapes. In empty states images taken at positive voltages, as presented in Fig. 4.7a, Fe atoms appear as bright localized electronic features, while the majority is not visible. This electronic contrast is attributed to Fe dopants in their isoelectronic state. In their Fe^{3+} isoelectronic configuration, Fe

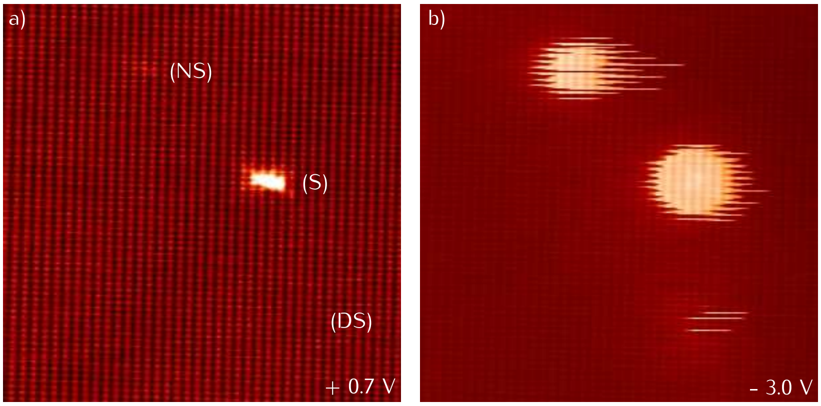

Figure 4.7: 23 nm×23 nm topography images of three single Fe impurities in GaAs taken at two different voltages. The Fe impurities are located at different depth below the surface labeled as (S) in the surface layer, (NS) near the surface and (DS) deep below the surface. At negative voltage (filled states imaging) the ionized Fe^{2+} impurities give rise to bright discs. At positive voltage (empty states imaging), the localized electronic contrast or its absence are attributed to isoelectronic Fe^{3+} impurities.

atoms should give rise to such a localized contrast that only impurities located in the surface layer (S) are expected to appear in the STM images. In this case the contrast originates from the difference in local density of states (LDOS) between the Fe atoms and the Ga atoms. The slightly delocalized features for Fe^{3+} atoms can be understood as the consequence of a slight hybridization of the Fe states with the neighboring As states. Consequently, if the Fe atom is at or very close to the surface, the LDOS difference is reflected on the tunneling current. If the Fe atoms located further below the surface, such small variation of LDOS does not affect significantly the tunneling current and should give a much weaker contrast or no contrast. The absence of electronic contrast for the large majority of the Fe impurities at positive applied voltage is better shown in Fig. 4.8. From these observations it can be concluded that at positive voltage Fe atoms are in their isoelectronic configuration Fe^{3+}.

In filled states images taken at negative voltages, as presented in Fig. 4.7b, a bright disc is visible around a number of Fe impurities. Such discs are generally associated to the ionization process of either donors[50] or acceptors[67]. In these studies, the onset of the disc indicates the spatial separation between the tip and the impurity resulting in a local TIBB sufficient to ionize the neutral impurity. The isotropic Coulomb field created by an ionized impurity induces a local enhancement of the states available for tunneling, and thus an increase in tunnel current. A brief summary of those studies is presented in section 3 of chapter 2. For similar reasons, the discs observed here for Fe impurities in GaAs are attributed to the presence of a Coulomb field. At negative voltages, an increase of the number of states corresponds to a Coulomb potential originating from a local negative charge. The $(Fe^{2+})^-$ charged acceptor state of Fe is therefore the only electronic configuration that can account for the presence of such discs.

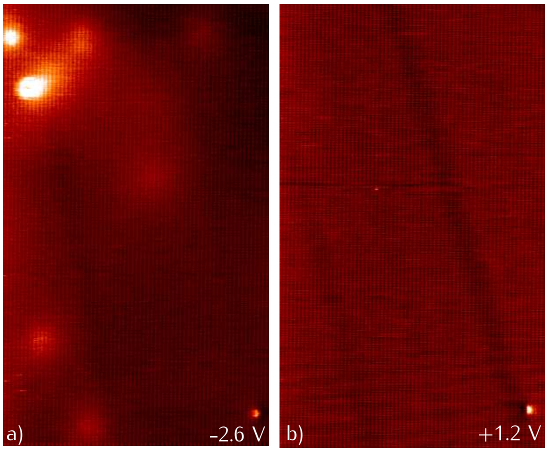

Figure 4.8: 30 nm×50 nm topography images of the same area at a) negative and b) positive voltage presenting a number of sub-surface Fe impurities. An isotropic Coulombic contrast is observed for each Fe impurity at negative voltage. The absence of electronic contrast arising from Fe impurities at positive voltage is attributed to their Fe^{3+} isoelectronic state. Only Fe atoms very close to the surface should be visible. They are absent here.

A mechanism is suggested which explains the change of the core electronic configuration of Fe atoms in GaAs when changing the voltage polarity and the presence of discs in topography images. This mechanism based on the tuning of the TIBB is illustrated in Fig. 4.9.

To begin with, two assumptions are made which will be discussed in the next section. First, the Fermi level on this Fe-doped GaAs sample is close to mid-gap. Consequently, in the bulk of the sample, the CTL is found below the Fermi level Second, close to the semiconductor surface, the bands are bent upwards. Hence the so-called flat band voltage V_{FB} is found at negative voltages. The origin of the latest assumption, which will be supported in the next section, is not clear. An initial upward bending of the semiconductor bands close to the surface is unusual. A possible cause would be the presence of defects at the surface which could pinned the Fermi level, but only a small concentration of defects was observed. Another explanation would be the presence of a 15 nm AlGaAs layer close to the Fe-doped region. Meant as a marker, this layer acts as a barrier and a space charge region might be created from the the GaAs/AlGaAs interface. Such region would be extended considering the low doping level of GaAs. According to these hypotheses, at positive voltages (not depicted here), the semiconductor bands are strongly bent upwards and close to the surface the Fe^{2+}/Fe^{3+} CTL is found above the Fermi level. Under this condition, the corresponding *e* level is not occupied and the Fe impurities in this area are stable in their isoelectronic configuration Fe^{3+}.

At low negative applied voltage, the semiconductor bands are also bent upwards and close to the surface the Fe^{2+}/Fe^{3+} CTL is found above the Fermi level. Consequently, when the tip is far from an Fe impurity, the *e* level of this Fe impurity is unoccupied and impurity is in its Fe^{3+} isoelectronic acceptor state. This situation is illustrated in Fig. 4.9a. As the tip is brought closer to the impurity, the electrostatic environment of the dopant changes under the effect of TIBB. At voltages higher than V_{FB}, the initial upwards band bending is reduced. At V_{FB}, the semiconductor bands are flat. At voltages lower than V_{FB}, the bands are bent downwards. In other words, at negative bias voltage, under the effect of TIBB, the semiconductor bands are effectively pulled towards lower energies. Consequently, from a specific distance, the TIBB becomes sufficient to bring the CTL level below the Fermi level. From this position the stable electronic configuration of Fe becomes Fe^{2+} with 6 electrons in the d-shell. This situation is illustrated in Fig. 4.9b. In the Fe^{2+} configuration, the As dangling bond is not complete and a hole should be weakly bound to the Fe center. However, the energy level associated with this hole is found very close to the valence band and well below the Fermi level. Therefore this host-like state is occupied and Fe^{2+} carries a localized negative charge. The presence of this negative charge induces an isotropic Coulomb field around the Fe impurity which interacts with GaAs states. The semiconductor bands are locally pulled upwards and the number of states available for tunneling, *i.e.* the tunnel current, is enhanced. This causes the tip to retract abruptly to keep the tunneling current constant. Once the tip is away from the Fe center, this sequence of events is reversed. Hence, the disc represent the region where the TIBB is sufficient to bring Fe from its Fe^{3+} isoelectronic acceptor state to its charged acceptor state $(Fe^{2+})^-$.

Charge manipulation of an impurity by means of an STM tip or a nearby charged defect has already been demonstrated for various impurities in III-V semiconductors[50,67,72]. But this manipulation shown here differs from shallow-state ionization of dopants. The novelty in this system is that the Fe impurities release a core *d*-state hole, whereas former studies on Mn acceptors and Si donors report respectively on the loss of a bound valence hole or a bound conduction electron. Here the neutral state is Fe^{3+}, and not the effective-mass-like complex Fe^{2+}, h^+. The filling of the 3*d*-shell changes from five to six electrons, and the core spin state changes from $S = 5/2$ to $S = 2$. Such change of the *d*-state core occupation has not been observed before. The $(Fe^{2+})^-$ acceptor state of an Fe atom in the top layer of a *p*-type GaAs surface has been previously reported, but the charge state was not demonstrated to be manipulated[77].

The discs around the Fe ions were only observed at in the X-STM experiments performed on the otherwise undoped sample with a sharp tip, at low temperature. A sharp tip apex is crucial. The spatial extent of the electric field from a blunt tip is much larger and the change in core states of an Fe impurity occurs therefore at a larger distance from the impurity. Consequently, the Fe atoms are negatively charged but the disc corresponding to the transition does not appear in the STM images. The absence of discs in the sample with C co-doping is explained by the different initial band bending and TIBB due to the higher density of charge carriers.

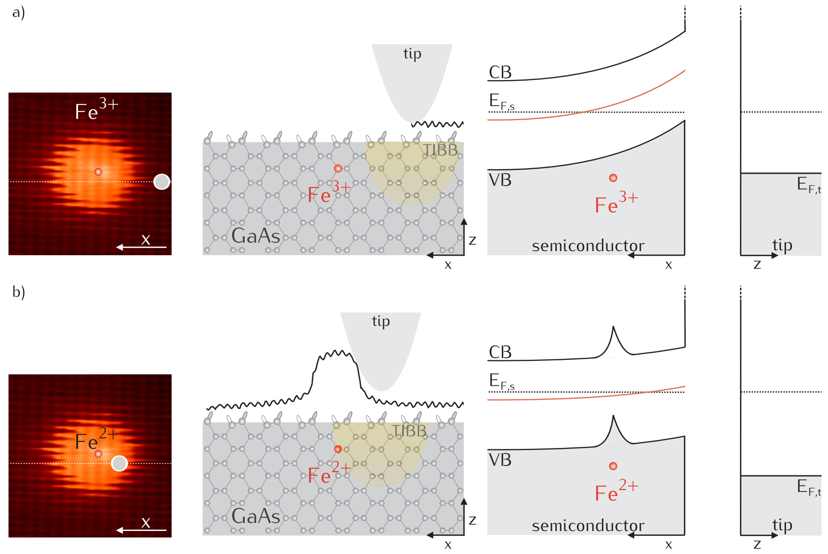

Figure 4.9: Illustration of the core state manipulation mechanism, displaying the STM height profile across the disc. Insets: 10 nm×10 nm filled states topography image of a single Fe impurity in GaAs taken at -3.0 V. a) The tip is far from the Fe impurity. The CTL is found above the Fermi level and the Fe atom is in its Fe^{3+} isoelectronic state. b) The tip is close enough to the Fe impurity. Locally, at the position of the dopant, the CTL is found below the Fermi level and the stable configuration for Fe is the charged acceptor state (Fe^{2+})$^{-}$ The presence of an isotropic Coulomb field around the charged impurity creates locally additional states. As a result, the tip is retracted to keep the tunnel current constant.

4.2.2 Dependence on tunneling parameters

To check the grounds of the mechanism suggested in the previous section, the dependence of the disc diameter on the tunneling parameters was investigated. From these observations, the relative position of the different levels in the bandgap and the initial band bending were determined resulting in the two earlier assumptions.

As reported for Mn acceptors and Si donors, the diameter of the discs is expected to change with the applied voltage and tip-sample distance, *i.e.* the current setpoint. Figure 4.10 shows constant current filled states topography images taken at different voltages and current setpoint but at the same position, where six Fe atoms can be identified, four of which very clearly.

The diameter of the discs is found to increase with higher negative voltages and lower current setpoints. The diameter dependence on the voltage is understood in terms of TIBB. The spatial extent of TIBB increases with applied voltage and the core state modification of an Fe center happens at a larger impurity-tip distance. In Fig. 4.11c, the evolution of the disc diameter as a function of the bias voltage is plotted, showing clearly the increase in diameter with higher negative voltage.

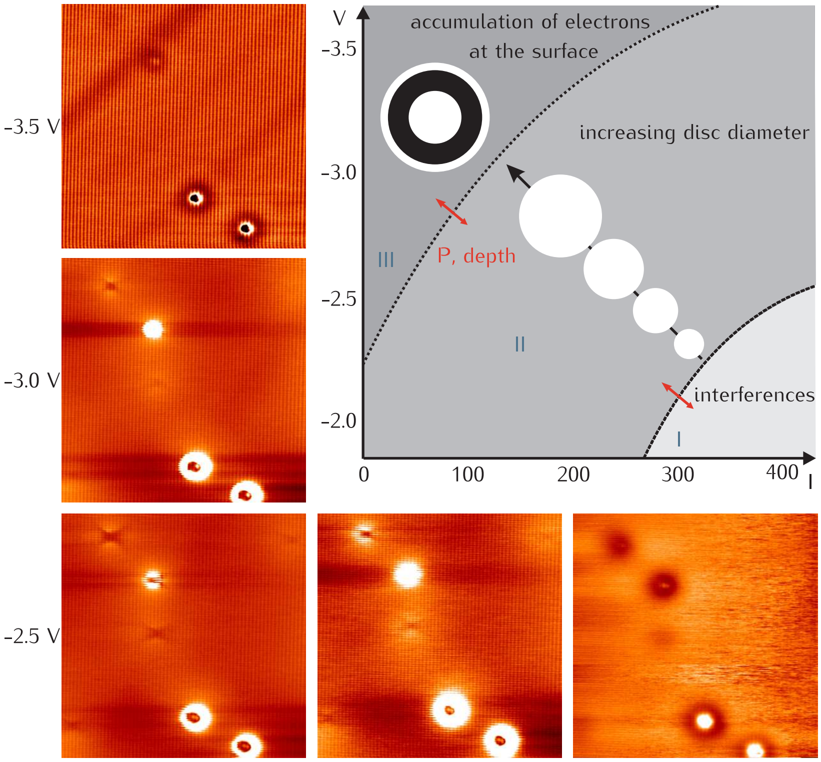

200 pA 140 pA 20 pA

Figure 4.10: 30 nm×30 nm filled states images taken at the same position for different voltages and current setpoints. Six Fe atoms can be identified, four of which more clearly. Diagram: summary of different imaging regimes and the associated electronic contrasts.

Associating the diameter dependence on the current to a change in TIBB requires making the assumption that the semiconductors bands are bent upwards at low negative voltage. Under this consideration, decreasing the current setpoint, which corresponds to increasing the tip-sample distance, results in a flattening of the semiconductor bands. The bands are pulled lower and the core state manipulation occurs at a greater distance from the impurity. In Fig. 4.11d, the evolution of the disc diameter as a function of the current setpoint is plotted, showing clearly a decrease in diameter with decreasing current setpoint. The evolution of the diameter on a function of the tip sample distance shows a more complex behavior. Two regimes can be distinguished. For current setpoints above 100 pA, the disc diameter varies very slowly. Such observation is consistent with the small TIBB variation expected when changing the current. For current setpoints below 100 pA, *i.e.* when the tip-sample distance is large, the disc diameter varies strongly. This strong dependence has supposedly a different origin. Because the measurements were performed under illumination with a red laser, it is suggested that a photo-current is created which contributes to the tunneling current. In the case of a low current setpoint, the contribution of this photo-current would dominate.

For very high negative voltages and/or very low currents, another type of electronic contrast is visible instead of a large disc. This feature corresponds to charge density oscillations around the negatively charged Fe center. The presence of such Friedel-like oscillations has already been reported for ionized dopants, such as Si[87] and Mn[88] in GaAs, in n-type semiconductors. Those oscillations originate from the accumulation of electrons at surface created locally under the tip when the conduction band edge is pulled below the Fermi level. These electrons screen charged defects and lead here to charge density oscillations around each negatively charged $(\mathrm{Fe}^{2+})^{-}$ ion. This observation is made when the applied voltage is higher than the difference between the tip work function and the electron affinity in the semiconductor. This condition is usually met in semiconductors with a Fermi level relatively high in the bandgap. The different regimes and the associated electronic contrasts are schematically summarized in Figure 4.10. The diagram consists in three distinct regions. The nature and the origin of region I is investigated in details in section 4 of this chapter. In region II, discs are visible and their diameter depend on applied voltage and current setpoint as shown in Figure 4.11c and d. The semiconductor bands are bent upwards. In region III, the charged $(\mathrm{Fe}^{2+})^{-}$ ions are screened by electrons present at the surface. The bands are bent downwards. The flat band voltage, which depends on the tip-sample distance, is found in between region II and region III.

To further check the basis of the core state manipulation mechanism, the diameter dependence on the sample illumination was investigated. Originally, the illumination of the sample at low temperatures was required to improve the conductivity. A controlled illumination was achieved by using a red laser and tuning its intensity. The variation in diameter as a function of the laser power is reported in Figure 4.11b. The diameter of the disc increases with increasing laser power. This is consistently explained by the creation of a photo-voltage at the surface of the semiconductor. The presence of additional charge carriers results in an effective flattening of the semiconductor bands. At fixed voltage and current, changing the illumination condition leads to a shift of the regions defined in Figure 4.10 as indicated by the red double arrows. The dependence of the discs diameters on the tunneling conditions are in agreement with the mechanism suggested as responsible for the reversible $\mathrm{Fe}^{3+}/\mathrm{Fe}^{2+}$ manipulation.

Fe impurities located deep in the bulk (>5ML) show bright isotropic Coulomb electronic contrasts. These Fe impurities are therefore in their $(\mathrm{Fe}^{2+})^{-}$ charged state. This is the most stable electronic configuration since the CTL is located below the Fermi level in the bulk. However, sharp disc edges are not visible. It means that, at negative voltages, these impurities are always charged regardless from the position of the tip and the magnitude the TIBB. The manipulation of the core state from $(\mathrm{Fe}^{2+})^{-}$ to Fe^{3+} requires to bring the CTL above the Fermi level. This is then only achieved by applying a positive bias voltage. The disc signature of the core state manipulation is only visible for Fe impurities close to the surface (<5ML). At a given voltage, the Fe atoms the closest to the surface show discs with the largest diameters. This means that these impurities are the first to be manipulated. Unfortunately, there is no absolute way to determine the depth of each Fe impurity. According to the proposed mechanism and the initial bending

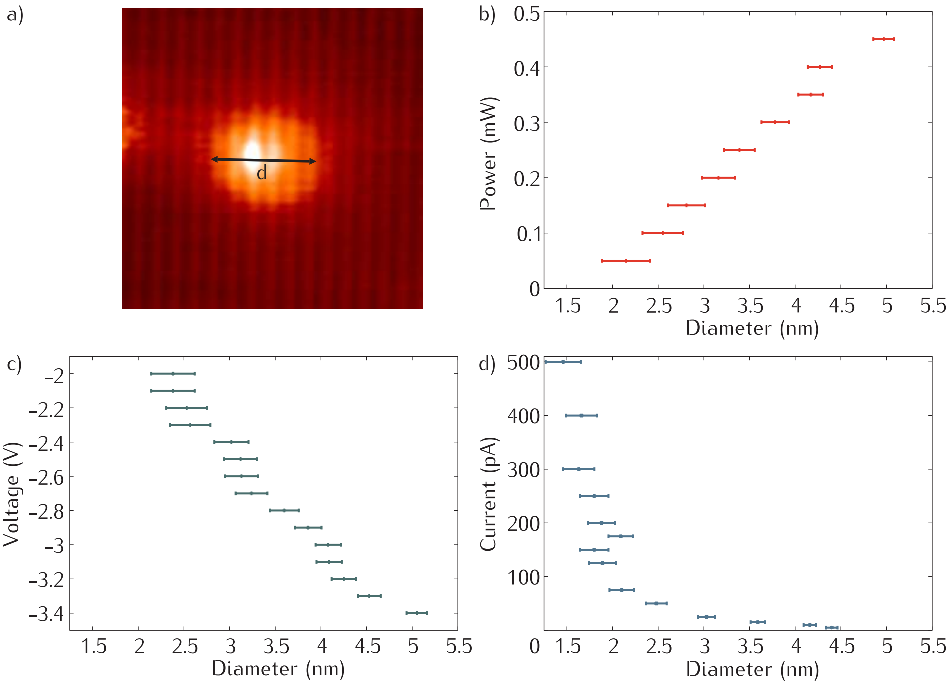

Figure 4.11: a) 8.5 nm×8.5 nm filled states image of an Fe^{3+}/Fe^{2+} disc. Evolution of the disc diameter as a function of b) laser power c) applied voltage and d) current setpoint *i.e.* tip sample distance. The initial tunneling conditions are V=-2.5 V, i=100 pA and P=0.1 mW)

of the semiconductor bands, this is supposedly a demonstration of the decreased binding energy of the Fe acceptor close to the semiconductor/vacuum interface. Enhancement of the binding energies of Si donors[51] and Mn acceptors[75] close to the semiconductor/vacuum interface have been reported.

A peculiar feature of the discs was observed which was never reported for ionization of shallow dopants. As presented in Fig. 4.7, the position of the disc edge can depend on the nature of the atoms under the tip. The impurity-tip distance necessary to affect the core states of Fe is larger when the tip is located above the As sub-lattice. This could originate from stronger hybridization between the *d*-states of Fe and the host valence band states. Furthermore, an instability is observed for some Fe impurities when the Fermi level is locally very close to the CTL and might be due to spontaneous relaxation from $(Fe^{2+})^-$ to Fe^{3+} state. Considering this observation as a specificity of a change in *d*-shell occupancy is however not possible. Analogous behavior was recently described for Si atoms at the (110) surface of GaAs[73].

4.3 Imaging the core states of single Fe impurities in GaAs

4.3.1 Experimental observations of the core states of Fe in GaAs

As presented in chapter 2, the wave function mapping of donors and acceptors can be realized by STM and STS. Visualizing the wave function shape and spatial extent of a dopant provides information about the nature of its neutral state and its binding energy. Such STM and STS experiments have been carried out for several transition metal atoms, like Mn, Fe or Co, in the surface layer of GaAs[77]. Among sub-surface atoms, the only transition metal which has been characterized with these methods is Mn in GaAs. In this section, the STM and STS analysis of sub-surface Fe impurities in GaAs is presented.

4.3.1.1 Topography

The manipulation of the core states of single Fe impurities in GaAs demonstrated in the previous section indicates that the neutral state of the Fe acceptor in GaAs is the isoelectronic Fe^{3+} state. In the empty states topography images, the electronic contrast created by subsurface Fe impurities appeared to be very localized and restricted to Fe atoms very close to the surface. The small number of empty states images acquired, due to the poor conductivity at positive bias voltage, did not allow to assign a particular shape to this electronic contrast. This problem was solved by co-doping the Fe-doped regions with C atoms. These shallows acceptors increased greatly the conductivity while having little influence on the position of the sample Fermi level.

Fig. 4.12 presents empty-states images taken on a single Fe impurity at different voltages. At first sight, it shows a strong similarity with the contrast reported for the sub-surface $[Mn^{2+}+h^{+}]$ neutral acceptor state[17]. Both contrasts share common features like their brightness and their anisotropic shape. It is here suggested that both anisotropic shape of the Fe acceptor and Mn acceptor wave functions originates from the cubic symmetry of the GaAs crystal[68]. This implies the presence of an Fe acceptor level with t_2 symmetry within the GaAs bandgap. As presented in first section of this chapter, the hybridization of the Fe d levels of t_2 symmetry, with the As sp^3 dangling bonds of same symmetry results in antibonding t_2 states in the bandgap of GaAs. According to this description, three levels related to Fe, are found in the bandgap of GaAs (see Fig. 4.6), of which, two with t_2 symmetry. At positive bias voltages, electrons are injected in the empty states of the semiconductor sample, that is in the conduction band and the empty energy levels associated to Fe impurities. At positive bias voltages, the semiconductors bands are bend upwards by TIBB. Consequently, the deep e and t_2 levels respectively located 510 meV and 880 meV above the valence band edge are empty. The shallow t_2 level located 25 meV above the valence band edge is assumed to be occupied.. A stronger positive voltage is necessary to bring this level above the Fermi level located deep in the bandgap. This condition is not met here. Instead, the level occupation described here corresponds to the electronic configuration of the Fe^{3+} isoelectronic acceptor state. This also means that electrons tunneling through the deep e and t_2 levels are responsible for the bright

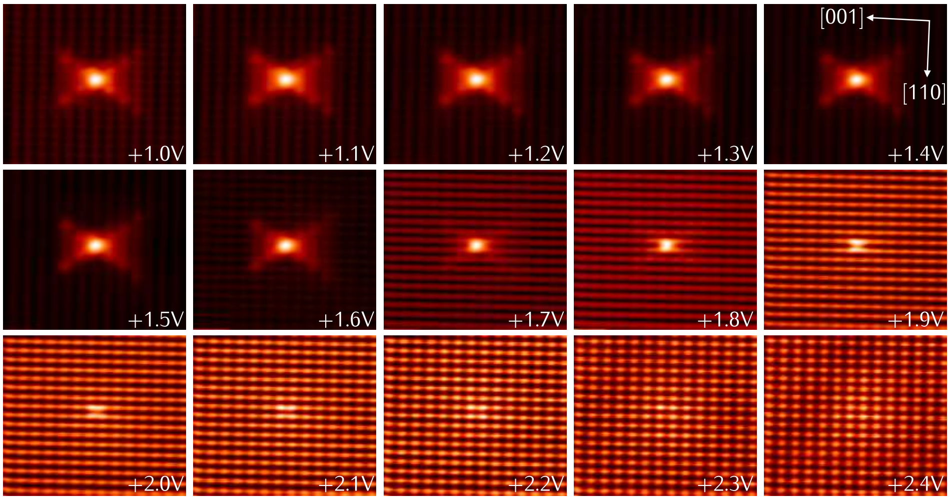

Figure 4.12: 7.5 nm×7 nm empty states images of a single Fe impurity taken at different voltages.

electronic contrast observed in the empty states images. The anisotropic shape is solely attributed to the t_2 core level wave function, as the e level is expected to have a much more localized contrast. This higher localization is explained by the weak hybridization of the e states with states the host crystal, due to a different symmetry of the corresponding d-orbitals. Fig. 4.13 presents the d-orbitals associated with the e and t_2 states. Simple geometrical considerations show that the double degenerated e states cannot efficiently couple to the sp^3 dangling bonds of the As neighbors organized following a tetrahedron. Comparing STM height profiles taken across the neutral Mn and Fe impurities shows that, in the case of Fe, the enhancement of the LDOS is more localized on the impurity itself. This can be explained by the deep nature of the Fe acceptors levels as well as the additional and localized tunneling channel due to the presence of an e state in the bandgap for Fe.

The voltage dependence shown in Fig. 4.12 is analogous to the one reported for other acceptors. The anisotropic shape, clearly visible a low voltages, fades away at higher voltages. It is interesting to note that this evolution is not completely gradual. Around V=+1.7 V, the anisotropic shape disappears for the most part, leaving only a bright localized contrast. This specific voltage also corresponds to a change in corrugation of the GaAs surface. Below that voltage threshold, the atomic rows are clearly defined along the [110] direction, whereas above this voltage, the atomic rows are well-defined along the [001] direction. This change in corrugation is explained by the position in energy of the different surface states involved in the tunneling process. At low voltages, electrons tunnel through the Fe state and the C_3 surfaces states. At high voltages, an additional tunneling channel appears involving the C_4 surfaces states. For this reason, as the voltage is increased, the contribution of the electrons tunneling through the Fe acceptor states to the total tunneling current becomes minimal. This effect

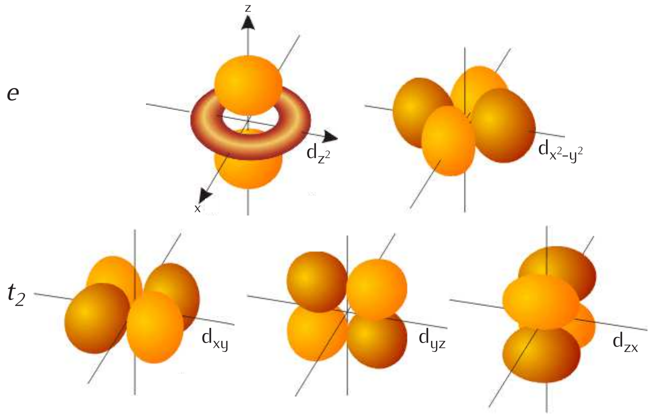

Figure 4.13: Schematic representation of the five-fold 3*d*-orbitals split under the cubic crystal field. The transition metal atom is located at the center.

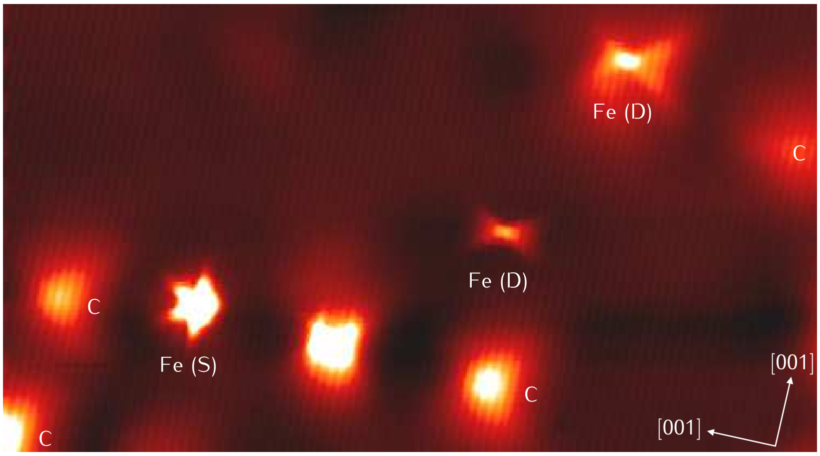

Figure 4.14: 27 nm×50 nm empty states image of a Fe and C-doped GaAs sample. C and Fe atoms are labeled. (S) surface dopant and (D) bulk dopant.

is further enhanced by the exponential decrease of the tunneling probability for states with lower energies.

A closer look at this bright electronic contrast shows that the shape is perfectly symmetric with respect to the [001] axis and highly symmetric with respect to the [110] axis. In the case of Mn atoms in GaAs, the degree of asymmetry with respect to the [110] axis is related to the interaction between the Mn state and the asymmetric buckled surface. Consequently, the symmetry is strongly dependent on the depth of the impurity relative to the surface. The symmetry decreases as the impurities is found closer to the surface, *i.e.* Mn atoms located 5 to 10 ML below the surface show the highest symmetry. This depth dependence is also observed for Fe impurities. In Fig. 4.14, three Fe atoms are visible which are located at different depth. The Fe atom labeled (S) is located in the surface layer. Its shape is similar to the one reported for an Fe atom substituted in the surface layer by Richardella et al.[77]. The low Fe concentration achieved in each sample did not allow for a systematic study of the shapes nor their attribution to a specific depth based on symmetry arguments. Nonetheless, Fe atoms in the first monolayers exhibit a higher degree of symmetry than Mn atoms with respect to the [110] direction. The suggested origin for this higher symmetry is the higher binding energy and weaker hybridization of the Fe states with the host crystal. Additionally, the surface does not affect as strongly the wave functions of the Fe states since they are more localized. The deep acceptors states of Fe have a stronger impurity character while the Mn acceptor state has a stronger host-like character. The electronic configuration of the neutral state of an Fe acceptor in GaAs deduced from the analysis of the constant current topography images is in good agreement with the energy diagram based on the existent literature and shown in Fig. 4.6.

4.3.2 A tight binding approach to the core states of Fe in GaAs.

The validity of the STM analysis described in the previous section requires additional investigations. Identifying the energy states of Fe atoms in GaAs implies prerequisite knowledge about the system, mainly provided here by the review of Malguth et al.,[85]. The interaction between the Fe ion and the host crystal can be treated in perturbation theory because the interaction of the Fe center with the host crystal is small enough so that the electrons are localized and identified in a tight binding sense as from the Fe center itself. A theoretical approach was used based on tight binding calculations in order to explore the spatial extent of the deep Fe acceptors states. This work was motivated by the surprisingly large experimental spatial extent of the Fe wave function considering the strong impurity-like character of those states.

The wave functions of the d states of e and t_2 symmetry have been calculated by Victoria Kortan at the University of Iowa, using the formalism by Tang et al.,[68]. This approach previously reproduced successfully the wave function of Mn acceptors[17], and is perfectly adapted to the case of Fe as more localized wave functions are expected. The GaAs valence-band structure is described using an $spds^*$ tight-binding model including spin-orbit interactions[89]. The homogenous Green's functions are calculated from the eigen vectors and values of the corresponding Hamiltonian. The Fe impurity is described using a tight-binding $spdds^*$ model. The 3d-orbitals and 4d-orbitalsof Fe as well as the 4d-states of GaAs are taken into account in this model. The 4d-orbitals of Fe are however considered as being far outside the energy range of interest, *i.e.* the bandgap of GaAs. Including the d-orbitals of Fe in the tight-binding model allows to use an on-site local impurity potential. Previously, the potential was added to the four nearest neighbors of the impurity. The on-site potential for the d orbitals has a non-magnetic[90], a magnetic[91] and a spin-orbit part. Spin-up and spin-down level in the band gap are introduced by the non-magnetic part, which are subsequently split by the magnetic part. The angular momentum states are resolved by the spin-orbit part. The values of the nonmagnetic and magnetic potential are

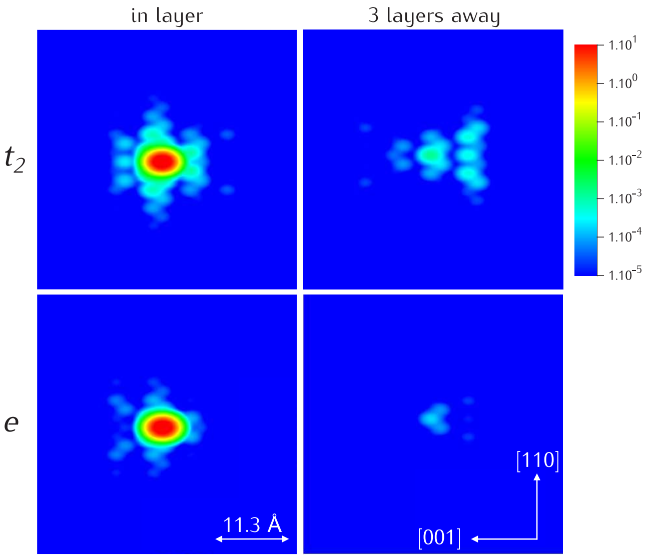

Figure 4.15: Calculated real space probability density of the d states of t_2 (top) and e (bottom) symmetry. On the left, the LDOS in the plane including the Fe impurity. On the right, the LDOS, three atomic planes away from the Fe impurity. As expected from the group theory, the e state gives rise to a highly localized wave function, while the t_2 state gives rise to a more delocalized wave function.

chosen to produce mid-gap states with energies corresponding to those found experimentally and reviewed by Malguth et al.[85]. The local density of states for the GaAs and Fe system is given by the imaginary part of the Green's function[68] calculated using the Koster Slater technique[92]. Previously for Mn, the chemical trend of impurity levels in semiconductors has been correctly predicted by this method[90].

Figure 4.15 presents the calculated real space probability density of the d states of t_2 (top) and e (bottom) symmetry. The calculations are performed for an Fe impurity located in the bulk of the host crystal. The plots shown here are 2D cuts through the bulk GaAs crystal. Consequently, the effect of the surface is not taken into account. On the left, the LDOS in the plane including the Fe impurity is plotted. On the right, the LDOS three atomic planes away from the Fe impurity is plotted. The LDOS associated to both the e and t_2 states are anisotropic. The LDOS of the t_2 level in the plane of the impurity shares common features with the shape for the Fe impurity in the surface (S) shown in Fig. 4.14, like the extensions the [110] direction. It is also perfectly symmetric with respect to the [001] direction. But the LDOS shape is not symmetric with respect to the [110] direction. The cross-like shape of the LDOS three planes away from the impurity is in agreement with the shapes observed for sub-surface Fe impurities (D) in the STM empty states image in Fig. 4.14. The contrast is spread over $\approx 2\,\text{nm}$. Moreover the LDOS is mostly localized on the impurity itself. This result is consistent with the experimental STM height profile taken above single

Fe impurities. Compared to the t_2 state, the e state gives rise to a much more localized wave function. The probability density is, also centered on the impurity, is not isotropic. Three atomic planes away from the Fe center, the LDOS becomes very localized within 1 nm. These results reflect well the prediction given by the group theory applied to the d-states of Fe in the tetrahedral environment in the cubic GaAs crystal as well as the STM experiments reported in the previous section.

4.3.3 Spectroscopic signature of the core states of Fe in GaAs

After a preliminary investigation of the nature of the acceptor states of Fe in GaAs by STM and tight-binding calculations, a second experimental study was carried on by means of I-V spectroscopy. The advantages of this technique have been introduced in chapter 2.

The $\log(dI/dV)$ curves presented in Fig. 4.16 were taken on GaAs about 5 nm away from an Fe impurity (in blue) and exactly above a sub-surface Fe impurity (in red) for voltages between 0 V and 1.6 V. The data acquisition was set such that the tip-sample distance was the same for every point. This is achieved by moving the tip with the feedback loop on at voltage, where the topography is uniform across the whole image (here V=+2.5 V). At each point, I-V curves were taken after the tip had been brought closer to the surface by 0.2-0.5 nm with the feedback loop off. These settings are chosen to avoid any topography cross-talk in the I-V spectroscopy data. Empty state topographic images of the Fe impurity investigated by I-V spectroscopy are presented in Fig. 4.12. From simple symmetry arguments and the spatial extent of the contrast, this Fe atom is supposedly located 2 or 3 monolayers below the surface. The dI/dV curves have been numerically derived from the I-V curves recorded experimentally, after subtracting the offset induced by the I-V converter. The onset of the conduction band is visible at a voltage of 1.55 V in the $\log(dI/dV)$ curve curve taken away from the Fe atom. As expected below this voltage, the signal is found close to zero and dominated by the background noise. There is no indication of the presence of an Fe impurity in the close vicinity. The dI/dV curve taken directly on the Fe center shows two distinct peaks around +0.5 V and +1.0 V, which are attributed to two states related to Fe. The fact that the dI/dV signal does not drop directly drop to zero at energies above these two peaks is tentatively attributed to the exponential decay of the tunneling probability from the tip to the impurity states at lower energies.

The dI/dV curve reported by Richardella et al.[77] in a earlier study was taken on a single Fe impurity located in the surface layer and showed two states related to Fe in the bandgap. The peaks were found at 0.88 eV and 1.5 eV. The position of the peaks in this previous study is shifted towards higher energies with respect to the dI/dV shown in in Fig. 4.16. This difference might be explained by the different position of the Fe impurity relative to the surface as well as the strongly p-type environment of the previous study. The two peaks are interpreted as corresponding to degenerated states of the Fe state of t_2 symmetry due to the breaking of the surface symmetry. A quantitative argument supporting this supposedly very large splitting of the acceptor state is however not provided.

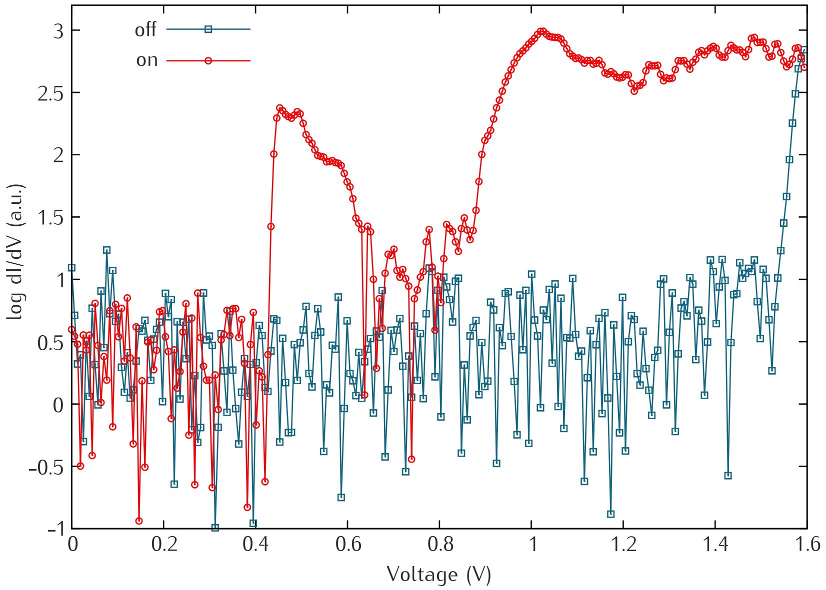

Figure 4.16: log(dI/dV) curves taken on GaAs about 5 nm away from an Fe impurity (in blue) and exactly above a sub-surface Fe impurity (in red). The onset of the conduction band is visible at a voltage of 1.55 V in the log(dI/dV) curve taken away from the Fe atom. The dI/dV curve taken directly on the Fe center shows two distinct peaks around +0.5 V and +1.0 V, which are attributed to two states related to Fe.

Instead, the explanation is supported by the odd and even symmetry of the spatial structure of the two states appearing in the differential conductance maps at the corresponding energies.

I-V spectroscopy data obtained on sub-surface Fe impurities combined to the results of the tight binding approach presents an alternative interpretation of the two peaks related to Fe in the GaAs bandgap. First, the energy difference between the two states is found to be very similar for surface and sub-surface Fe atoms in GaAs. This seems to indicate that the surface has a limited influence on the energetic position of those peaks[67]. A behavior which does not seem consistent with surface resonances. Instead, their relative position of these two peaks in the bandgap is found to reproduce qualitatively the electronic configuration for Fe in GaAs as depicted in the diagram in Fig. 4.6. The lower energy peak would correspond to the empty state of e symmetry, 510 meV above the valence band edge, while the high energy peak would correspond to the empty state with t_2 symmetry, 880 meV above the valence band edge.

A spatially resolved I-V spectroscopy experiment was performed on the same Fe impurity at 4 K. A 7.5 nm wide $dI/dV(x, V)$ cross-section taken across the Fe impurity along the [001] direction is shown in Fig. 4.17a. The two peaks are visible in the bandgap. $dI/dV(x, y)$ maps taken at 0.46 V and 1.02 V, energy positions corresponding to the two peaks, are presented in Fig. 4.17b. The spatial extent of these two states is clearly different. The lower energy state is strongly localized

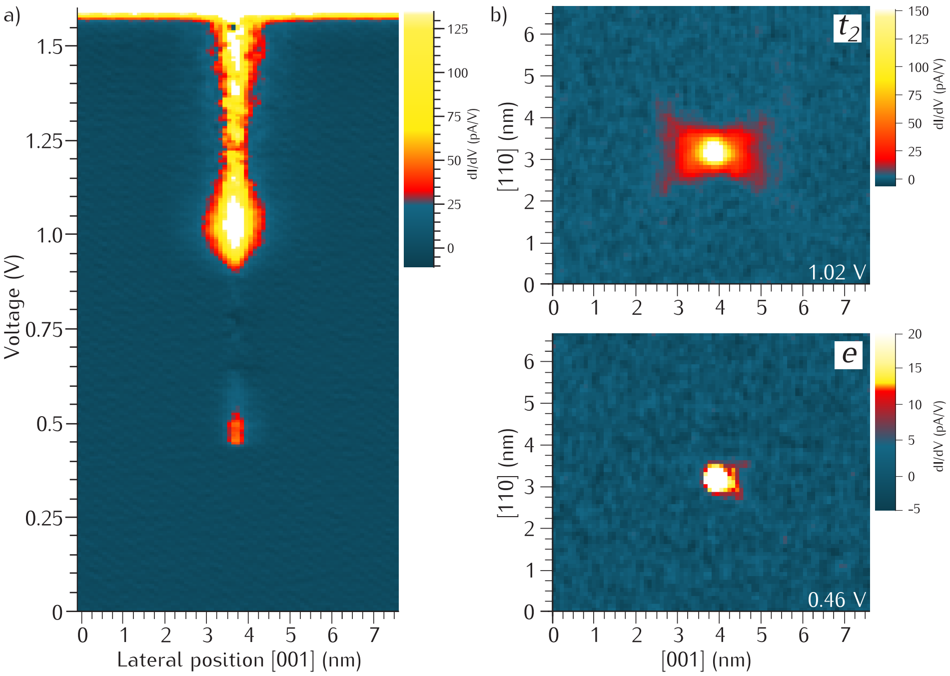

Figure 4.17: Spatially resolved I-V spectroscopy experiment was performed on the same Fe impurity at 4 K. a) $dI/dV(x, V)$ cross-section taken across the Fe impurity along the [001] direction. Two peaks are resolved in the bandgap. b) $dI/dV(x, y)$ maps taken at 0.46 V and 1.02 V. The spatial extent of these states is consistent with those expected for the deep Fe states of e (lower energy) and t_2 symmetry (higher energy).

on the Fe impurity itself. The wave function of this state is almost isotropic and extend over $\approx$ 0.75 nm. Two small features can be seen extending in the $[00\bar{1}]$ direction. The shape is very similar to the one expected for the deep Fe state of e symmetry, from the group theory and the tight binding calculation presented in Fig. 4.15. The higher energy state is also mainly localized on the Fe impurity itself but presents extensions in a cross-like shape, like the one expected for the deep Fe state of t_2 symmetry, from the group theory and the tight binding calculation presented in Fig. 4.15. . The wave function of this state is anisotropic and extends over $\approx$ 2.5 nm along the [001] direction and 2 nm along the [110] direction.

Figure 4.18 allows to compare directly the experimental $dI/dV(x, y)$ maps taken at 0.46 V and 1.02 V with the results of the tight-binding calculations. The spatial extent of experimental and theoretical density of states are very similar. Differences could be attributed to a difference in depth. These two states do not exhibit the even and odd symmetry expected for states resulting from a splitting of the t_2 state by the effect of the reconstructed surface. Instead, the shape and the spatial extent of this state is consistent with the one expected for the deep Fe states of t_2 symmetry from the group theory and the tight binding calculation

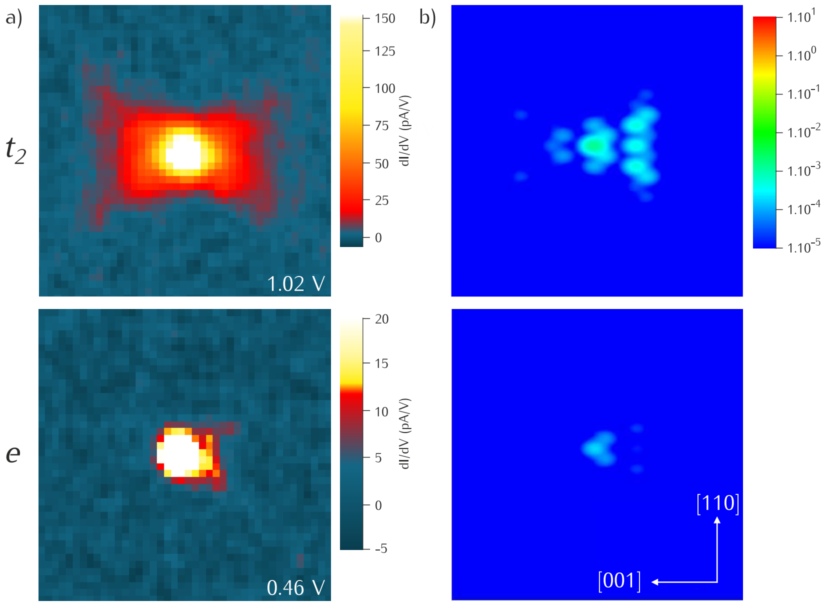

Figure 4.18: a) 3 nm×3 nm experimental $dI/dV(x, y)$ maps taken at 0.46 V and 1.02 V on a single Fe impurity at 4 K. b) 3 nm×3 nm plots of the calculated real space probability density of the d states of t_2 (top) and e (bottom) symmetry, three atomic planes away from a single Fe impurity.

presented in Fig. 4.15.

To summarize, two energy levels related to Fe have been resolved the bandgap of GaAs by means of I-V spectroscopy. From the relative energetic position of these two Fe states and their spatial extent, they are here attributed to the Fe states of e and t_2 symmetries for the lower and higher energy respectively. The good agreement between the experimental localization of these states and the theoretical one provided by tight-binding calculations suggests that the wave function anisotropy observed in the spectroscopy data can be directly linked to the symmetry of the orbitals as described by the group theory.

4.4 Internal transitions on a single Fe impurity in GaAs upon tunneling.

4.4.1 Experimental evidences for internal transitions

A new and peculiar electronic contrast related to Fe was observed at low negative voltages, as shown in the filled states topography image of Fe atoms in Fig. 4.19. In this image, taken at the exact same position as Fig. 4.9, three Fe impurities are visible. The main characteristics of this new electronic feature are the dark contrast on a brighter background, the clear anisotropy and the asymmetry.

Similar anisotropic shapes, but with bright contrast, have been reported for

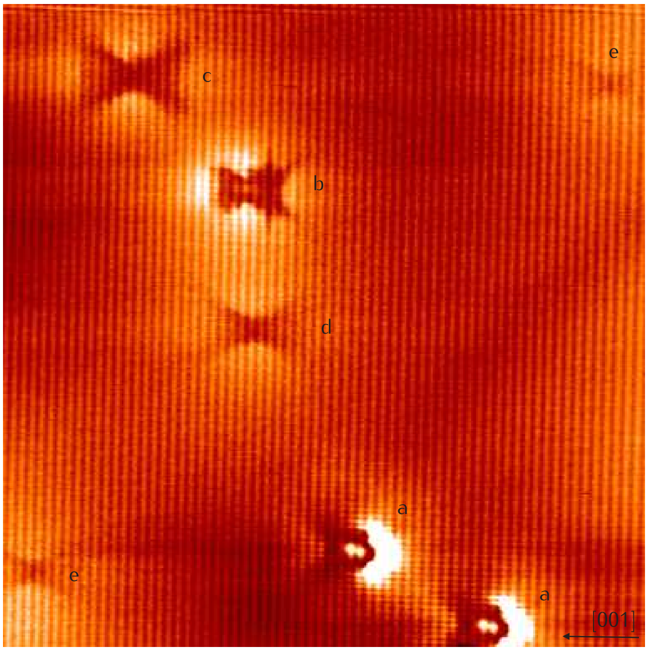

Figure 4.19: 45 nm ×45 nm filled states topography image showing several Fe impurities located at different depth below the surface. Each impurity is labeled with a letter. The alphabetical order indicates their position from the surface towards the bulk.

the wave functions of holes bound to individual acceptors in GaAs[17,52]. Bound hole wave functions are imaged at low positive voltage, when electrons can tunnel from the tip to the empty acceptor state and appear as bright anisotropic features. The anisotropy of the contrast originates from the cubic symmetry of the host crystal[17], and the asymmetry is related to the interaction with the surface and the binding energy of the acceptor[93]. In the previous section, it has been shown that the wave function of the core state of Fe with t_2 symmetry can also be at the origin of the such anisotropic contrast . The resemblance is particularly striking for the Fe impurity at the surface, indicated by (S) in Fig. 4.19, exhibiting the highly anisotropic and asymmetric shape reported of an Fe impurity in the surface layer[77]. Consequently, this new contrast is presumably related to the acceptor levels of Fe in GaAs and the variation in shape from one Fe atom to the other is attributed to the depth dependence of the charge distribution contrast, as shown for Mn impurities in GaAs[56].

A set of 7 nm ×8 nm filled states imaged taken a negative voltages on a single Fe impurity is shown in Fig. 4.20. The shape of this feature for a single impurity is very sensitive to the tunneling conditions. The brighter background is the signature of a Coulomb potential resulting from the negatively charged state of Fe. This positive contribution to the tunneling, caused by charged state of the impurity, is partially compensated a the negative contribution in the form of this peculiar dark feature. The strong dependence of the dark shape on the bias

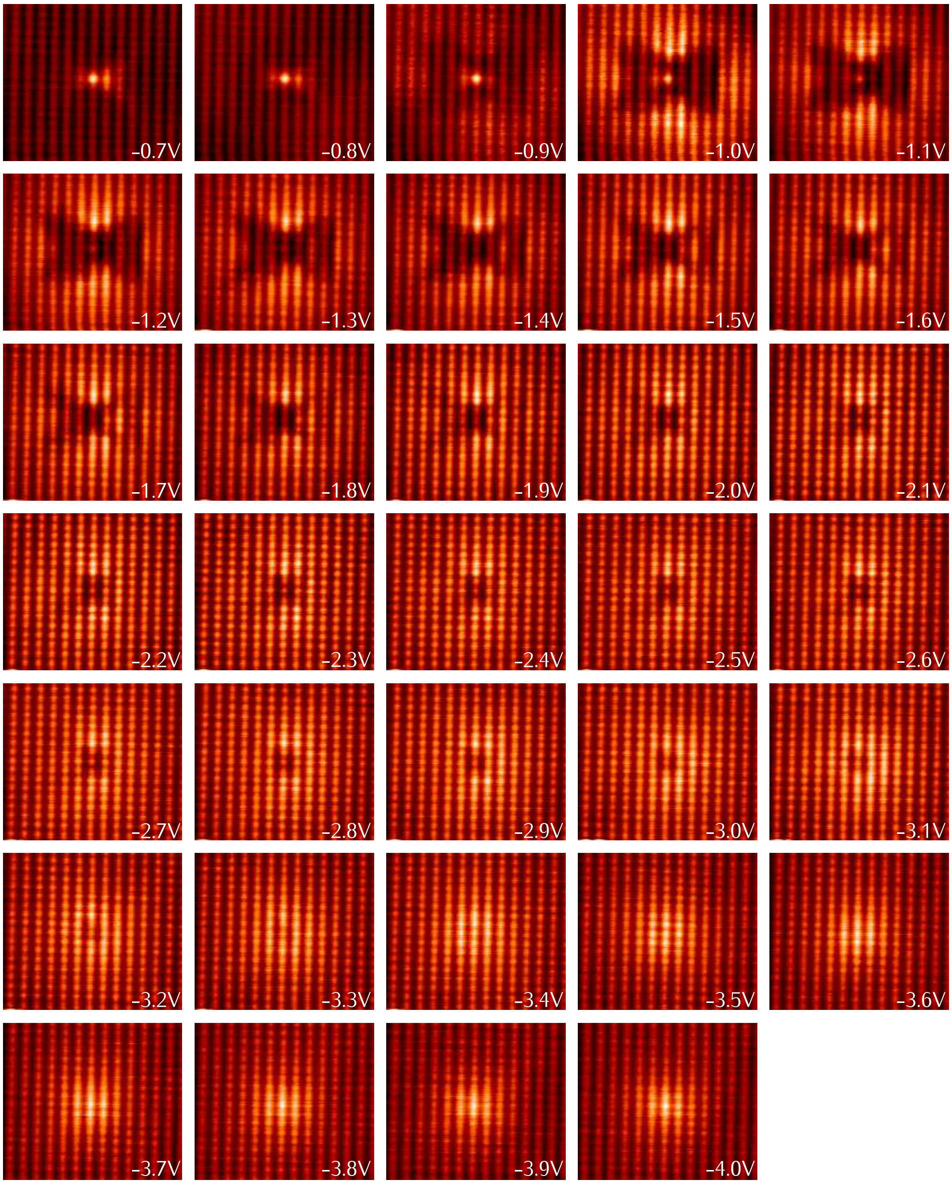

Figure 4.20: 7 nm ×8 nm filled states topography images of the same Fe impurity located deep below the surface in GaAs, taken at different negative voltages. The dark feature corresponds to a decrease in conductivity. Its anisotropic shape becomes smaller and more asymmetric as the voltage, *i.e* TIBB, becomes larger.

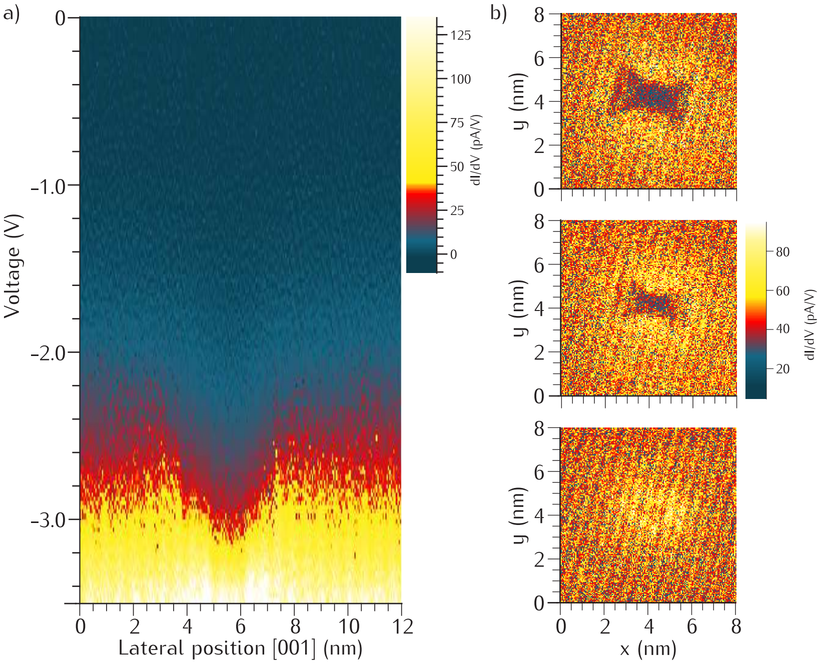

Figure 4.21: a) $dI/dV(x,V)$ cross-section taken across the Fe impurity along the [001] direction. The suppression of the tunneling current and its voltage dependence is clearly visible. b) 8 nm ×8 nm $dI/dV(x,y)$ maps taken at -2.7 V, -3.0 V and -3.4 V. The dark feature disappears at higher voltages. The bright Coulombic background is present over the entire voltage range.

voltage is very specific to this new contrast. As shown in the previous section, wave function imaging does not involve such strong dependence. At high negative voltages, only the Coulomb contribution to the contrast is visible. Going towards lower negative voltage, the spatial extent of the decrease in conductivity becomes larger and more symmetric. The same dependence is found when decreasing the current setpoint or increasing the laser power when illuminating the sample. This dependence can be understood as a consequences of the bending of the semiconductor bands as explained for the core state manipulation in section 2 of the current chapter. Fig. 4.21a presents a $dI/dV(x,V)$ cross-section taken over a single Fe atom. The decrease in tunneling current at the position of the Fe impurity and the voltage dependence discribed above appear clearly. $dI/dV(x,y)$ maps taken at -2.7 V, -3.0 V and -3.4 V, on a single Fe impurity, are displayed in Fig. 4.21b. A Coulomb field is present over the entire voltage range and the spatial extent of the tunneling current reduction matches the one seen in the filled states images in Fig. 4.20.

Decreases in conductivity appearing at a single impurity in filled states topography images are rare and only a few electron tunneling mechanisms have been reported that can account for it. The contribution to the tunneling current of an inelastic tunneling path is small and positive. However within the framework of inelastic electron tunneling spectroscopy, for single magnetic adsorbates[94] or single molecules[95] on a metallic surface, decreases in tunneling current have been observed. In the case of a magnetic atom, the LDOS directly above the impurity can be reduced by tunneling through Kondo resonances which develop due to the screening of the moment localized on the magnetic adatom. The phenomenon we observe is particularly robust (present at room temperature) hence Kondo-like resonances in our system are unlikely. Instead our interpretation draws on observations of a decrease in tunneling current due to interference between two elastic tunneling paths through a single molecule, one path virtually exciting a vibrational resonance[96–99]. Here we consider a similar scenario in which two distinct elastic paths from the tip to the sample interfere: one passing directly through without disturbing the Fe impurity core electrons, and one virtually exciting an electronic transition from the e to the t_2 crystal-field-split states in the d shell. This suggested mechanism is based on the Fe^{2+} electronic configuration of the Fe impurity at negative voltages attested by the bright Coulomb contribution to the contrast. In this configuration the lower energy level e is occupied, whereas the t_2 is left empty.

4.4.2 Theoretical framework

The coupling of an electron with a virtual transition in the core states of Fe from the e state to the t_2 state acts as perturbation to the carrier injection. This alternative injection path interfering with the direct injection path could be the cause of the decrease in tunneling current observed at negative applied voltages. Considering the suggested origin of this peculiar contrast and using a similar formalism as Persson *et al.*,[98], the contribution of a second elastic path that virtually excites the core exciton, $\partial I/\partial V$, normalized to the path that does not excite the core exciton, can be written similarly as:

$$\begin{aligned}\frac{\partial I}{\partial V} = {} & \frac{\delta\epsilon^2}{(E_a - E_{f,s})^2 + (\Gamma/2)^2} \\ & \times \left[\frac{(E_a - E_{f,s} + \omega)^2 - (\Gamma/2)^2}{(E_a - E_{f,s} + \omega)^2 + (\Gamma/2)^2} \Theta\left(V + \omega\right) \right. \\ & \left. + \frac{1}{\pi} \frac{(E_a - E_{f,s} + \omega)\Gamma}{(E_a - E_{f,s} + \omega)^2 + (\Gamma/2)^2} \ln\left|\frac{V+\omega}{\Delta}\right| \right] \end{aligned} \tag{4.1}$$

where $\delta\epsilon \sim 0.35$ eV is a measure of how much the acceptor level energy, E_a, changes due to the virtual excitation of the core Fe electron, $\Gamma = 0.2$ eV is the width of the acceptor state E_a, $E_{f,s}$ is the position of the Fermi level at the surface of the sample, $\omega = 0.37$ eV[100] is the energy splitting of the e and t_2 Fe d-level states, $\Delta \ll \Gamma$ is a cutoff energy, and V is the applied voltage. The value of $\delta\epsilon$ has not been calculated, however the energy of the exciton is 0.3 - 0.4 eV and it is plausible that the shift of the electron state E_a will be similar to this energy difference between the$e$ and t_2 states of Fe. This expression for the interfering contribution is valid for regions where the non-exciting path is the

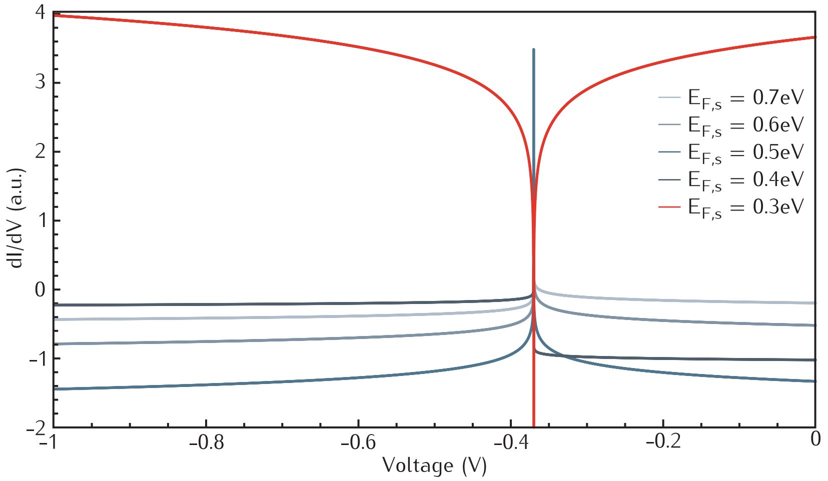

Figure 4.22: Calculated contribution to dI/dV from the tunneling path that virtually excites a core exciton, in units of the dI/dV from the tunneling path which does not involved the excitation and for several potential values of the Fermi energy $E_{f,s}$. Parameters and the quantitative expression used are described in the main text. Negative values indicate a suppression of the tunneling current. The calculated wave function of the lowest-energy core *d* state, of *e* symmetry, using the formalism of Ref.[68] is shown in the inset.

dominant feature. The path that does not virtually excite a core exciton yields a feature in the dI/dV that is a relatively wide Lorentzian centered around $-E_{f,s}$, and thus it is the dominant feature in the dI/dV for a range of $E_{f,s} \pm 0.2$ eV.

This results in the dI/dV plot of the virtual-exciton-exciting path $\partial I/\partial V$, normalized to the non-exciting path, shown in Fig. 4.22. In this figure, there are two main trends of interest. The first is the transition of the height of the spike near $eV =$ -0.37 eV (corresponding to the energy splitting of the e and t_2 Fe d-level states) from negative to positive. This switch occurs for an increase in $E_{f,s}$. The second trend is the decrease of the dI/dV in voltage regions outside the main feature. This decrease happens for an increase in $E_{f,s}$. The switching of the spike from negative to positive does not substantially affect the topography due to the narrow voltage range of the peak, however, the decrease in the other regions of $\partial I/\partial V$ has a substantial effect because it demonstrates that for a large range of negative voltages the Fe image should be dark relative to its surroundings. The large range of voltages for which the calculated $\partial I/\partial V$ is negative and should produce in topographic maps a dark region (relative to surroundings) with roughly has the size and shape of the t_2 core state wave function, support the interpretation for the dark anisotropic shapes shown in Fig. 4.20, To conclude, the peculiar dark and anisotropic electronic contrasts shown in Fig. 4.19 are consistent with the presence of interference between two elastic tunneling paths. These interferences are suggested to arise from the virtual and internal excitation of carriers between the occupied level of e symmetry and the empty level of t_2 symmetry. This phenomenon has not been reported for shallower impurities studied by STM and STS. It is however suggested that impurities with two deep levels or more in the semiconductor bandgap could give rise to such feature.

To summarize, the STM and STS studies of single Fe impurities in GaAs showed that tightly-bound core states can be electrically manipulated by means of TIBB. The observation of a disc around single Fe atoms in filled states images is a clear manifestation of a change in charge and valence state of the Fe impurities from $(\mathrm{Fe}^{3+})^0$ to $(\mathrm{Fe}^{2+})^-$. The isoelectronic Fe^{3+} configuration, imaged at positive voltages, is the neutral state of the Fe acceptor. This statement is supported by the STS data indicating the presence of two levels attributed to Fe in the bandgap of GaAs. The relative position of these levels in is good agreement with the one established from optical spectroscopy experiments[85,86]. Moreover, the good agreement between the experimental localization of these states (Fig. 4.17) and the theoretical one provided by tight-binding calculations (Fig. 4.15) suggests that the anisotropy observed in the spectroscopy data can be directly linked to the symmetry of the orbitals as described by the group theory. The spatial mapping of the wave function of deep core d-states of an impurity by itself represents a stimulating achievement in the field of single impurities in semiconductors. The evidence of internal transition occurring on the Fe acceptor upon tunneling complete this solid picture of the energy levels of Fe dopants in GaAs. In view of being the most precise, it should be mentioned here that only 20% of the Fe impurities showed directly a clear presence of e and t_2 levels in the bandgap and the associated contrast in empty states images. The remaining 80% showed a different electronic contrast not reported here. The attribution of this other contrast to Fe impurities is made straight-forward by the observation of switching between these two contrasts. This alternative state of Fe may result from a non-substitutional position of Fe in the GaAs lattice. Further investigations are however required to support this idea.

chapter 5

Droplet Epitaxy of GaAs quantum dots in AlGaAs

This chapter presents a study at the atomic scale of GaAs/AlGaAs self-assembled quantum dots (QD) grown by Droplet Epitaxy (DE). The morphology of these GaAs/AlGaAs DE-QDs was investigated by means of Atomic Force Microscopy (AFM) and cross-sectional Scanning Tunneling Microscopy (X-STM). Unlike for Stranski Krastanov-QDs, the GaAs/AlGaAs DE-QDs shape can be finely tuned by an accurate variation of the growth parameters. This advanced control over QD aspect ratio and exposed facets allowed for a straight forward model for the main mechanism governing the relationship between QD shape and several growth parameters based on Ga diffusion dynamics and crystallization during the exposure of the Ga liquid droplet to the As flux. Besides this general picture, peculiar crystallization phenomena occur that have been studied by X-STM and Atom Probe Tomography. Finally the effort made to achieve a precise height control GaAs/AlGaAs DE-QDs by engineering the capping layer is presented.

5.1 Quantum Dots and Droplet Epitaxy

Amongst the most relevant advancements in nanoscience an important place is taken by quantum confinement effects taking place in semiconductor nanostructures. The small dimensions of these heterostructures, typically tens of nms, lead to quantum confinement in different dimensions. One dimensional confinement is achieved layers called semiconductor quantum wells (QW) and two dimensional confinement is obtained in semiconductor nanowires (NW). Three dimensional confinement is obtained in semiconductor nano-islands called quantum dots (QDs). QDs show a discrete spectrum of energy levels and can therefore be considered as artificial atoms[101]. Unlike and beyond natural atoms, QD electronic properties can be finely tuned by adjusting parameters like dimensions, shape or chemical composition. Both single-particle and many-particle aspects of the electronic properties show a complex dependence on the structural properties of the QD[13,14]. The origin is not only the simple quantum-confinement physics but reflects also directly electronic structure effects such as interband, intervalley, spin-orbit and strain-induced state coupling[102,103]. Working on the QD shape allows thus for the engineering of the QD electronic states in order to effectively extend the performance of various optoelectronic devices[104], ranging from room temperature QD-based inter-subband detectors[105] and lasers[106] (the latter because of the hindering, obtained via QD electronic energy tailoring, of the electron–phonon scattering[107,108]), to semiconductor optical amplifiers[109], polarization controlled single photon emitters for quantum communication systems[110] and QD based photovoltaic cells[111].

Different approaches exist for the fabrication semiconductor quantum dots. The first approach described here is the chemical synthesis from precursor compounds dissolved in solution resulting in the so-called colloidal semiconductor nanocrystals, typically between 2 and 50 nm in size. The great advantage of this technique is its scalability which makes this method promising for commercial applications. However, despite a lot of efforts, the optical properties of these QDs are affected by spontaneous changes in the emission brightness under continuous optical excitation, referred to as "blinking" which limit their field of application. The second approach consists in using nanolithography techniques, like photolithography or nano-imprint to etch the nano-islands out of a bulk layer. With this so-called top-down approach, spatially ordered nano-islands, typically 20–500 nm are created with a specific pattern. This technique shows great reproducibility but the QDs suffer from defects created by the consecutive lithographic steps. In particular the QD interfaces are very rough and impurities are likely to contaminate the direct QD environment. In these first two approaches, the poor quality of the interfaces are generally found to be very detrimental for the optical functionality of the nanostructures.

The third approach relies on the self-assembly of semiconductor heterostructures. Semiconductor crystals can be grown by epitaxial techniques like Molecular Beam Epitaxy (MBE) or Metal Organic Chemical Vapor Deposition (MOCVD). One of the most common methods for self-assembled QDs fabrication is the epitaxy of lattice-mismatched semiconductor materials via the Stranski-Krastanov (SK) mode[112]. SK exploits the self-assembly of pyramidal-like QDs driven by the relaxation, above a critical thickness, of strain accumulated in the epilayer. Despite the high success of this technique which led to consequent fundamental physical understandings and to a large variety of applications[112–114], the available degrees of freedom in their fabrication remain limited[115] owing to the energetic driven evolution of the SK-QD shape[116]. This technique applies exclusively to lattice-mismatched heterostructures and the geometry of resulting QDs is mainly determined by the thickness of the initial layer, the lattice mismatch and the growth temperature. This leads to QDs with specific dimensions and facets. Sharp transitions from one QD geometry to the other (pyramid, dome) are found which correspond to abrupt changes of their optoelectronics properties. SK-QD self–assembly may be overcome by Droplet Epitaxy (DE), a MBE based growth procedure for the self-assembly of III-V semiconductor nanostructures[117–119].

The DE procedure is based on the subsequent deposition of III and V column elements at specific temperatures and fluxes (the first in form of nanometer scale

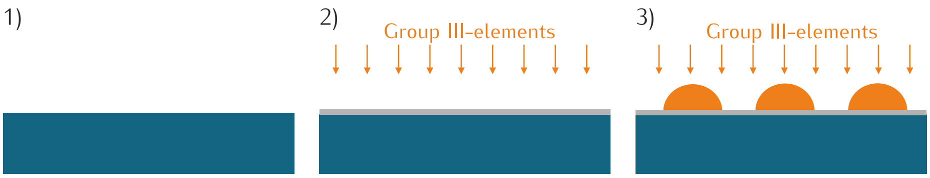

Growth of a barrier at nominal conditions followed by the decrease in temperature and a depletion in group V-elements.

Supply of group III-elements. Depending on the type of surface reconstruction, the first monolayers are crystallised in a thin layer.

Additional supply of group III-elements leads to the formation of liquid group III-elements nano-droplets.

Supply of group V elements resulting in the complete crystallization of the droplets into QDs.

Capping of the QDs at intermediate temperature followed by an annealing step at nominal temperature.

Completion of the barrier with capping at nominal conditions.

Figure 5.1: Schematic illustration of the steps in Droplet Epitaxy.

droplets), allowing for a good control over composition and assuring a large flexibility in nanostructure shape design[19–24,120–124]. The different stages of Droplet Epitaxy are schematically depicted in Fig. 5.1.

The following steps describe the details of the growth of QDs by DE.

1) A barrier is grown under the standard conditions of pressure and temperature ($T \approx 580^\circ - 600^\circ$). The temperature of the crystal is then lowered to $T = 200^\circ$-400° . Simultaneously the group V-element flux is stopped and the background group V-element pressure drops below 1×10^{-9} Torr.

2) A flux of group III elements is supplied and the group III-atoms are deposited on the barrier material. According to the surface termination, a fraction of group III atoms crystallize into a thin III-V layer (between 0 and 2 ML typically).

3) The additional supply of group III elements leads to the formation of liquid Ga droplets. The dimensions and the density of the group III-elements droplets are controlled by the group III-element flux and the volume deposited and the substrate temperature.

4) A flux of group V element is supplied which changes the surface reconstruction and crystallizes the Ga droplets into GaAs quantum dots. Note that this is the most crucial step of the DE procedure. The morphology of the final nanostructure is largely determined by the group V element flux and the crystallization temperature at that stage[123–125].

5) The QDs are annealing ($T = 300^\circ - 500^\circ$) and subsequently capped with a barrier material at intermediate temperature ($T = 400^\circ$) for a few tens of nanometers.

6) The growth of the barrier is completed at normal conditions of temperature and pressure.

5.2 Controlling the DE-QD morphology

The system investigated here are GaAs quantum dots in AlGaAs. Because GaAs and AlGaAs are lattice matched materials, GaAs QDs can not be obtained by the SK growth mode. In comparaison, DE allows the fabrication of strain-free GaAs QDs. This particularity allows for QDs with an electronic structure free from strain. Structural properties are then the most relevant factors in determining the optoelectronic properties. In the following section, X-STM and AFM techniques are used to characterize systematically QDs obtained by varying the parameters like the volume of Ga deposited (step 3), the As flux and the crystallization temperature (step 4). The effect of the capping is also investigated.

5.2.1 Experimental study

5.2.1.1 Growth

The DE-QDs in this study were grown in the group of Stefano Sanguinetti at the Milano-Bicocca University and in the group of Takaaki Mano at the National Institute for Materials Science in Tsukuba. DE-QDs were grown by MBE on GaAs (001) substrates. After the growth of a 100 nm $Al_{0.3}Ga_{0.7}As$ buffer layer, DE was performed, which consists of (1) the Ga droplet formation by a supply of Ga without As flux (background As pressure below 1×10^{-9} Torr) and (2) their crystallization into GaAs by a supply of As_4 flux. Three sets of samples (P, T and V) were grown in this study. For sets P and T, identical Ga droplets were formed by a supply of 2.5 ML Ga at 350°C. In set P, droplets were crystallized at 200°C by a supply of different As beam equivalent pressure (BEP) ranging from 2.5×10^{-5} Torr to 5×10^{-6} Torr. In set T, the As BEP was fixed at 1×10^{-5} Torr while the droplets were crystallized at different substrate temperatures ranging from 150°C to 250°C. In set V, droplets of various sizes were crystallized under the identical conditions (supply of As (BEP 1×10^{-5} Torr) at 200°C). The droplet size was varied by depositing 2 to 2.5 ML of Ga at 250°C–350°C. Within set V, a series of QDs with capping layer (V_{cap}) was grown following the standard procedure for obtaining highly luminescent QDs, *i.e.* an uncapped annealing at 400°C and a post-growth rapid thermal annealing at 750°C. In this subset, the Ga droplets were formed by a supply of 1.5 to 5 ML of Ga at 200°C and subsequently crystallized at 200°C under an As flux of 2.5×10^{-4} Torr. This subset is of special importance as it allows us to investigate the QDs after capping in their final state. For each set, a detailed description of growth parameters can be found in Table 5.1.

The MBE growth of all samples was monitored *in-situ* by Reflection High Energy Electron Diffraction (RHEED). For all sets of samples, a $c(4\times4)$ reconstruction was clearly visible in RHEED patterns before Ga deposition. In all

Table 5.1: Growth parameters of the different sets of samples. Set P: variation in As BEP. Set T: variation in crystallization temperature. Set V: variation in Ga droplet volume. Set V_{cap}: variation in Ga droplet volume and capping procedure.

Set	P	T	V	V_{cap}
Ga supplied (ML)	2.5	2.5	V1 = 3 V2 = 2 V3 = 2.5	V1 = 1.5 V2 = 2 V3 = 3 V4 = 5
Ga deposition T (°C)	350	350	V1 = 350 V2 = 350 V3 = 220	200
As BEP (10^{-5} Torr)	P1 = 5 P2 = 2.5 P3 = 1 P4 = 0.75 P5 = 0.5	1	1	25
Crystallization T (°C)	200	T1 = 150 T2 = 175 T3 = 200 T4 = 225 T5 = 250	200	200
Crystallization time (s)	180	180	180	10
QD density (cm^{-2})	6×10^8	6×10^8	6×10^8 to 1×10^{10}	2×10^{10}

sets, after that 1 ML of Ga was incorporated on the As terminated surface, a Ga terminated surface appeared in RHEED pattern. The remaining volume of Ga deposited formed liquid Ga droplets. The single ML of Ga required to subsequently onset the droplets formation as well as our experimental conditions[126] indicate that the $c(4 \times 4)\alpha$ phase is the most probable reconstruction at the initial stage. In the temperature and As pressure ranges explored, complete crystallization of the Ga droplets into GaAs QDs occurs along with the formation of a thin GaAs layer less than a bilayer thick[127].

5.2.1.2 AFM

All samples were characterized by AFM in tapping mode using ultra-sharp tips with a 2 nm radius. The evolution of the QD morphology with the As pressure is shown in the 300 nm×300 nm AFM images of a typical QD of three samples of set P found on Fig. 5.2a). The corresponding height profiles are shown below each image. The evolution of the QD morphology with the crystallization temperature is presented in the 300 nm×300 nm AFM images of typical QDs of three samples of set T in Fig. 5.2b. The corresponding height profiles are shown

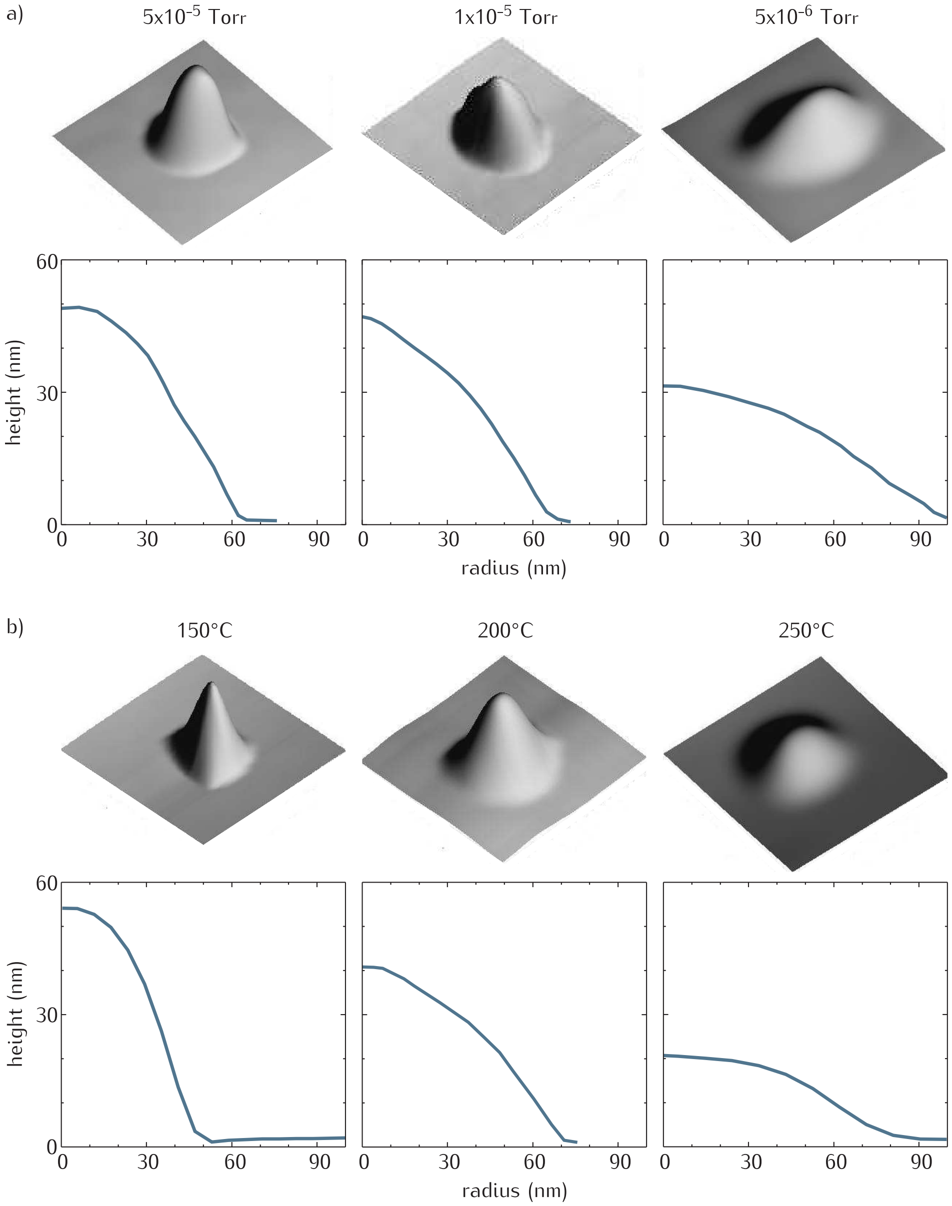

Figure 5.2: 300 nm×300 nm AFM images of QDs grown at different a) As pressures (set P) and b) crystallization temperatures (set T) along with their corresponding AFM profiles

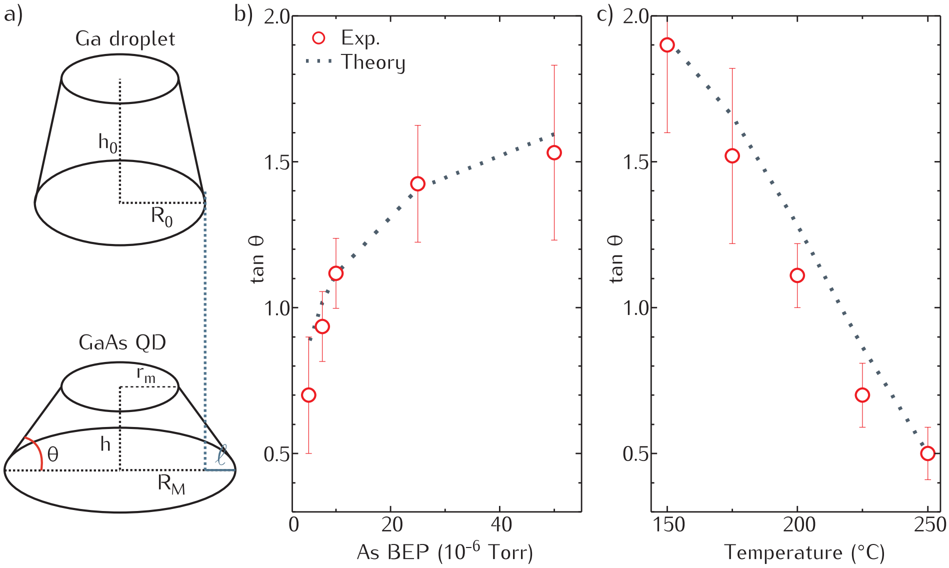

Figure 5.3: a) Schematics of the truncated Ga droplet and its evolution in QD with increasing radius R_M due to Ga diffusion onto the surface. ℓ is the diffusion length of Ga. Plots of the tangent of the angle θ, between QD surface and substrate, as a function of b) As BEP (set P) and c) crystallization temperature (set T). The dotted lines indicate the theoretical prediction based on the model.

below each image. Although starting from identical Ga droplets (sets P and T), the QDs show a broad range of dimensions. QD heights vary from 20 nm to 55 nm and QD diameters range from 100 to 200 nm. The QDs have an approximately truncated circular conical shape. At high As flux and low crystallization temperature, the QDs have a high aspect ratio. When the As flux is decreased and/or the crystallization temperature increased, the QD aspect ratio decreases and the QDs become slightly elongated along the $[1\bar{1}0]$ direction. None of the QDs have straight facets. The lower part of the QDs has steep and well defined exposed facets. The slope of the upper part however decreases gradually while the top is generally flat. The slope of the lower part is defined by the tangent of the angle θ between QD surface and substrate, as illustrated in Fig. 5.3a). Its strong dependence on the the As flux and crystallization temperature are shown in Fig. 5.3b and c respectively.

The slope of the side facet increases with increasing As flux and decreasing crystallization temperature. Only the QDs from sets P and T were compared here as they originate from identical Ga droplets. The initial Ga droplets in set V are different and allow us to study the evolution of the QD morphology for identical crystallization conditions but different sizes. The evolution of the QD morphology with the volume of Ga deposited is shown in the 300 nm×300 nm AFM images of a typical QD of three samples of set V found in Fig. 5.4. The aspect ratio of the QDs increases with increasing amount of Ga deposited. The variation in QD geometry observed for sets P, T and V results from a gradual variation of QD dimensions

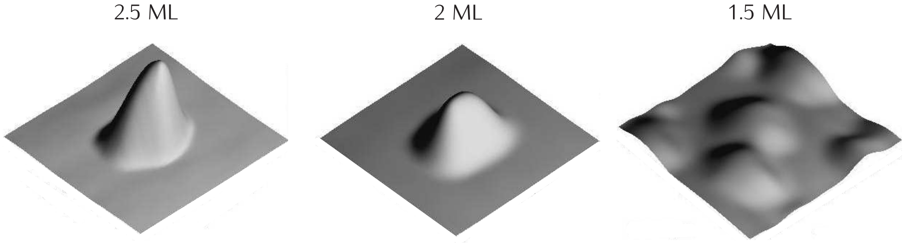

Figure 5.4: 300 nm×300 nm AFM images of QDs grown from different volume of Ga deposited.

and aspect ratio. This is very different from the case of SK-QDs, where the change in morphology occurs in abrupt steps between well-defined stable facets. The smooth evolution of the DE-QD profile with the growth parameters is an advantage for the engineering of its electronic properties. However, the QD becomes only functional upon capping and after a rapid thermal annealing step. Whether the DE-QDs maintain their morphology upon capping and annealing is of crucial importance. In fact, the capping layer has proven to affect strongly the final morphology of the QDs in the case of SK-QDs, where the capping layer can be engineered in order to control the QDs height and shape[128]. Where AFM does not allow to study capped QDs, X-STM was used to answer this question.

5.2.1.3 STM

The serie V_{cap} was investigated by X-STM performed at room temperature and 77 K under UHV conditions (5×10^{-11} Torr). The STM was operated in constant current mode on clean and atomically flat (110) and ($1\bar{1}0$) GaAs surfaces obtained by *in-situ* cleavage.

Topographic images of a typical QD for different volumes of Ga are shown in Fig. 5.5a-d. All the images were recorded at negative bias voltages (-2.5 V). At these tunneling conditions and with the color scaling used, Al atoms give a darker electronic contrast than Ga atoms. Hence, the AlGaAs matrix (ternary compound) appears as an inhomogeneous region while large, bright, homogeneous regions correspond to the GaAs nanostructures (binary compound). Four QD layers grown from different volume of Ga were studied and 167 QDs were analyzed. First of all, height profiles like in Fig. 5.5e taken across the QDs do not show any relaxation of the cleaved surface. This implies that the nanostructures are strain-free as expected for lattice-matched AlGaAs/GaAs heterostructures.

Also, independently from the volume of Ga used, it is difficult to resolve the thin GaAs layer between the QDs, which forms when the substrate is first subjected to the flux of Ga. This layer is 2 ML thick at maximum, which is in agreement with Ga deposition on a $c(4 \times 4)$ reconstructed surface as observed by RHEED.

The dimensions of the QDs were determined along the [$1\bar{1}0$] and [110] directions. This analysis is made under the assumption, supported by the AFM data (see inset Fig. 5.7), that the size distribution of the QDs is small. And if the QDs are approximately of equal height, the height and diameter distribution observed

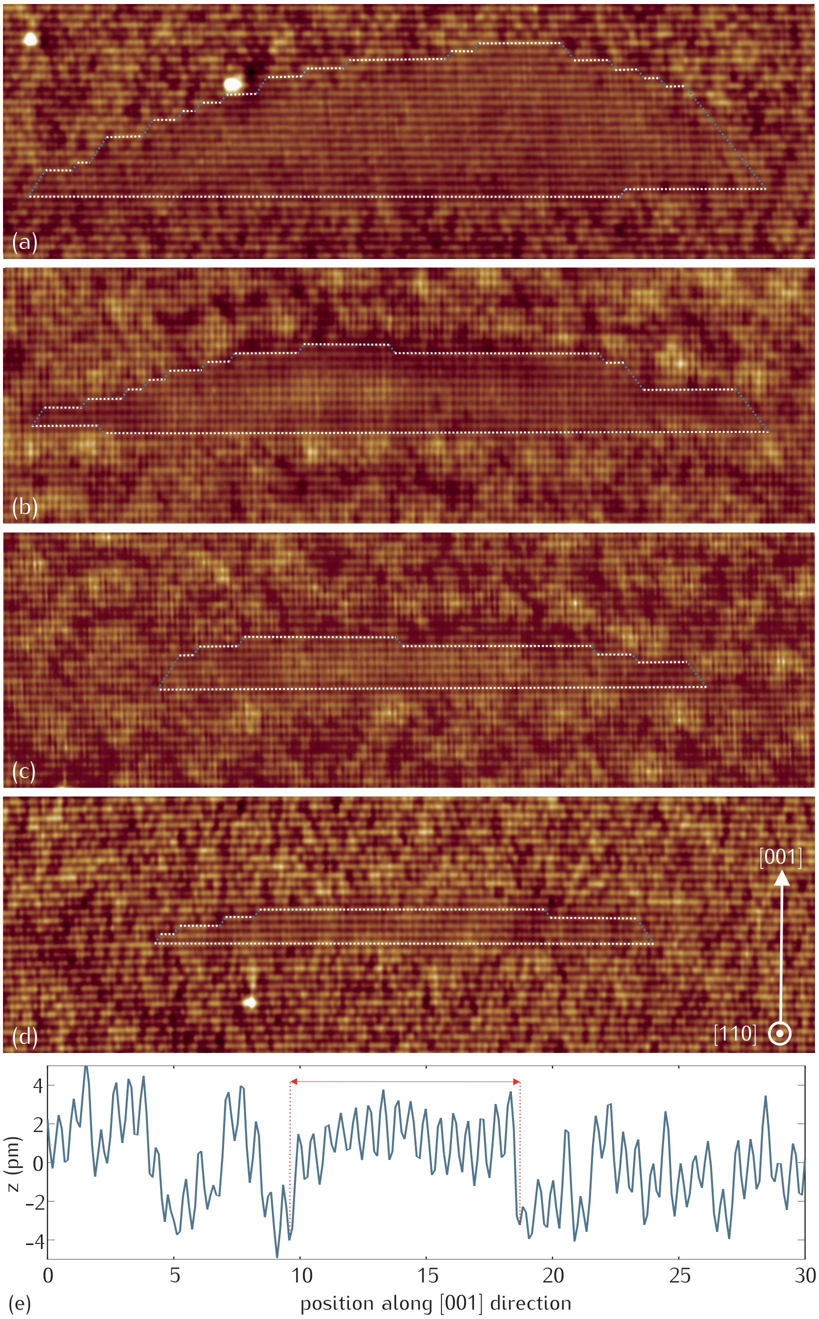

Figure 5.5: 53 nm × 17 nm filled states topography images of QDs for (a) 1.5 ML, (b) 2 ML, (c) 3 ML and (d) 5 ML of Ga. The images correspond to 2D cuts close to the center of the QDs. (110) facets are outlined in white and (111B) facets are outlined in blue. e) STM height profile taken across a QD (indicated by the red arrows) along the [001] direction. The surface is not relaxed and the variation in height has an electronic origin.

in the cross-sectional STM images is due to the random position of the cleavage plane relative to the center of each QD.

In this perspective, the highest QDs observed are considered as cut through their center. This way, a QD height of 12 ML (3.4 nm), 16 ML (4.5 nm), 26 ML (7.3 nm) and 44 ML (12.4 nm) can be respectively attributed to 1.5 ML, 2 ML, 3 ML and 5 ML of Ga deposited as shown in Fig. 5.6a. The QD diameter along the [110] direction increases with the volume of Ga from 35 nm for 1.5 ML Ga to 50 nm for 5 ML. Furthermore an elongation of the diameter is observed in the $[1\bar{1}0]$ direction with respect to the [110] direction (see Fig. 5.6b). The variation in QD dimensions for different volumes of Ga deposited is expected as the initial Ga droplets have different sized. However, the variation in height is stronger than the variation in diameter. This leads to a change in aspect ratio along the [110] and $[1\bar{1}0]$ directions as illustrated in the Fig. 5.7, where the QD aspect ratio is plotted against the volume of Ga deposited. In each direction, the aspect ratio depends non-linearly on the volume of Ga. The difference between the [110] and the $[1\bar{1}0]$ directions reflects the elongation of the QDs along the $[1\bar{1}0]$ direction Because of the arbitrary position of the cleavage, defining the exact shape of the QDs is difficult and has to be done carefully. In the X-STM images, it clearly appears that the QDs exhibit a (001) top facet. The absence of triangular shaped cross-sections and the fluctuations of cross-section base diameters for each layer exclude the possibility of truncated pyramidal QDs. This indicates a truncated shape with a circular base instead of a squared base, consistent with the approximate truncated cone shape deduced from the AFM observations. Moreover, as the volume of Ga increases, the aspect ratio dispersion in the cross-sectional STM cuts increases strongly indicating that: (i) small QDs proportionally have a wider (001) top facet, (ii) the QD sides are not straight, (iii) the angle θ is not constant. All these points are in agreement with the observations made on the single QD STM images shown in Fig. 5.5. Resolving the facets QDs is challenging due to the weak contrast at the interfaces. However, as reported in literature[129] and shown in Fig. 5.5a-d, the GaAs DE-QD facets can be described by a combination of alternating (001) facets (white lines) and (111)B facets (blue lines). The (001) facets are wider for a low volume of Ga (1.5 and 2 ML) than for a high amount of Ga deposited (3 ML and 5 ML). As a result the number of (111)B facets is much higher for the QDs with an high aspect ratio. The comparison at the nanoscale of the AFM and X-STM data regarding QD dimensions and overall QD morphology reveals that the shape and size of the QDs are not altered upon capping. Additionally the STM study shows that the gradual change in QD profile is made possible at the atomic scale by varying the number of (001) and (111)B exposed facets.

5.2.2 Analytical model and discussion

The DE-QD aspect ratio and side facet angle appear to continuously vary in the range 0.04–0.4 and 10°–62° respectively, as a function of the crystallization conditions (AFM data). This is a peculiar characteristic of DE-QDs. In SK-QD systems, like SiGe/Si and InAs/GaAs, well-defined transitions between aspect ratio and facet configurations are shown as a function of the deposited volume[130–132].

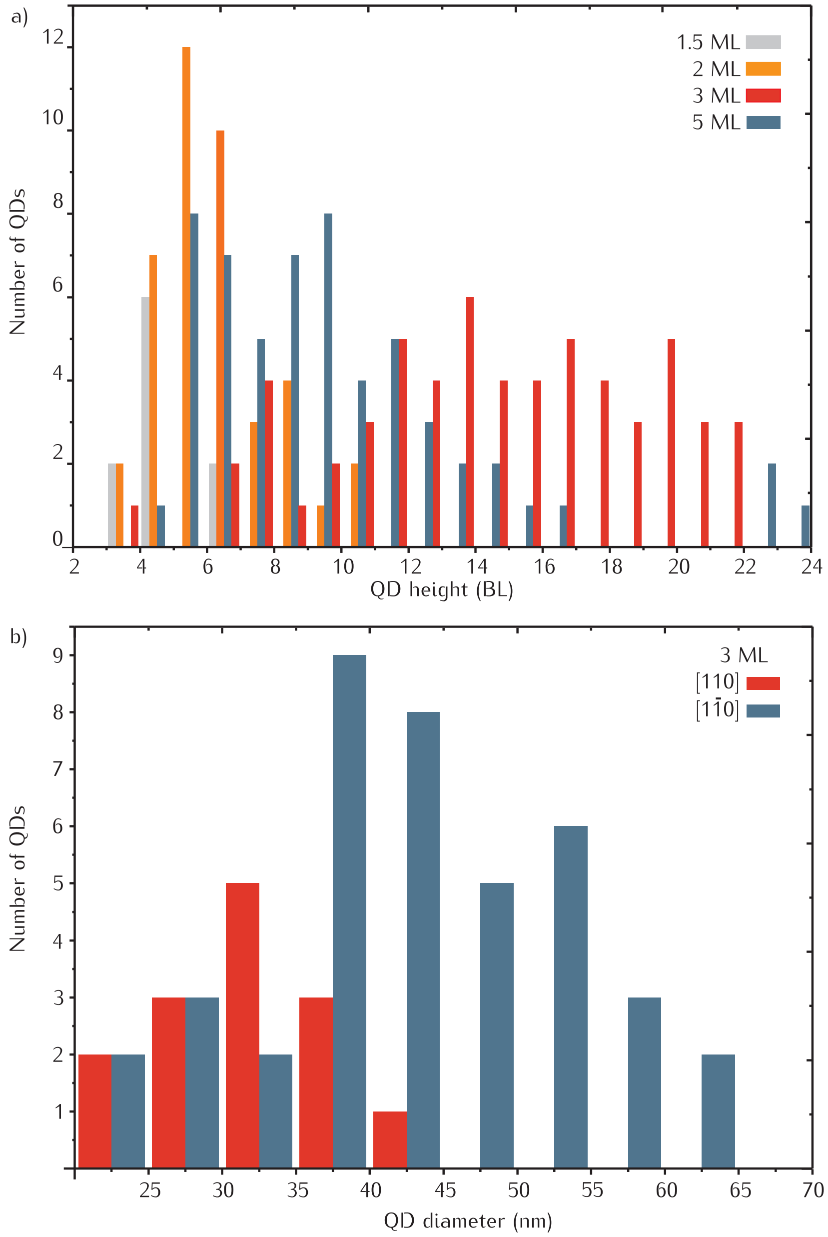

Figure 5.6: QD dimensions determined from the cross-sectional STM images. a) Height distribution of the GaAs QDs for different volume of Ga. b) Diameter distribution along the [1$\bar{1}$0] and [110] directions of the GaAs QDs grown from 3 ML of Ga deposited . The large distributions reflect the cuts off QD center.

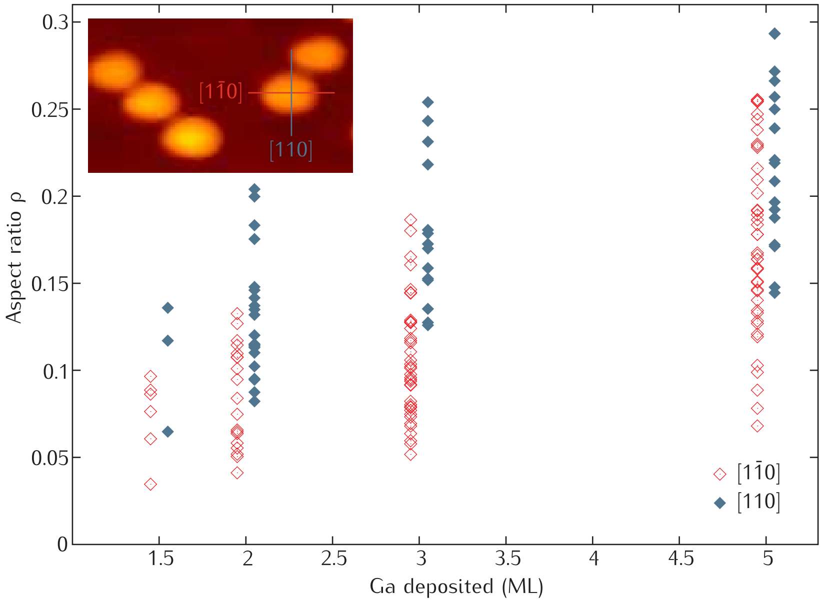

Figure 5.7: Aspect ratio as function of the volume of Ga deposited for all the capped QDs analysed by X-STM along the [110] direction (closed symbols) and $[1\bar{1}0]$ direction (open symbols). The aspect ratio depends non-linearly on the Ga volume. The dispersion increases with the volume of Ga indicating that: (i) small QDs proportionally have a wider (001) top facet ,(ii) the QD sides are not straight, (iii) the angle θ is not constant. The difference between the [110] and the $[1\bar{1}0]$ directions reflects the elongation of the QDs along the $[1\bar{1}0]$ direction also seen in the inset. This elongation originates from the anisotropic diffusion of Ga atoms. Inset: 250 nm×150 nm AFM image of the uncapped QDs for 3 ML of Ga deposited.

When a critical volume is reached an abrupt change of the island morphology from one shape to another (like from pyramid to dome) is observed. This is due to the fundamental role played by surface energetics and strain relaxation in the determination of the island shape. In SK growth mode the three-dimensional island formation is in fact favored by the strain relaxation, despite the higher surface energy. Surface energetics and strain relaxation play a fundamental role and their ratio determine the overall dot shape[132].

The smooth variation in DE-QDs aspect ratio and side facet angle within wide ranges, depending only on the crystallization conditions, suggests a minor role played by surface energetics, compared to growth kinetics, in DE-QD formation. The thermodynamically stable configuration of GaAs on AlGaAs is a 2D layer due to the high solid–solid surface tension and the lack of strain. Facet energy minimization plays only a minor role. Instead the DE-QD formation process is strongly influenced by the diffusion of Ga atoms out of the droplet towards thermodynamical equilibrium in the presence of an As flux[117,118,133]. The GaAs/AlGaAs DE-QD self-assembly relies crucially on the kinetically limited processes of crystallization and Ga diffusion[18].

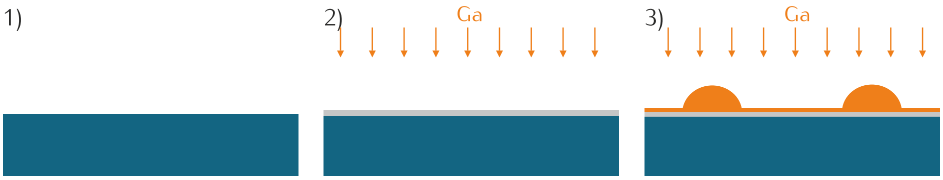

AlGaAs barrier. Surface shows a c(4x4)α reconstruction.

Supply of Ga. The first ML of Ga crystallize in a thin GaAs layer.

Supply of Ga. Remaining Ga forms liquid Ga droplet. The surface is Ga-rich.

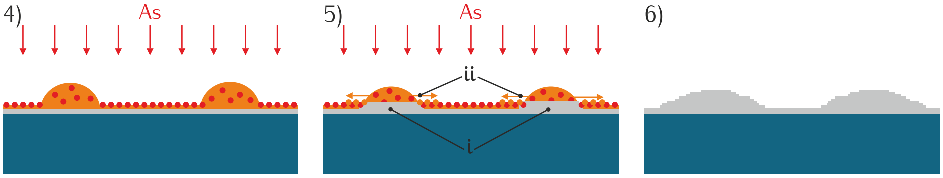

Supply of As. As atoms incorporate in the Ga droplet and change the reconstruction into an As terminated surface.

Supply of As. i) The liquid Ga droplet starts to crystallize into GaAs. ii) Ga atoms diffuse on the As-rich surface.

The entire comsumption of the Ga leads to crystalline GaAs QDs.

Figure 5.8: Schematic representation of processes and successive surface terminations during the DE of GaAs/AlGaAs QDs. A complete description can be be found in the text.

During the Ga droplet crystallization under As flux, the relative importance of two mechanisms proceeding in parallel determines the final crystal morphology: i) the As incorporation in the metallic droplet and the GaAs crystallization at the liquid-solid interface; ii) the As adsorption on the surface surrounding the droplet changing the surface termination and providing the thermodynamic driving force for the diffusion of Ga out of the droplet by capillary forces[134]. The two processes proceed in parallel until the complete consumption of the Ga contained in the droplet. Temperature and As pressure are the key parameters governing the relative importance of the two processes in DE–QD fabrication procedure. The different stages of the DE of GaAs/AlGaAs are schematically represented in Fig. 5.8. Ga adatom diffusion and Ga-As bond formation on the surface around the droplet lead to the accumulation of GaAs material within a diffusion length of Ga adatoms from the droplet edge.

The GaAs nanocrystal profile is therefore expected to be proportional to the radial dependence of the Ga diffusing from the droplet. Small diffusion lengths result in QDs[18], whereas large diffusion lengths compared to the droplet radius lead to a complete change of shape, e.g. disks and rings[19,123,125]. In the latter case the dynamics of the surface reconstruction play a fundamental role[125]. The AFM and X-STM characterization presented here show the possibility to influence the QD morphology to obtain different shapes and aspect ratios by properly tuning the growth conditions which influence both crystallization and diffusion dynamics.

In view of all these considerations, the main physical parameter governing the QD formation is the diffusion length of Ga $\ell = \sqrt{4D_{Ga}\tau}$, which depends on temperature and As flux through the diffusivity constant $D_{Ga} = D_0 \exp(-E_A/kT)$, where E_A is the activation energy of the diffusion process and τ the lifetime of the Ga adatoms. Droplet epitaxy being a As limited growth mode[18], the Ga adatom lifetime is $\tau = N_s/J_{As}$, where N_s is the number of surface sites and J_{As} the atomic As flux[135]. The experimental data suggests that the accurate control of the Ga diffusion length, via temperature and As flux allows to finely tune the QD shape and dimensions.

In order to test this hypothesis, numerical simulations were performed based on a diffusion model adapted to DE by Stefano Sanguinetti and compared to the experimental QD profiles. The idea is that the geometrical QD profile is proportional to the concentration profile of Ga diffusing from the droplet. The initial Ga concentration profile is $P(r) = A(r)/\xi$, where $A(r)$ is the experimental profile of the sample crystallized at the lowest temperature and highest As flux and ξ the proportionality factor. This allows to implicitly take into account the complex crystallization dynamics inside the metallic Ga droplet[134,136]. The QD radial profile, as a function of ℓ is then given by[137]:

$$C(r,\ell) = \frac{2\xi}{\ell^2} \exp\left(\frac{-r^2}{\ell^2}\right) \int_0^\infty P(r') \exp\left(\frac{-r'^2}{\ell^2}\right) I_0\left(\frac{2rr'}{\ell^2}\right) r' dr'. \tag{5.1}$$

In this analysis, the anisotropy of the Ga diffusion is neglected[138]. In the definition of ℓ on an As terminated surface, $D_0 = 0.2$ cm^{2}s^{-1} and $E_A = 1.0$ eV[139]. The only fit parameter in the simulations was the sticking coefficient σ of As_4, required to convert our As_4 molecule flux into J_{As}. The result was $\sigma \approx 1$. This value is reasonable considering that in DE-QD the growth front, due to the low temperature and high As flux, may be composed of areas with high density of edges and steps which can therefore be considered close to an "ideally rough" surface[140]. In Fig. 5.2, this diffusion model is compared to the experimental results for the series P and T series. The description of the shape evolution given by the model is in excellent agreement with experimental data. This validates the proposed hypothesis about the fundamental process determining the dependence of QD shape on growth parameters.

Through the simplification of the QD morphology, the model of the nanostructure evolution with temperature and As flux can be fit parameter free. From the analysis of the AFM and X-STM images, the QD shape is approximated by a truncated cone (see Fig. 5.3), where R_M and r_m are its major and minor radius and h its height. The QD volume V is related to the volume of the liquid Ga droplet V_0 and radius R_0 via the relation $V = \beta V_0 = \beta\gamma R_0^3$. Assuming that each Ga atom in the droplet contributes to the formation of the dot, β is the ratio $\beta = V_{GaAs}/V_{Ga} = 2.31$ between the volume $V_{GaAs} = 4.52 \times 10^{-29}\,\mathrm{m}^3$ of a GaAs molecule inside the GaAs crystal and the atomistic volume of Ga in the liquid droplet $V_{Ga} = 1.96 \times 10^{-29}\,\mathrm{m}^3$. The proportionality constant γ between the volume and the radius of the droplet is set by the contact angle between the metallic Ga and the substrate is $\gamma = 0.7$ in our experiment.

From the AFM and X-STM QD profiles, a proportionality between the major and minor radius of the DE-QDs is found: $r_m = \alpha R_M$, being $\alpha = 0.45$. This approximation is valid except for a low volume of Ga deposited.

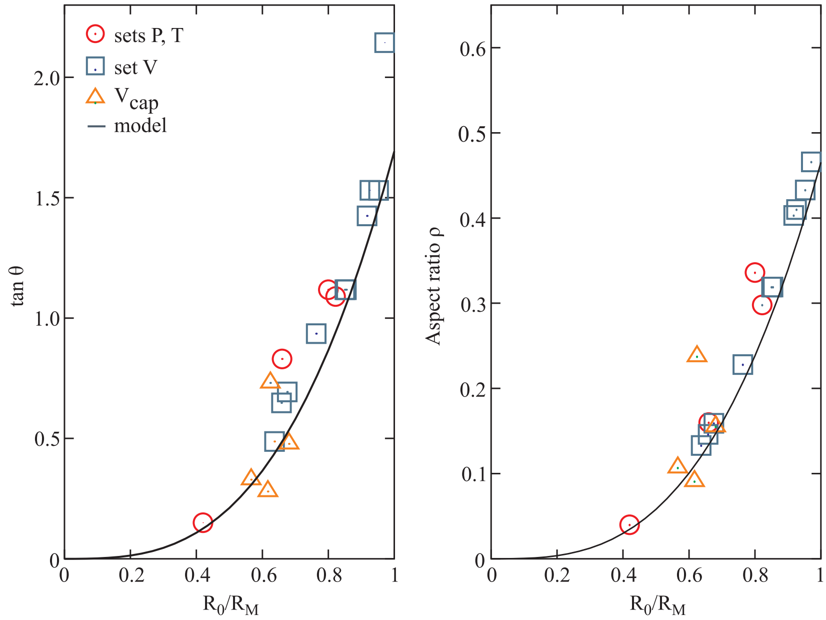

Figure 5.9: Left panel: facet angle θ and right panel: aspect ratio ρ as a function of the R_0/R_M ratio for the sets P and T (circles), V (square) and the serie V$_{cap}$ (triangle). The continuous line is the theoretical prediction obtained using Eq. (5.3).

As explained earlier, the As supplied to the liquid Ga droplets system changes a Ga-rich surface to an As terminated surface, where the Ga diffuses away from the droplet to wet the surface nearby before crystallizing there. Under As pressure, this Ga diffusion increases the radius of QD base by a diffusion length: $R_M = R_0 + \ell$. Changing the diffusion length ℓ via temperature and As flux, at constant QD volume V, directly affects QD height and facet through the dependence of R_M on ℓ. Increasing the QD radius reduces the QD height and consequently the QD aspect ratio $\rho = h/2R_M$ and the facet angle θ. With simple geometrical considerations, θ and ρ can be expressed as a function of the ratio of two observable quantities, the droplet (R_0) and the QD (R_M) radius:

$$\tan(\theta) = \frac{3}{\pi}\frac{\beta\gamma}{(1-\alpha^3)}\left(\frac{R_0}{R_M}\right)^3, \tag{5.2}$$

$$\rho = \frac{3}{2\pi}\frac{\beta\gamma}{(1+\alpha+\alpha^2)}\left(\frac{R_0}{R_M}\right)^3. \tag{5.3}$$

The agreement between the predicted behavior and the experimental data of θ and ρ for sets P and T, shown in Fig. 5.9, is remarkable and indicates the correct assumption for the QD shape.

The dependence of the DE-QD shape on the QD volume, was reported by Heyn *et al.*[21]. Here, the full reliability of this analytic model in the case of volume variation was tested by the analysis of the set of samples V. In this series, the diffusion length is fixed (same crystallization conditions) but not the droplet volume, changing thus the relative importance of the diffusion contribution through R_M. Theory and data are in good agreement in the whole volume range (Fig. 5.9). The continuous change in faceting can be understood by considering the ratio R_0/R_M in Eq. (5.3). At fixed ℓ, a small droplet radius R_0 leads to small values for ρ and θ. Whereas if ℓ is variable and the initial droplet volume V_0 is fixed, the aspect ratio is smaller when the diffusion is enhanced (higher T and lower As BEP). Consequently, no sharp transition on the dependence of ρ and θ on the QD volume are observed, as expected for a system driven by energy minimization.

The continuous transition between high symmetry surfaces is a peculiar feature of the DE, attributed to the stepped nature of the DE-QD exposed facets, as shown by the X-STM data. Side facets appear to be a combination of alternating (001) terraces separated by (111)B steps. Angles θ between 54° and 10° are obtained by an extension of (001) terraces and a reduction of (111)B steps when moving from high to low angle surfaces, allowing the system to expose minimal energy surfaces. Angles above 54°, observed when $\ell \approx 0$, may stem from the additional presence of $\{100\}$ or $\{110\}$ steps.

It is worth noting that the post droplet crystallization *in-situ* annealing procedure performed on sample V_{cap} induces a slight change in the QD morphology related to thermally activated mass transport processes driven by the out-of-equilibrium state of DE-QDs[141,142]. Strong modification of the QD morphology has been reported for SK-QDs[143]. In the DE case Ga diffusion is also the key process driving the morphological change of the QD and leads to the elongation of the dot in the $[1\bar{1}0]$ direction. By controlling the temperature and the time of the *in-situ* annealing, it is possible to control the QDs anisotropy and aspect ratio[141,142]. For functional QDs, as in sample V_{cap}, two diffusion processes should then be taken into account: i) the Ga diffusion during crystallization described earlier (ℓ_{cry}); ii) the Ga diffusion during *in-situ* annealing in the two orthogonal directions [110] and $[1\bar{1}0]$($\ell_{ann}^{[110]}$ and $\ell_{ann}^{[1\bar{1}0]}$). Each of them contribute to the total $\ell = \ell_{cry} + \ell_{ann}$, the latter giving rise to the observed QD anisotropy. From the As pressure and the substrate temperature during crystallization and annealing, $\ell_{cry} \approx 2$ nm[139], $\ell_{ann}^{[1\bar{1}0]} \approx 12$ nm and $\ell_{ann}^{[110]} \approx 6$ nm[142]. The predicted value of $\ell_{ann}^{[1\bar{1}0]} - \ell_{ann}^{[110]} \approx 6$ nm is in good agreement with the differences between the average radius of the capped QDs in the $[1\bar{1}0]$ and [110] directions $R^{[1\bar{1}0]} - R^{[110]} = 8$ nm (see Fig. 5.6). The dependence of the average aspect ratio and facet angle of the capped QDs on the ratio R_0/R_M (here R_M is the mean value of the radius along the two orthogonal directions $[1\bar{1}0]$ and [110]) is reported in Fig. 5.9. The experimental data agrees well with the theoretical predictions, showing that also in the case of capped and annealed QDs the dot shape is determined by Ga diffusion processes. Overall, the QD morphology is maintained upon capping. The growth model proposed here is still valid after capping and rapid thermal annealing, as shown by the good fit of the STM data in Fig. 5.9. This crucial outcome is specific to DE-QDs and essential as the annealing procedure is indispensable in order to get high quality optical emission from the DE-QDs.

In this section, the ability to control QD faceting and aspect ratio of GaAs/AlGaAs DE-QDs was demonstrated. The QD shape is determined by the diffusion of Ga from the droplet on the As terminated surface during the As supply. QD faceting undergoes a continuous transition dependent on the initial droplet radius and the diffusion length of Ga during crystallization. The QD morphology is maintained upon capping. The results show that it is possible to introduce a detailed engineering of the DE-QD electronic properties, like electron state energies separation and electron-phonon interaction, via growth condition shape control. In fact, the QD shape can *a-priori* be designed on the basis of the droplet dimension and the expected diffusion length at the crystallization conditions, through the simple analytical relations introduced in Eq. (5.3).

5.3 Structural properties of DE-QDs

The study presented in the previous section focused essentially on the geometrical profile of the GaAs/AlGaAs DE-QDs. The details of the QD crystallization have been mostly neglected. Ironically as much as a high control on the DE-QD morphology is now demonstrated, the exact crystallization dynamics of the liquid Ga droplet under As flux remain uncertain and subject to debate. Most of the knowledge about the crystallization process was obtained by the systematic study the final QD morphology as a function of growth parameters like crystallization temperature and As flux[136]. In particular, the large range of growth parameters used to elaborate nanostructures by DE results in different nanostructures with specific anisotropy and elongation[19,24,124]. This allowed, among other things, to learn about the kinetics as well as the location of the crystallization of material diffusing out of the initial Ga droplet. However, the lack of *in-situ* characterization techniques able to give insight on the crystallization inside the liquid Ga is a limiting factor. So far, the only studies proposing a description of the inner crystallization are based on Kinetic Monte Carlo (KMC) simulations. With this method, different epitaxial models can be investigated taking into account both liquid and crystalline phases of DE[134].

This second section on QDs grown by Droplet Epitaxy is aimed at presenting new insights into the structural properties these QDs, like their chemical composition and interfaces. Beside the shape and the strain of the QDs, those are important factors influencing greatly the final optoelectronic properties of QDs. Moreover, chemical composition and interfaces can to a certain extent be linked to the crystallization process. For that purpose, X-STM and Atom Probe Tomography (APT) experiments have been performed on a unique QD sample. Both techniques have the particularity to provide information on the inner structure of DE-QDs.

5.3.1 Interfaces

As shown in the previous section, the GaAs/AlGaAs DE-QDs have stepped side facets which can be considered as abrupt. From earlier X-STM measurements, it already appeared that GaAs DE-QDs sometimes have rough bottom interfaces[127].

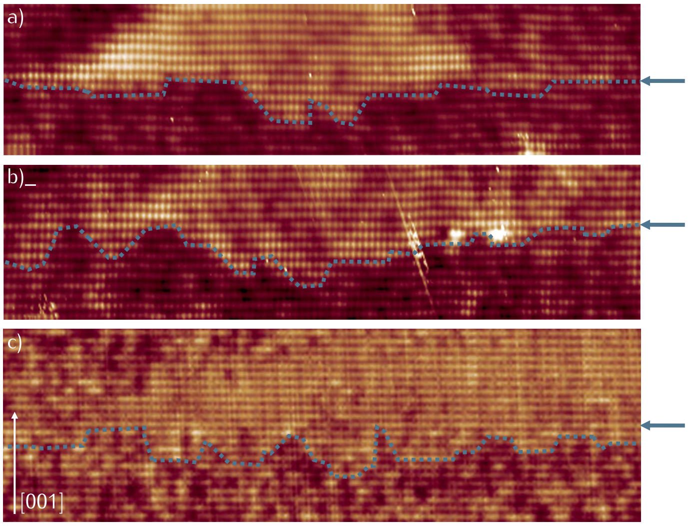

Figure 5.10: a) and b) 9 nm × 24 nm filled states topography images of the bottom interfaces of DE-QDs grown in a previous study. c) 13 nm× 35nm filled states topography image of the bottom interface of a DE-QD in the current study. GaAs inclusions are present below the QDs. Locally above those intrusions, Al atoms are incorporated inside the QD.

The most recent characterization of capped QDs (sample V_{cap}) by X-STM presented here confirms that pure GaAs QDs with abrupt interfaces are not always formed.

Fig. 5.10 presents the filled states topography images of the bottom interfaces of three GaAs/AlGaAs QDs. Fig. 5.10a and b were taken on QDs grown in a earlier study and Fig. 5.10c was taken on the recent sample V_{cap}. The growth conditions of both samples are similar. Growth conditions of V_{cap} are found in Table 5.1. QDs in the previous sample were crystallized at low temperature (200°C) and high As flux (2.0×10^{-4} Torr) resulting in high aspect ratio QDs. The only differences with sample V_{cap} are the lower capping and rapid thermal annealing temperatures, respectively 350°C and 650°C instead of 400°C and 750°C. Consequently similar observations are made. The GaAs/AlGaAs bottom interfaces are often not well-defined. Determining the transition from a ternary to a binary compound from STM topography images has to be done carefully. Nonetheless, the width of this transition clearly ranges from one bilayer to a few nanometers. Moreover, the roughness of the interface is not spread evenly along the initial growth plane indicated by arrows in Fig. 5.10. Instead the GaAs QD is composed of the crystallized droplet and additional GaAs intrusions found below the initial Ga droplet. The presence of such intrusions has been reported in systems where, like in DE, a liquid metallic droplet (In, Ga) is formed on a arsenide semiconductor surface[144,145]. Hence several models have been developed and adjusted which account for this so-called "drilling" or "etching" effect[146,147]. The mechanisms suggested for this drilling effect partially explain the diversity of the nanostructures obtained by DE[120,148].

The main process driving the etching is the dissolution of As atoms from the substrate and their diffusion into the metal droplet. As a result, an As concentration gradient forms inside the metal droplet. In the system presented here, the As atoms diffuse towards the liquid/vapor interface, after which they either escape in the vacuum or lead to crystallization into GaAs at the interface. This leads to the liquefaction of the substrate locally below the Ga droplet. This local etching of the substrate starts with the formation of the Ga droplet and proceed until its complete consumption. For this reason, a low As background favors the drilling[147]. If the environment stays completely As free, the final structure is a hole inside the substrate surrounded by a GaAs ring. If the droplet is rapidly subjected to a high As flux, like in DE, the As gradient is reduced. The metal droplet turns into a shallower GaAs QD with relatively small GaAs intrusions in the substrate.

The X-STM observations support this model. Distinct GaAs intrusions are found frequently for the largest QDs grown from 5 and 3 ML of Ga deposited, in agreement with the model and previous observations[149]. At constant As flux, the crystallization of large droplets requires a longer time leading to a stronger etching of the surface. Additionally the As gradient, which is the driving force, is the strongest in QDs with higher aspect ratio. The GaAs intrusions in the substrate are rare for smaller QDs. All the QDs, independently from the initial volume of Ga deposited, exhibit broad bottom interfaces.

A more complete investigation of the DE-QDs was achieved by using Atom Probe Tomography. This technique is able to provide a quantitative and spatially resolved chemical analysis of a semiconductor crystal at the atomic scale. A comprehensive presentation and review of this technique was written by Kelly et al.,[150]. Fig. 5.11a shows a 3D representation of the morphology of a typical DE-QD outlined by a 88% Ga iso-surface. The elongation and the anisotropy previously revealed by the scanning probe techniques are clearly visible. Fig. 5.11b shows a 2D Ga concentration map centered on the bottom interface of a DE-QD. These maps were obtained by counting the number of atoms of each species inside a volume cutting through the QD at the different positions indicated in the left panel. The color scale is linear from 30% (blue) to 100% of Ga (red) (only cations are considered here). The dotted black lines indicate an arbitrary (001) plane. Despite the lower spatial resolution of APT compared to X-STM, the bottom interface is also found to be very rough. GaAs inclusions appear below the QD, as seen in the X-STM analysis.

In both samples investigated by STM, the occurrence of these inclusions is close to 50%. Their spatial extent varies randomly from a few ML to several nanometers. As expected the high post-annealing temperature does not have a clear influence on the drilling process. This is understood by the fully crystalline structure of the GaAs QDs at that stage. The temperature seems to be the most critical during the formation of the droplet and its crystallization. The exact role of these temperatures as well as DE kinetics in parameter range resulting in QDs remain to be investigated more systematically.

GaAs DE-QDs have diameters of several tens of nms, hence the quantum confinement is the strongest along the growth direction. Fluctuations of sev-

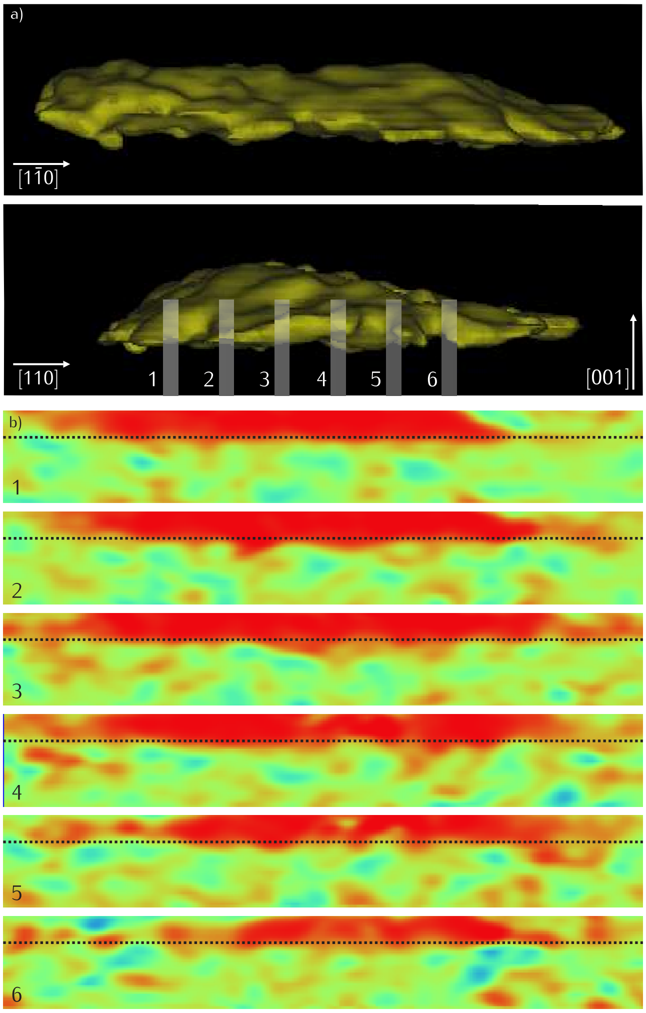

Figure 5.11: a) 10 nm×60 nm 88% Ga iso-surface in a 3D APT data set, outlining the morphology of a DE-QD grown from 3 ML of Ga. b) 15 nm×55 nm 2D Ga concentration map centered on the QD bottom interface. The color scale is linear from 30% (blue) to 100% of Ga (red). The dotted black lines indicate an arbitrary (001) plane. The interface is rough and small GaAs inclusions are present below the QD.

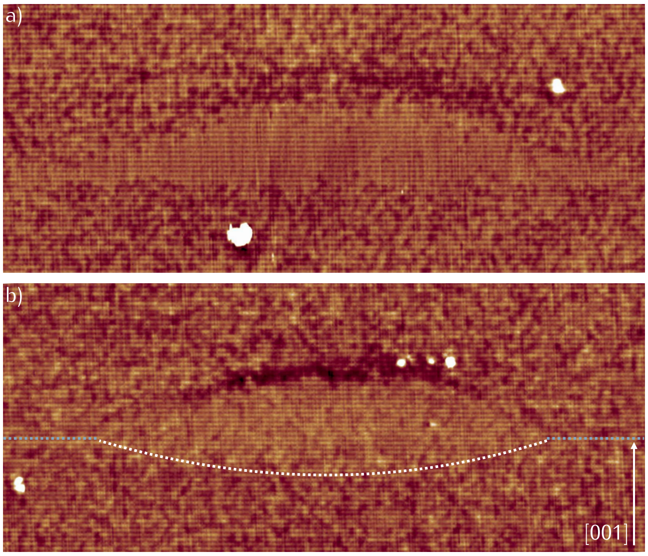

Figure 5.12: 32 nm×76 nm filled states topography images of DE-QDs grown under the exact same conditions. a) low and b) high level of Al intermixing. The dotted line indicates roughly the bottom interface of the QD.

eral nanometers in QD height arising from the etching mechanism undoubtedly compromise the final goal of controlling the optical emission of these DE-QDs. Despite the fact that the growth parameter window (As flux and crystallization temperature) will probably be reduced, efforts to suppress any drilling process should be made. On the path towards well-defined optoelectronic properties, such phenomenon can be very detrimental.

5.3.2 Chemical composition

Besides the QD morphology and the quality of interfaces, another important QD character is its chemical composition. Semiconductors bandgaps are determined by the chemical composition of their crystals. The bandgap of a ternary alloys is found to vary non-linearly with its chemical composition. The functionality of a QD is therefore directly connected to its chemical profile. SK-QDs are typically not pure binary compounds. In the case of SK InAs/GaAs QDs, an In gradient is found inside the QD ranging from 0% to 70%[151]. For comparison, InAs QDs recently grown by DE are made of almost pure InAs allowing for optical emission above 1.55 μm[121].

The large majority of the GaAs/AlgaAs DE-QDs investigated exhibit a low level of Al intermixing as shown in the STM topography image in Fig. 5.12a. As in the previous study, the concentration of Al atoms in the QDs can be estimated by overlaying a grid with the positions of the semiconductor lattice at the (110) surface on the X-STM image (not shown here). Because Al atoms give a darker local contrast than Ga atoms, it is possible to count the Al atoms present in the

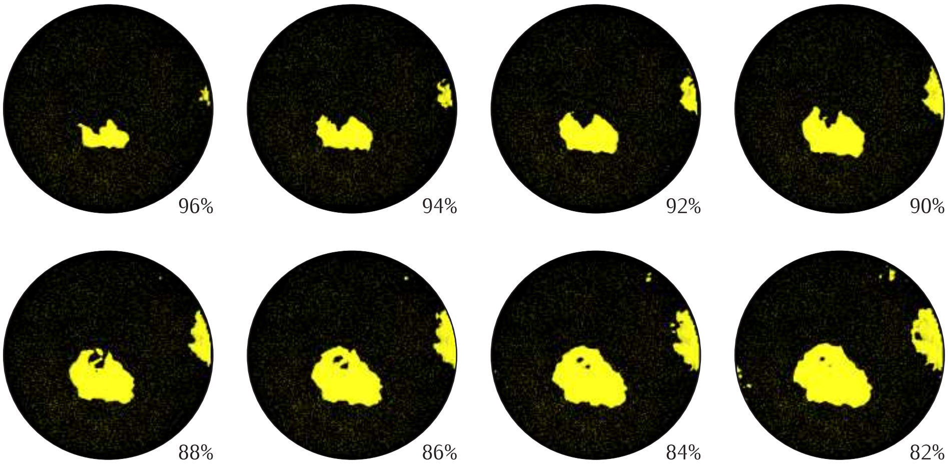

Figure 5.13: 100 nm diameter 3D APT data set presenting Ga iso-surfaces of a DE-QD grown from 3 ML of Ga, ranging from 96% to 82% of Ga. The final morphology of the QD can be determined from the 84% Ga iso-surface. The concentration in Al inside the QD varies roughly from 0% to 15%.

surface layer. With this method, from one QD to the other, Al concentrations varying between 0% and 10% were found, a range of intermixing which does not affect strongly the optical properties of the QDs. The exact Al concentration inside the GaAs QD can not be determined by the strain relaxation method presented in chapter 2 as the GaAs/AlGaAs system is strain-free. A more quantitative analysis of the Al intermixing was carried out using Atom Probe Tomography. From the APT data set, iso-surfaces of the element of choice can be plotted in 3 dimensions. Figure 5.13 shows Ga iso-surfaces, ranging from 96% to 82% of Ga, around at the position of a DE-QD (sample V_{cap}, 3 ML of Ga). The final morphology of the QD is clearly defined by the 84% Ga iso-surface. From the evolution shown in this set of images, it clearly appears that most of the Al intermixing does not take place randomly inside the QD but extends from all the interfaces. The Al content and the spatial distribution of Al atoms inside the QD can not determined by Al iso-surfaces because the concentrations are too small (less than 12% Al). For the same reason, an Al concentration gradient can not properly be defined. The APT observations are consistent with the STM data analysis. It reveals the presence of an low intermixing region at the QD boundaries which can be also be regarded as a broadening of the QD interfaces over a few monolayers.

The suggested origin of this broadening of the interfaces is the diffusion of atoms promoted by the post-growth rapid thermal annealing (RTA) step performed after the capping of the DE-QDs. This diffusion is spatially limited and does not change the core composition of large QDs, which is around 90-95% of GaAs. Additionally, Al-Ga inter-diffusion is known to take place in structures grown at low temperatures and later subjected to annealing[152,153]. The process is explained by the creation of point defects, like vacancies, in the low temperature crystal which subsequently mediate the diffusion of cations[154,155]. A broadening of the

QDs has been reported for SK-QDs were the inter-diffusion is enhanced by the presence of a strain field[143].

If most of the QDs present a low degree of Al intermixing, a small number of QD (10%) presents however a very high concentration of Al, as shown in Fig. 5.12b. For comparison, in this filled states STM image, the AlGaAs matrix around the GaAs QD contains 33% of Al. QDs with Al concentration up to 30% were found. Not only the magnitude of this intermixing is different from the Al intermixing mentioned above but also the distribution of Al atoms inside the QD is here homogenous. For these reasons and because of the large dimensions of the QDs affected, Al diffusion during RTA can not be held for the only responsible mechanism. A more careful look at highly intermixed QDs shows that their bottom interface is located up to 16 MLs (4.5 nm) below its nominal position. A dotted white line is drawn as a guide to the eyes in Fig. 5.12b. This is an observation common to all strongly intermixed QDs. A possible explanation, without further evidence, is the incorporation of Al in the QD prior to crystallization due to massive local etching as described in the previous paragraph. Along with the As atoms, Al atoms detach from the substrate and diffuse in the Ga droplet contributing this way to the drilling process. As a result a large Ga-rich region is formed in the AlGaAs substrate below the QD.

Like broadened interfaces and increased QD dimensions, the formation of alloyed QDs have a strong impact on the QD carrier confinement. A a simple example, the confinement in a AlGaAs QD with 15% Al (see Fig. 5.12b) in an standard AlGaAs barrier with 33% Al is reduced by half compared to a pure GaAs QD.

5.3.3 Ga depleted cap

Another structural feature associated to the GaAs/AlGaAs DE-QDs and revealed by X-STM and APT analysis is presented in Fig. 5.14. The color scale of the APT 2D Al concentration maps is linear from 0% (red) to 35% (blue) of Al. In both data sets, an Ga depleted AlGaAs capping layer is found to sit on top of the QDs. This local Ga depletion is found above 70% of the large QD (grown from 3 and 5 ML of Ga) imaged by STM and all QDs analyzed by APT. Very rarely, QDs grown from 2 ML of Ga deposited show such feature, whereas QDs grown from 1.5 ML of Ga do not exhibit it at all. In other words, the Ga depleted AlGaAs regions are only found above the QDs with the highest aspect ratio.

As displayed in Fig. 5.15b, only the upper part of the QD is covered by this Al-rich AlGaAs region. Moreover, the 3D APT representation of such QD shows that the anisotropy of this Al-rich region follows the anisotropy the QD.

From the APT data, the magnitude of the Ga depletion can be estimated quantitatively from the composition profile along the [001] growth direction. The concentration of each element is extracted from a cylindrical volume across the QD and the Ga depleted region. Composition profiles across QDs grown from 3 and 5 ML of Ga are shown in Fig. 5.15c. Both profiles are very similar. The QDs are made of almost pure GaAs. The Al concentration inside the QDs is lower than 5%. The absence of a step-like transition at the bottom and top interfaces confirm the broadening of the interfaces from a few monolayers to several nanometers

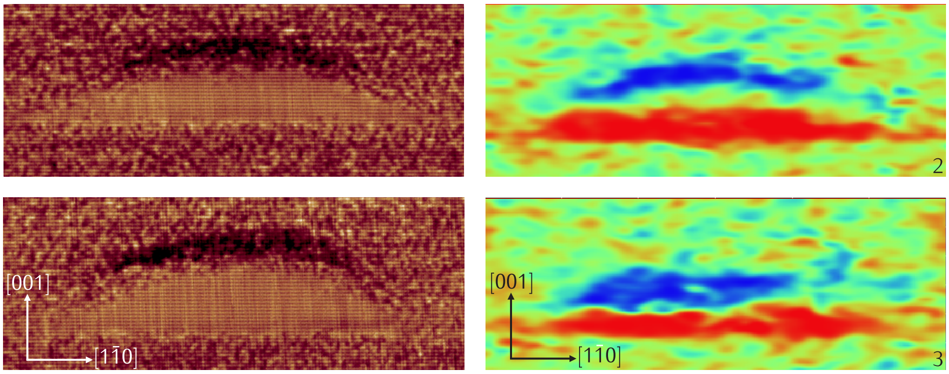

Figure 5.14: a) 28 nm×75 nm filled states topography images of 2 different DE-QDs grown from 5 ML of Ga. b) 30 nm×60 nm 2D Al concentration maps taken on one QD grown from 3 ML of Ga at different positions. The color scale is linear from 0% (red) to 35% (blue) of Al. An Al-rich region is present above the QD.

depending on the QD. The presence of a Ga depleted region above each QD is clearly visible. In both cases, the Ga content drops to 30% while the amount of Al in that region increases to 60%. The nominal AlGaAs matrix is composed of 67% of Ga and 33% of Al, hence the the Al/Ga ratio is almost exactly inverted in the depleted regions. This inversion is clearly visible in the chemical composition profiles.

A mechanism based on the difference of in Ga and Al adatom mobility is suggested. As mentioned earlier, the thermodynamically stable configuration of GaAs on AlGaAs is a two-dimensional layer due to the high solid–solid surface tension and the lack of strain. However, the high aspect ratio of the QD nanostructures confers a curvature to the growth front right on top of the QDs. This geometrical condition results in the diffusion of Al and Ga adatoms along the side facets during capping. Because Ga atoms are more mobile than Al atoms, they diffuse away from QD top to while the Al atoms remain on top of the QD. Additionally, the difference in migration may also vary depending on the side facets. This way a the AlGaAs layer crystallized on top of the QD becomes rich in Al. This mechanism explains well the highly localized position of this feature at the top of the QDs (Fig. 5.15 b) and its anisotropy. Furthermore, because this separation process continues until the growth front has flatten out, the Ga-depleted regions extend notably along the [001] direction. (Fig. 5.14 left). Additional, crystallization kinetics should undeniably play a role in the local Ga depletion of the AlGaAs capping layer.

Both in the APT data and the STM images, it appears that the Al-rich region is not directly in contact with the QD. Instead a thin layer of nominal AlGaAs is present in between. This "gap" might be explained by the broadening of the interfaces upon post-growth rapid thermal annealing. However, unlike the bottom interface of the QD, this interface is grown at higher temperature (400°C) with less points defects and the Al-Ga inter-diffusion should be limited.

To summarize, the fabrication of GaAs/AlGaAs QDs by Droplet Epitaxy is

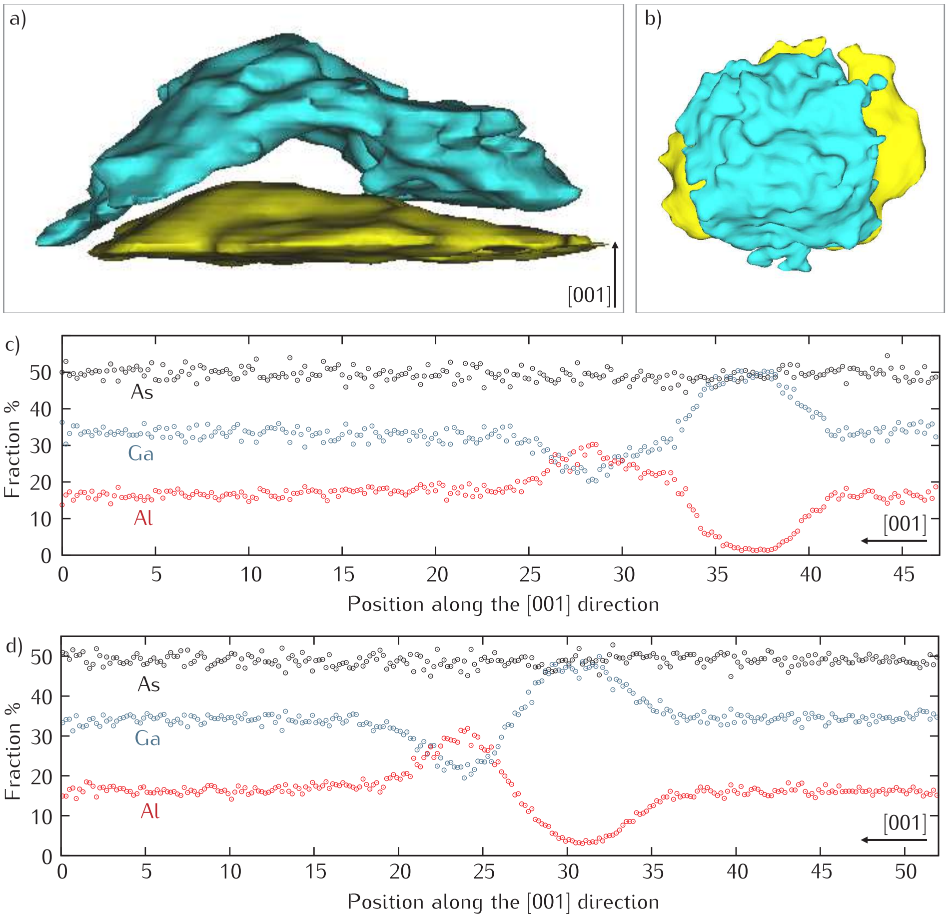

Figure 5.15: 88% Ga iso-surface (yellow) and 50% Al iso-surface in a 3D APT data set, outlining a QD grown from 3 ML of Ga, and its Al-rich cap. a) 20 nm×40 nm side view. b) 50 nm×50 nm top view. c) Ga and Al concentration profiles along the [001] direction for a QD grown from c) 3 ML of Ga and d) 5 ML of Ga. The Al-rich cap is separated from the pure GaAs by an intermixed region.

subject to phenomena altering the final dimensions and chemical composition of the QDs. Several processes have been reported which may be connected to each other; local drilling of the substrate below the QD, interface broadening, Al intermixing and Ga depletion above high aspect ratio QDs. Preventing those phenomena is essential to keep the control of the QD morphology achieved by the fine tuning of the growth parameters. From this investigation, the key factors seem to be the temperature and the kinetics of the crystallization and the annealing steps. Understanding and controlling those is expected to allow for the suppression of these unwanted phenomena.

5.4 Height control

In this chapter, the importance of controlling every structural aspect of QDs to obtain specific optoelectronic properties has been largely emphasized. It has been shown that such great control can be achieved by carefully tuning growth parameters like crystallization temperature, As flux and volume of Ga deposited. Some undesirable phenomena related to inherent or necessary steps of Droplet Epitaxy have however been observed which compromise the final QD functionality.

No clear solution to prevent the local etching of the substrate is suggested here. The main difficulty is the natural occurrence of this process in Droplet Epitaxy conditions. Changing those conditions would most certainly affect strongly the QD formation itself. The consequence of the presence of a region depleted in Ga above most of the DE-QDs has not been determined yet. However, this phenomenon is considered as detrimental. To suppress it and achieve a higher control over the QD height, a procedure is used which consists in engineering the capping layer. Such methods have been first developed in strained systems, like SK-QDs, and resulted in a major impact on the final nanostructure morphology and properties[156]. This was realized in different ways like changing the chemical nature of the capping layer[157,158], the strain field[159] or the growth scheme: by adding growth interruptions and annealing steps[160,161].

5.4.1 Experimental details

The coming section presents the application of a such method to GaAs/AlGaAs QDs grown by Droplet Epitaxy to obtain an accurate control over their height. The different steps of this engineered capping process, called flushing, are illustrated in Fig. 5.16 and described below.

1) The QDs are grown following the standard Droplet Epitaxy procedure.

2) Subsequently, the fully crystallized QDs are partially capped with AlGaAs at intermediate temperature. This means that the thickness of this capping layer is chosen to be thinner than the expected height of the QDs. As the results the QDs should be partially embedded. The top part remains exposed.

3) As the growth is interrupted, the system is left under As flux and the temperature is increased at high temperature. This step favors the dissolution of the exposed GaAs material followed by the desorption of Ga and Al atoms. Such process should result in truncating the QDs at the top position of the partial capping layer.

4) The truncated QDs are capped with AlGaAs at intermediate temperature. After which, an annealing step at normal growth temperature is performed.

5) Finally the barrier is completed by growing AlGaAs at normal growth conditions.

A sample with four different QD layers was grown to study the efficiency of the flushing procedure on DE-QDs. The first QD layer was grown in a standard way as a reference. Two other QD layers were grown using partial AlGaAs capping layers of 2 and 4 nm. The QDs in the last layer were grown on a 2 nm thick GaAs quantum well using a 4 nm AlGaAs capping layer. Overall the growth of

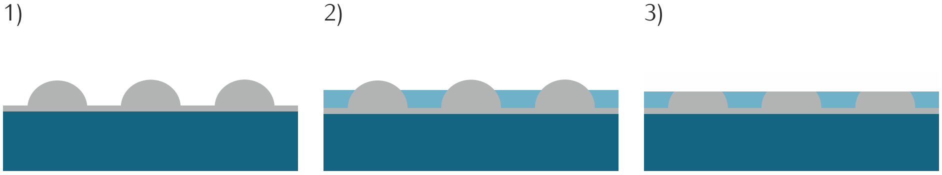

Complete crystallization of the droplets into QDs.

Partial capping of the QDs at intermediate temperature.

Annealing step at high temperature under As flux.

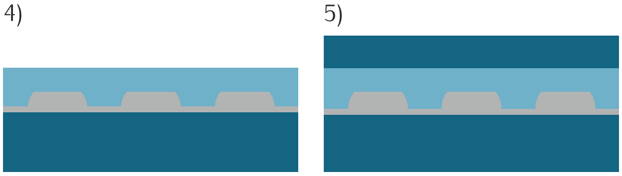

Capping of the truncated QDs at intermediate temperature followed by an annealing step at nominal temperature.

Completion of the barrier with capping at normal conditions.

Figure 5.16: Schematic illustration of the steps of the flushing procedure in Droplet Epitaxy.

these QDs before capping was done in similar conditions as in sample V_{cap} which was investigated by X-STM. The initial volume of Ga was 5 ML. The temperature of Ga deposition and crystallization temperature was 170°C and the As flux of $1.2{\times}10^{-4}$ Torr. The very low temperature was chosen to limit the prevent the 2D dimensional growth. These QDs are expected to exhibit a high aspect ratio as explained in the first section of this chapter. The QDs were capped in two distinct steps with AlGaAs at 400°C, a temperature slightly higher than for sample V_{cap}. In between the two steps, the layer was annealed at 640°C. The rest of the AlGaAs barrier was grown at 580°C. A post- growth annealing step was perform at 800°C to improve the optical properties of the QDs.

5.4.2 Structural properties of the flushed DE-QDs

Filled states images of DE-QDs grown as reference, that is with the normal capping procedure, are presented in Fig. 5.17. Like in the previous sample V_{cap}, the QDs have a high aspect ratio, consistent with the low temperature and high As pressure used for crystallization. Top and bottom interfaces are broad and Al intermixing is visible in a number of the QDs. In particular, the Al atoms are found at the bottom edges of the QDs (see Fig. 5.17). This corresponds to the position of the triple point solid/liquid/vapor which is believe to be the starting point of the crystallization process[136]. A Ga depleted region is also present above each QD. Overall the reference layer is the same as the QD layer grown from 5 ML of Ga in sample V_{cap}. For this reason and because of the poor statistics on the new QDs of reference, future comparison will be done considering the QDs in V_{cap}.

Filled states images of DE-QDs grown using the flushing capping technique

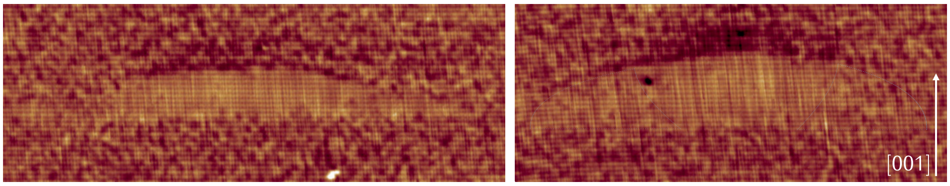

Figure 5.17: Left: 24 nm×59 nm and right: 24 nm×68 nm filled states topography images of DE-QDs grown without the flushing procedure. The white lines indicate areas with Al intermixing at the edge of the QD.

but with different capping thicknesses are shown in Fig. 5.18. The position of the bottom and top interfaces are highlighted by the white dotted lines and the distance between the two is indicated in bilayers.

The flushed QDs appear to be essentially made of pure GaAs. The frequency and degree of intermixing is much lower than for the QDs in the reference layer or in the former sample V_{cap}. Clear GaAs inclusions below the QDs can not be distinguished. Nevertheless, as shown in these images, Al atoms are visible inside the QDs close to the bottom interfaces. The bottom interfaces are therefore not well-defined. The GaAs/AlGaAs transition is not homogeneous and occurs within a few bilayers (2-5 BL). This broadening is similar to the one observed in sample V_{cap}.

Lowering the crystallization temperature from 200°C to 170°C and decreasing slightly the As flux reduces the local etching of the AlGaAs substrate. The absence of clear GaAs inclusions associated with a lower intermixing level supports the suggested connection between the two. The Al intermixing level seems to scale with the severity of the local substrate etching. Hence the high Al concentrations inside the QDs reported for the previous sample most probably originate from the AlGaAs substrate.

The broadening of the interfaces is also observed for QDs grown on the 2 nm thick GaAs quantum well. Besides, an initial surface roughness, a possible explanation is the spontaneous inter-diffusion process at GaAs/AlGaAs interface grown at low temperatures. Such process has already been reported, where the intermixing is mediated by the presence of point defects resulting from the low temperature growth. An additional argument for this idea is the relative sharpness of the GaAs QW markers present elsewhere in the sample and grown at a nominal temperature o f580°C. Unfortunately, increasing the temperature at the QD GaAs/AlGaAs interface is not an option. The low temperatures used in Droplet Epitaxy are necessary to the formation of liquid Ga nano-droplets.

The growth of GaAs DE-QDs on a GaAs QW instead of on a AlGaAs layer results in a difference in QD base diameter. The QD diameter distribution for each layer is presented in Fig. 5.19. For strict comparison, the base diameter of the QDs grown on the GaAs was measured 2 nm from the bottom interface. The dispersion in diameter for each layer is explained by the random position of the cleavage plane relative to the center of the QD. When the DE-QDs are grown on the GaAs QW, the distribution is shifted towards higher diameters. The typical diameter is found around 75-80 nm instead of 65-70 nm for the QDs grown on

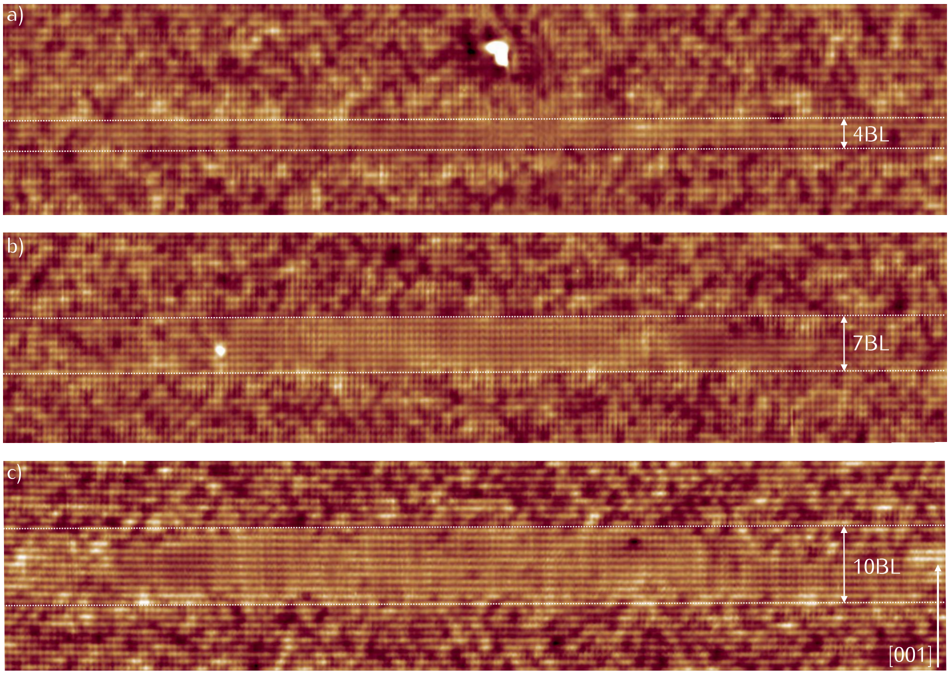

Figure 5.18: 15 nm×68 nm filled states topography images of DE-QDs grown with the flushing procedure. a) 2 nm AlGaAs partial capping. b) 4 nm AlGaAs partial capping. c) 4 nm AlGaAs partial capping + 2 nm GaAs QW.

AlGaAs. This can be explained by the known difference in the initial diffusion length of Ga atoms on GaAs and a AlGaAs (001) surfaces. Here again, the key role of Ga diffusion on determining the QD morphology is highlighted.

Unlike the bottom interface, the top interface of all QDs are found be be very abrupt. The GaAs/AlGaAs transition occurs within one BL. Furthermore, no Ga depleted regions are found above the flushed QDs. The striking sharpness of the top interface is explained by the successful truncation of the QDs with the flushing method. The annealing step under As flux does lead to the complete dissolution of the GaAs crystal remaining exposed after the partial AlGaAs capping and is followed by the desorption of the Ga atoms. Annealing under As flux is well-know as a way to reduce the roughness of the growth front. Here it results in a homogeneously flat surface. During the annealing step, the RHEED pattern changes from spotty to streaky and AFM data shows that the surface roughness is less than 1 nm[141]. As the structure is capped further with AlGaAs, standard 2D growth occurs. The absence of curvature on the surface manifestly explains the absence of the Ga-depleted regions above the QDs. This observation supports the idea that the convex shape of the QD and the difference of mobility of Al and Ga atoms are the factors responsible for the formation of these convex Ga depleted regions.

Interestingly, the position of the annealing step appears clearly in the STM as

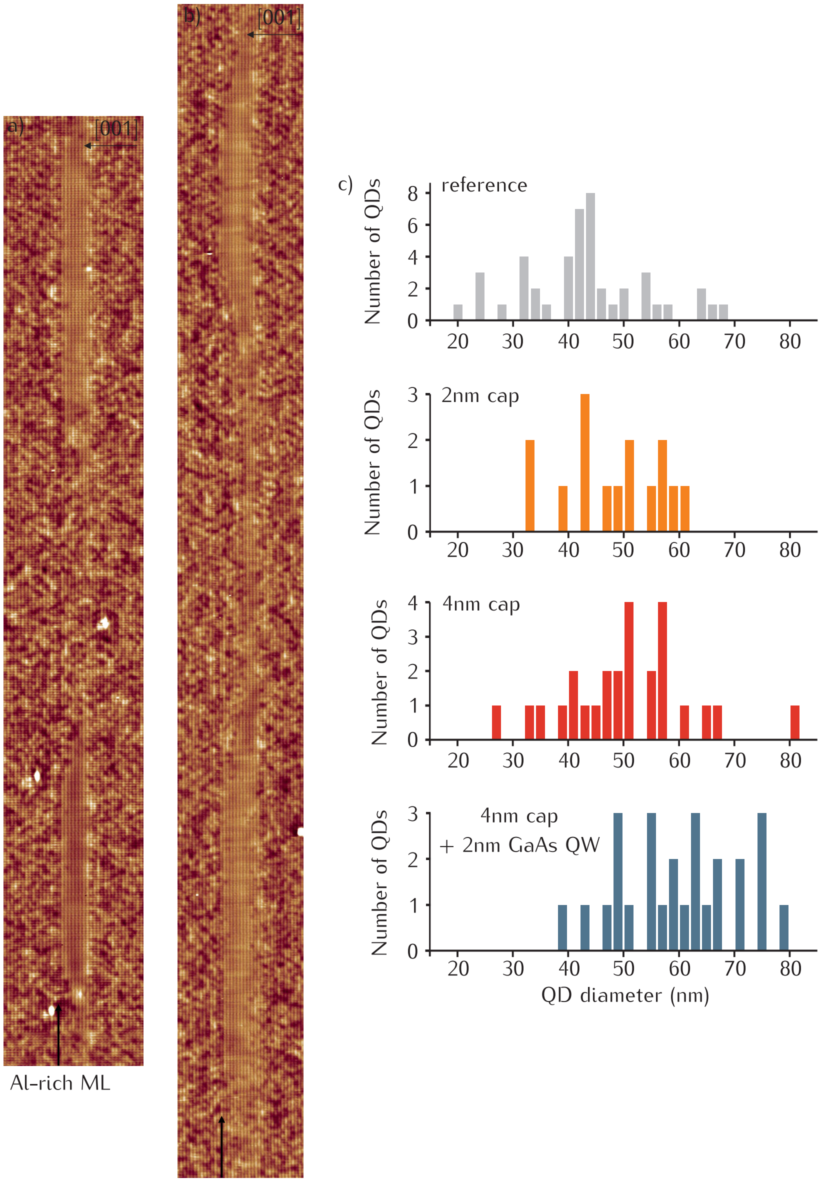

Figure 5.19: a) 22 nm × 150 nm and b) 22 nm × 185 nm filled states topography images of DE-QDs grown with the flushing procedure using a 4 nm thick AlGaAs cap a) on AlGaAs and b) on a 2 nm thick GaAs QW. c) Diameter distribution of the QDs in the four different layers imaged by X-STM.

a dark line better seen in Fig. 5.19a and b. This correspond to an Al-rich bilayer at maximum. Analogous observation has been reported previously for similar annealing conditions of an AlGaAs surface and is explained by the stronger desorption of Ga atoms compared to Al atoms[127]. Comparing both studies reveals that the thickness of the Al-rich layer depend on the temperature of the substrate. Lower temperatures lead to a relative enhancement of the Ga desorption, Al atoms being more strongly bound than Ga atoms. In this case, the presence of an Al-rich bilayer at that position further indicates that the desorption of Ga upon annealing is very efficient. This is in contradiction with a former AFM study showing that, during the flushing procedure, only a partial desorption of the Ga atoms takes place and that thin and elongated GaAs islands are formed[162]. A difference in the heating rate may explain these different observation. The GaAs material originating from the dissolution of the QD top most likely diffuses on the surface before its complete desorption.

The remarkable absence of broadening for the top interface for the flushed quantum dots is a very instructive observation. All QDs were post-annealed at high temperatures, here at 800°C. Therefore this final and necessary rapid annealing step at very high temperatures can not be responsible for the broadening of the interfaces. The search for the origin of the top interface broadening has to be pursued in a different direction. Another difference between the bottom and top QD interfaces is the temperature at which they were grown. While the bottom interface was grown at 170°C, the top interface of the flushed QD was formed at 400°C. This again points towards the important role of Al-Ga interdiffusion for low temperature grown GaAs/AlGaAs interfaces. The reference QDs were also capped at 400°C and presented broad top interfaces. In this case, the QD crystallization process may be responsible for the presence of Al close to the top interface. In particular the presence of Al atoms in the liquid Ga droplet combined with their limited desorption could lead to such broadening. However, the suggested preferential accumulation of Al atoms at the vapor/liquid interface remains to be investigated and clarified.

The quality of QD top interfaces illustrates the efficiency of the flushing technique. To assess the height control achieved with this method, the height of every QD imaged by STM is reported in Fig. 5.20. The distribution of the QD height for each flushed QD layer as well as for the reference QDs is presented.

The QD height distribution for each flushed QD layer is very narrow. This fact is particularly impressive given the fact that X-STM images do not always show QD cleaved through their center at maximal height. Here, the QD height variation is found within 3 bilayers. This minimal dispersion has two origins. First, because of the shallow AlGaAs capping before annealing, the QDs are truncated close to their bases. At that position the QD diameter is relatively large according to the high aspect ratio of the QDs. Consequently the side facets are steep and the QD (001) top facet is wide. The cleavage plane is more likely to go through the top facet. Second, it reflects the very small roughness of the surface after the flushing process. The surface roughness is estimated be within those few monolayers.

More impressive is the relation between the thickness of the partial AlGaAs capping layer and the resulting mean QD height. The inset in Fig. 5.20 shows a one to one relation over the whole range. In others words, the QD height is

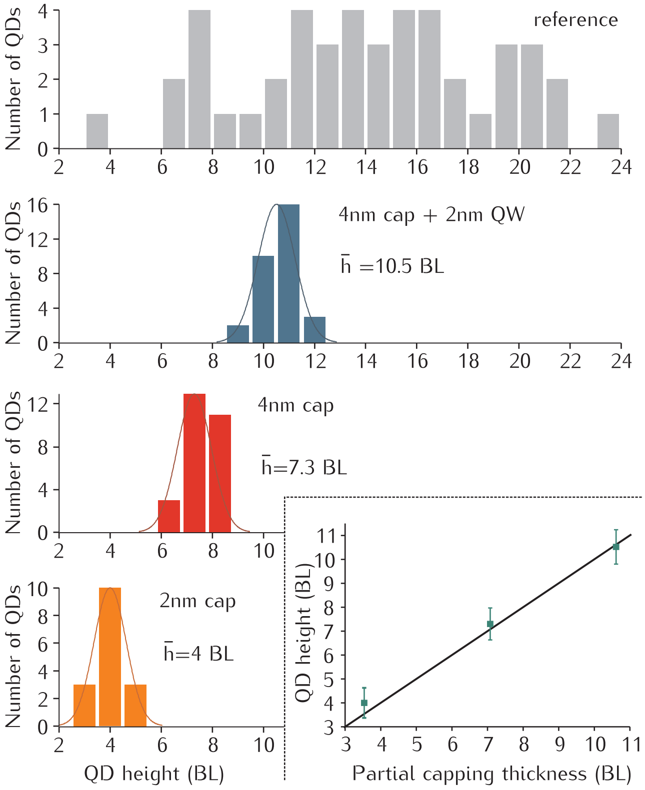

Figure 5.20: Height distribution of the flushed QDs imaged by X-STM. Top to bottom: reference, 2 nm AlGaAs capping, 4 nm AlGaAs capping and 4 nm AlGaAs capping + 2 nm GaAs QW.

the same as the nominal thickness of the partial AlGaAs capping layer. This is shown in the inset of Fig. 5.20, where the QD height is plotted against the partial capping layer thickness. This exact correlation is explained by the absence of wetting layer in the case of DE-QDs and the smoothness of the (001) surface achieved upon annealing. Analogous control of the QD height was achieved with this technique on strained SK-QD systems[160,161]. However the flushing mechanism is expected to be somewhat different in case of unstrained QDs.

From the STM analysis, a mechanism is suggested which is schematically presented in Fig. 5.21. In the case of strain-free QDs, the thin AlGaAs capping layer is expected to grow homogeneously in-between but also on top of the QDs[141]. The presence of a Ga depleted region above QDs capped in a simple way already hinted to the inaccuracy of this hypothesis. Hence, here the assumption is made that during the partial capping of the GaAs QDs, the 2D growth in-between the QDs is favored by the supply of cations through their diffusion along the steep QD side facets. As a result, the QD top is covered by a thin Al-rich AlGaAs layer. This process differs from the partial capping achieved for SK-QDs

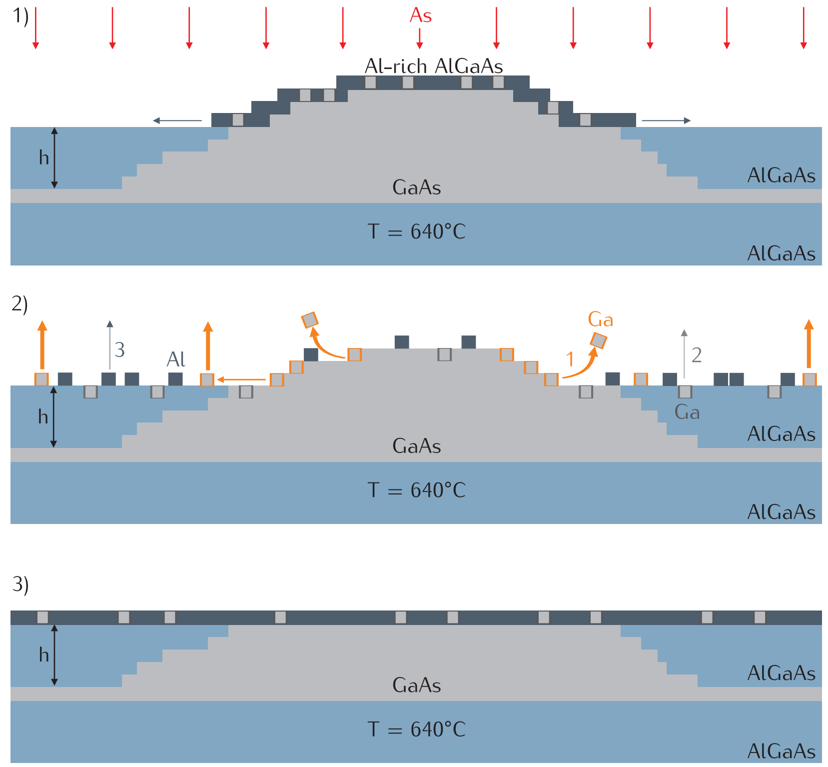

Figure 5.21: Schematic illustration of the suggest mechanism behind the flushing of strain-free GaAs/AlGaAs DE-QDs. A detailed explanation is found in the main text.

by the presence of strain which favors 2D growth in-between the QDs. Then as the temperature is raised under As flux, the atoms at the surfaces start diffusing. Adatoms which are loosely bound will start desorbing. The desorption of Ga atoms is stronger than for Al atoms, leading to an Al-rich surface. As the GaAs QD is uncapped and exposed, Ga atoms will desorb from the QD itself. It is important to stress here that the GaAs DE-QD facets can be described by a stepped surface alternating wide (001) facets and (111)B facets. Consequently, the Ga desorption does not happen homogeneously. Ga atoms at step edges (in orange) have less bonds. The total bond strength of these Ga atoms is lower and they will desorb first. A layer by layer evaporation of atoms supposedly takes place until the surface becomes atomically flat. This evolution leads to a rapid removal of the unprotected GaAs layers at the top of the QD. In comparison, the desorption of Ga from the neighboring AlGaAs surface is much slower and it is suggested that one AlGaAs monolayer at most is fully desorbed. This explains the practically 1:1 relation observed between the partial AlGaAs capping layer thickness and the final QD height. Furthermore, at the end of the annealing step, the surface is rich in Al in agreement with the STM observations. Additional investigations should be made in order to support this qualitative model. On a theoretical side, it is likely that Monte Carlo methods simulating this flushing procedure would bring some insights. In conclusion, the flushing technique is a powerful technique to accurately control of the height of DE-QDs. The fundamental mechanism based on annealing is the same as in SK-QDs. However the necessary partial capping of the QDs depends on diffusion processes and is hence expected to be both material and composition dependent.

chapter 6

X-STM on selenide and telluride II-VI semiconductors

This chapter presents a study at the atomic scale of selenide and telluride semiconductor heterostructures. After a short introduction on their properties, the particularities of X-STM on II-VI semiconductors are discussed. This includes cleavage related effects and the optimization of the experimental conditions. Then, the X-STM study of p-type doping of ZnTe achieved by introducing N atoms is presented. Finally the study of CdSe/ZnTe and CdSe/ZnCdTe multiple quantum wells is presented, focusing on the quality of the interfaces between the selenide and telluride compounds as well as the resulting optoelectronics properties.

II-VI semiconductor materials are usually regarded as exotic materials among solid-state semiconductors compounds. Less abundant, their cost is relatively high and their toxicity is recognized. Nevertheless these wide-bandgap semiconductor compounds are expected to present interesting optoelectronic performances in a wide range of the spectrum. In particular, telluride and selenide based binary and ternary compounds make the emission and absorption possible in a range going from the infrared (CdZnTe), via the visible (CdTe, ZnSe) to the ultraviolet (MnTe). Consequently, they are nowadays used in infrared detectors (CdHgTe), in thin films solar cells (CdTe) or in the fabrication of yellow-green LEDs (ZnSe).

In parallel to these niche applications, a large variety of pioneering fundamental research work in semiconductors physics has been carried out into II-V compounds since the 1980's. Among others, diluted magnetic semiconductors have been extensively studied. Many experiments supplied substantial knowledge to understand bulk ferromagnetism in transition metal doped II-VI semiconductors like ZnTe:Cr[163] or ZnTe:Mn[164]. This effort was followed by the fabrication of electrically active devices controlling magnetic properties like Curie temperature and coercive field. From that point, the interest moved towards smaller systems. Recently the physical properties of a single Mn ion in a CdTe quantum

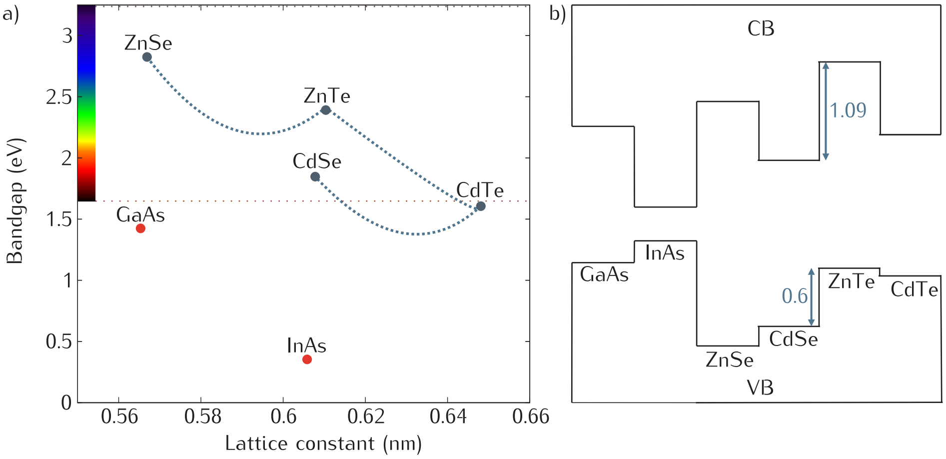

Figure 6.1: a) Band gap energy versus lattice constant for selenide, telluride and arsenide compounds. The blue dashed line indicates schematically the evolution of the bandgap energy with chemical composition. The latter scales linearly with the lattice constant. The red and purple dotted lines represents the limits of the visible light. b) Band alignements and band offsets of cubic selenide, telluride and arsenide compounds.

dot has been the subject of several studies. The spin state of the Mn ion was successfully read out optically and the position of the Mn ion in the system was determined as a critical parameter[25]. Over the years, the fabrication of a wide range of low-dimensional systems by heteroepitaxy allowed for the exploration of phenomena like the emission of single photons in CdSe quantum dots[165,166], Bose Einstein condensation of exciton polariton in CdTe microcavities[167] or the Aharonov-Boehm effect at high temperatures in ZnTe/ZnSe quantum dots[168].

The study presented in this chapter, exclusively focused on selenide and telluride compounds, was motivated by the lack of structural information about these compounds compared to the wide knowledge about their optoelectronic properties. As stressed in the previous chapter, structural properties are decisive when engineering the energy levels of quantum confined systems. Furthermore, precise growth of heterostructures based on selenide and telluride compounds should lead to the creation of devices active in the visible part of the spectrum (Fig. 6.1a.

Selenides and telluride crystals can be grown by Molecular Beam Epitaxy. In heteroepitaxy, they all have a zinc blende cubic structure where each atom has a tetrahedral environment, as described in chapter 2. The sp^3 hybridization of their orbitals results in bonds with a higher ionicity compared to III-V semiconductors because of the stronger difference in electronegativity between cations (group II-elements: Zn, Cd) and anions (group VI-elements: Se, Te). This largely explains their wide bandgaps, which scales with the degree of ionicity of the crystal bonds, as well as their low hardness. Fig. 6.1a shows the bandgap energy of selenide and telluride as function of their lattice constant. The band alignments and band offsets of selenide and telluride compounds are schematically represented in Fig. 6.1b. It shows that the chemical nature of the cation influences the conduction band offset while the chemical nature of the anions influences the valence band offset. For a long time, achieving p and n-type doping of wide bandgap II-VI materials remained difficult, despite considerable efforts to understand and work around substantial compensation effects[169]. Nowadays, n and p-type doping of selenide and telluride is realized routinely. The wide range of lattice constants, bandgaps and band alignments available with those compounds naturally allows the fabrication of a large number of devices with various functionalities. Furthermore, they can conveniently be grown epitaxially on lattice-matched III-V semiconductors substrates like GaAs for ZnSe or InAs for CdSe and ZnTe.

6.1 X-STM on II-VI semiconductors compounds

Few X-STM studies have been carried out on II-VI semiconductors compounds. The smaller II-VI semiconductor community is not the sole reason for the rarity of the reports. II-VI semiconductors compounds happen to be more difficult to prepare for X-STM experiments. For one, they are more brittle than III-V semiconductors which make them more difficult to handle once the sample is thinned down. This difficulty was overcome by growing the II-VI semiconductor heterostructures on III-V semiconductor substrates, like GaAs or InAs. The costs are thereby also reduced, which is a significant point considering the destructive and material consuming character of X-STM. Unfortunately the quality of the cleavage remained poor and the yield very low (5-10%). In most cases the cleaved surface is atomically flat on the substrate while the II-VI semiconductor epilayers are not. The slight variation in yield is explained by its disparity from one system to the other.

Cleaving ZnSe on GaAs has proven to be extremely difficult. A unique example of the ZnSe/GaAs interface is shown in Fig. 6.2a. The interface is cleaved atomically flat. The difference in the height profile results from the valence band offset ZnSe and GaAs (VBO= 1.25 eV[170]). GaAs with a smaller bandgap appears brighter. The interface appears to be abrupt within 1-2 ML but the ZnSe crystal shows regular damages in the form of trenches. The epitaxial ZnSe/GaAs interface has been described thoroughly in the literature. It was experimentally shown that the surface termination of GaAs determines the quality of this interface[171] and that dislocations and vacancies are generally formed[172,173]. The presence of point or extended defects at the ZnSe/GaAs interface may explain the difficult cleavage. Growing a large ZnSe buffer layer to reduce the number of defects in the vicinity of the epilayers of interest did not improve the cleavage.

In comparison, cleaving ZnTe on InAs, with a yield of 10%, has given the best conditions for X-STM experiments. Atomically flat cleavage over the ZnTe/InAs interface was achieved as shown in Fig. 6.2b. The difference in the height profile results from the difference in valence band offset between ZnTe and InAs (VBO= 0.26 eV[174]). InAs with a smaller bandgap appears brighter. The interface is not as sharp as the ZnSe/GaAs interface. Fluctuations up to 6 ML are observed but no structural defects are seen. The good quality of the ZnTe/InAs interface

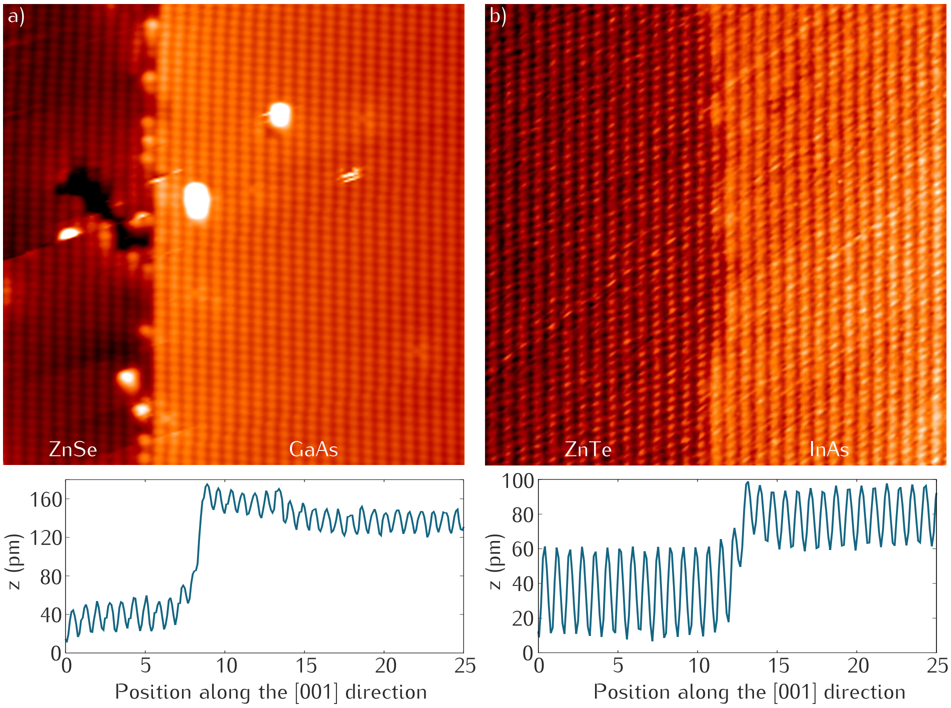

Figure 6.2: a) 25 nm×25 nm filled states images of a a) ZnSe/GaAs interface b) ZnTe/InAs interfaces and the corresponding height profiles. GaAs and InAs have smaller bandgap and appear brighter.

was reported elsewhere along with the suggestion of GaSb as an alternative substrate[175].

This small success for ZnTe on InAs has been the results of specific sample design and numerous attempts which could unfortunately not be translated to others systems. One of the key points has been to carefully choose the thickness of the ZnTe buffer layer. While a thin layer may lead to poor crystal quality, a thicker layer may reduce the conductivity of the epilayers, another crucial point in X-STM experiments. On the contrary, the thickness of the capping layer did not appear to influence the quality of the cleavage. Like for III-V semiconductors, the presence of strain and defects influences strongly the quality of the cleavage.

The lower conductivity of II-VI semiconductors at low temperatures restricted their investigations at room temperature. Good tunneling conditions on these wide band gap semiconductors require on average higher applied voltages (3 V to 5 V). Such voltages compromise however the stability of the W tip which then releases regularly clusters of atoms, contaminating the surface. Lower voltages result in intermittent contact between tip and surface, pulling out atoms and damaging irreversibly the surface as reported earlier[176].

Missing rows of atoms are another distinctive feature of cleaved II-VI semiconductor surfaces. Such extended defects, created upon cleavage, were found on

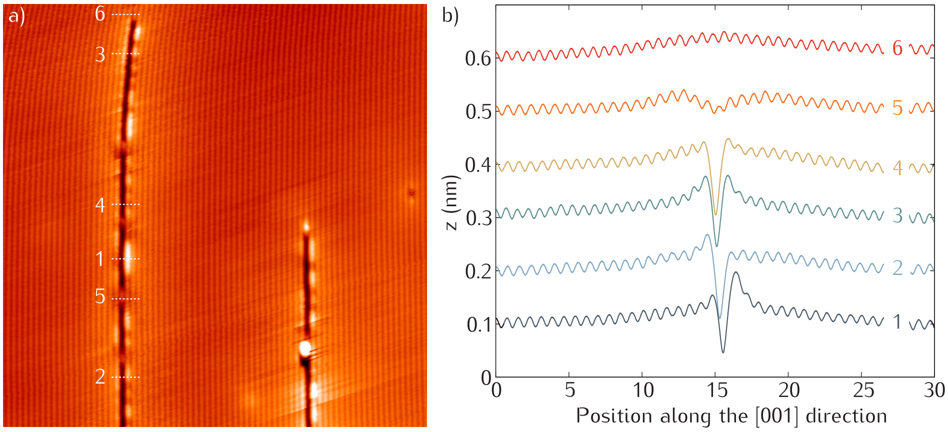

Figure 6.3: a) 45 nm × 45 nm filled states image of the (110) ZnTe surface. b) Height profiles taken along the [001] direction across one of the row at different positions indicated in a).

ZnSe, CdSe and ZnTe (110) surfaces. Two examples are shown in the filled states topography image of the (110) ZnTe surface in Fig. 6.3a. Missing rows of atoms are found to follow straight lines along either the [110] and $[1\bar{1}0]$ crystal directions depending on the cleavage plane. This effect is extremely rare on cleaved III-V semiconductors surfaces. On the contrary, ZnTe, CdSe, ZnSe and CdZnTe cleaved surfaces are nearly always affected. Among selenide and telluride, the number of missing rows is material dependent. The origin of those defects is not clear. The higher ionicity and lower hardness of II-VI semiconductors may be important factors promoting the creation of such defects. The local electronic contrast around the defect is not constant. Such local variations are better seen in the height profiles in Fig. 6.3b taken at different positions across a unique row of missing atoms. This points towards the presence of different bond configurations and relaxation, which locally modify the LDOS. The exact nature of the missing component is however difficult to determine solely from the the STM height profiles. In a recent study, the electronic contributions associated with different vacancy states in ZnTe has been modeled and compared to experimental STM images[177]. According to this study, Zn only, Te only as well as ZnTe binary vacancies are created.

6.2 N doping of ZnTe

The first investigation of II-VI semiconductor structure presented here is the study of ZnTe p-type doping with nitrogen atoms. In ZnTe, N substitutes for Te and acts as a shallow acceptor with a binding energy of 53 meV[178]. The sample was grown by Hervé Boukari at the Néel Institute in Grenoble. A sample was grown containing four 30 nm thick N-doped ZnTe layers separated from another by 70 nm of intrinsic ZnTe. The intended doping level in all layers was 1×10^{19} cm^{-3}. Each layer was grown at a different temperatures; T_1= 300°C, T_2= 320°C, T_3= 340°C and T_4= 360°C. The epilayers of interest were grown on a Zn-doped

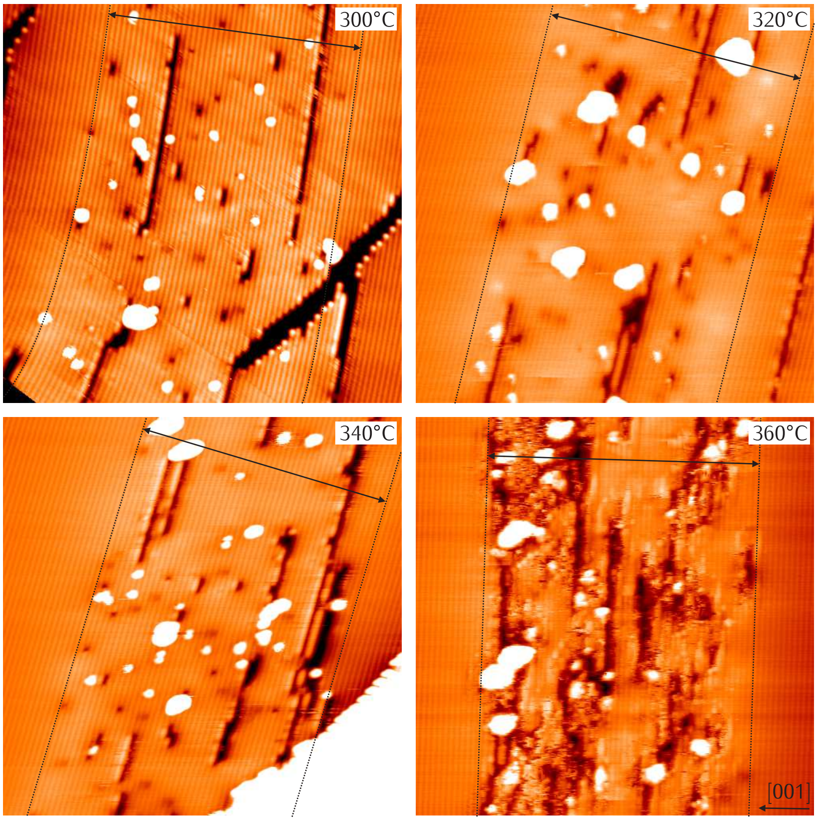

Figure 6.4: 45 nm×45 nm filled states images of four N-doped ZnTe layers grown at different temperatures. The doped layers are 29 nm thick. Segregation and diffusion of dopants are no observed.

InAs substrate and 70 nm thick ZnTe buffer layer and capped by a 500 nm thick ZnTe layer. N-doping is achieved by using a N dc glow plasma source[179]. With this method, N concentrations between 1×10^{18} cm^{-3} and 5×10^{20} cm^{-3} are obtained with a high doping efficiency. The main goal of this study was to investigate the segregation and the diffusion of N dopants in ZnTe as a function of the growth temperature. An earlier study of N-δ-doped ZnTe layers grown at 300° showed that N dopants were both segregating and diffusing over severals nms[176]. The origin of this redistribution was not explained.

Fig. 6.4 shows filled states topography images taken on the four N-doped ZnTe layers grown at different temperatures. The observations are similar for all growth temperatures. The doped layers are extremely affected by the presence of structural defects.

The main defect observed is the presence of the missing rows of atoms along the [110] direction, which are created upon cleaving. The high density of these defects in the N-doped layers compared to the undoped spacer layers is particularly striking. In the spacer layers, few rows of missing atoms are found and

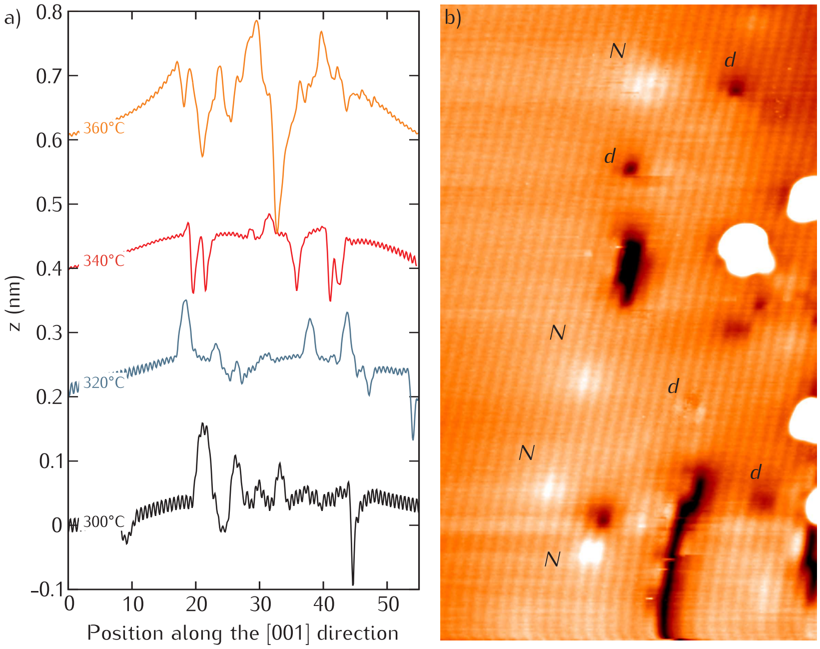

Figure 6.5: a) STM height profile across the four ZnTe:N layers grown at different temperatures. b) 18 nm×30 nm filled states images of N acceptors in ZnTe. N acceptors are ionized and appear as bright and isotropic electronic features.

they propagate over distances of several tens of hundreds of nanometers. In the doped layers, the large majority of these defects are found to be only a few nanometers long. The starting and ending points of these defects lines appear to often coincide with the presence of clusters of atoms on the cleaved surface. It is reasonable to think that theis accumulation of material may be made of Zn and Te pulled out of the surface during cleavage. To explain the statistical difference between doped and undoped regions, it is suggested that the presence of N atoms or other defects promotes the creation of missing rows of atoms. In the case of N in ZnTe, the Zn-N bond (2.16 Å) is smaller than the Zn-Te bond (2.62 Å) and lead to a local compressive strain and a significant change in the lattice parameter[180]. The incorporation of N increase gives rise to local distortions which can lead to extended defects. Point defects were found in the N-doped ZnTe layers. The very localized dark contrasts, labeled as *d* in Fig. 6.5, are attributed to vacancies. A stronger contrast is found for those in the surface layer which may have been created upon cleavage. However, weaker contrasts indicating sub-surface defects created during epitaxy are found with a concentration around 1×10^{19} cm^{-3}. A similar mechanism is suggested to be involved in starting the missing rows, where impurities and point defects can induce local changes in bond configuration which facilitate the detachment of Zn and Te atoms.

The STM height profiles for the four layers, plotted in Fig. 6.5a, do not show the inward relaxation of the cleaved N-doped ZnTe surface expected due to the high concentration of N atoms reducing the average lattice constant. This is due to the strong electronic contribution to the contrast. All the images were taken at -2.5 V and 35 pA. For these tunneling conditions, the N acceptors are in their ionized state and give rise to bright and isotropic contrasts labeled as *N* in Fig. 6.5b. This contrast is induced by the presence of a Coulomb field around the negatively charged N atoms. The LDOS is higher in the N-doped regions compared to the intrinsic regions. Furthermore, the high density of structural defects changes the strain field at the cleaved surface as well as the local electronic potential. Consequently, local changes in lattice constant can not be directly attributed to the presence of N atoms.

N acceptors give rise to delocalized contrasts. Their high concentration results in a bright background and single N impurities are not always resolved. Therefore, they are not a reliable way to determine the exact width of the doped layer. For these reasons, and because of the strong relation between their presence and N-doping was established, the position of the structural defects was used to determine the boundaries of the doped layers (black dotted lines in Fig. 6.4). With this method, all four layers were found to be 47 or 48 BL wide, corresponding to 29 nm. This number is in excellent agreement with the nominal value of 30 nm. Electronic contrasts which could be attributed to N acceptors were not found outside of the intentionally doped layers. This indicates the complete absence of segregation and diffusion of N atoms incorporated in ZnTe in a temperature range of 300°C to 360°C. This conclusion diverges from the one in a previous X-STM study on N-δ-doped ZnTe layers grown at lower temperature[176]. Additionally, the creation of a large number of point defects along with the incorporation of N in ZnTe was revealed, which will strongly affect the electrical and transport properties of the doped ZnTe crystal.

6.3 II-VI semiconductor multiple quantum well structures

The structural properties of multiple CdSe and ZnTe quantum well heterostructures (MQW) were investigated by X-STM and an attempt was made at finding a link with their growth conditions and optical properties. CdSe is a semiconductor compound growing naturally in a wurtzite structure. However, in 1989, Samarth et al. demonstrated that zinc-blende CdSe was obtained by heteroepitaxy on GaAs (001)[181]. Subsequently, the growth of cubic CdSe on different substrates, such as Si[182], InAs[183], or ZnTe was reported. Particularly interesting is the growth of cubic CdSe on ZnTe which gives an almost lattice-matched system[184,185]. The motivation behind the growth of ZnTe and zinc-blende CdSe quantum wells (QW) or superlattices (SL) is the possibility to study in detail an almost strain-free system with type-II band alignment[186]. The type-II band alignment band between the two materials results in the spatial separation of the carriers[186]. Such characteristic is interesting for possible applications in photovoltaics. The electrons are mostly confined in the CdSe, while the holes resides in the ZnTe, leading to a slower radiative combination of the carriers. Engineering these type-II structures also provides access to wavelength regions otherwise not be available with a single material. Short period CdSe/ZnTe superlattices are expected to absorb in the visible between 550 and 700 nm. In order to obtain such specific functionalities, a controlled and precise growth of the semiconductor nanostructures is required. At the nanoscale, phenomena like segregation or intermixing can take place, which deteriorate the intrinsic properties of nominal structures. Epitaxial techniques, like MBE, allow for a high control over the growth and should prevent the development of these unwanted phenomena.

Among others, it was shown in photo-luminescence experiments that optical properties depend strongly on the growth stoichiometry between Cd and Se. Structures with CdSe layers grown in a Se-rich environment show the desired optical emission. On the contrary a Cd-rich growth leads to lower optical properties due to the clear creation of a defect band. In the study presented here, the MBE growth conditions necessary to obtain abrupt interfaces between binary compounds without common anion or cation were investigated by means of X-STM.

6.3.1 Growth and RHEED observations

The samples were grown by Régis André and Lionel Gérard at the Néel Institute in Grenoble. The different samples were grown by MBE in a Riber 32P MBE machine, containing elemental cells of Cd, Se, Mn, Zn and Te. During the growth, the background pressure was around 1×10^{-10} Torr. *In situ* feedback on the growth was obtained with Reflection High Energy Electron Diffraction (RHEED) analysis. To obtain the best optical properties, the samples were grown on ZnTe (001) substrates except for the dedicated STM samples grown on InAs (001). ZnTe substrates were chemically prepared. A solvent bath was used to clean the surface followed by a short bromine and methanol attack to remove the oxide layer. To avoid oxidation, the samples were transferred to the nitrogen glove box in a solvent bath. InAs substrates were deoxidized *in-situ* under As flux between 400° C and 500° C, monitoring the surface state with RHEED. In both cases, a ZnTe buffer layer was grown at 340 °C for higher material quality and reproducible results. Stable growth conditions for CdSe are found for substrate temperatures between 280° C and 340° C. Determining the optimal flux ratio of the elemental Cd and Se cells is not trivial as both elements have a relatively low sublimation temperature. For this reason, they are generally used in excess for the growth of (001) ZnSe and CdTe[187].

The progress of the epitaxy at the MQW interfaces as monitored by RHEED in real-time. During the growth, going from one element in excess to the other changes the surface reconstruction resulting in specific RHEED patterns. In the case of CdSe, a growth in excess of Se gives a (2×1) reconstruction, typical for Se stabilized surfaces[171]. When grown in excess of Cd, $c(2 \times 2)$ and (2×1) reconstructions are visible. This allows for a good control of the growth conditions. Additionally, the RHEED intensity reflects the roughness of the growth surface. If the growth takes place on a flat and clean surface, the RHEED intensity oscillates periodically as each monolayer is formed. However these oscillations have shown abnormal dynamics depending on column-II/column-VI element flux ratio. When growing CdSe in Se excess on ZnTe, the RHEED intensity oscillations at

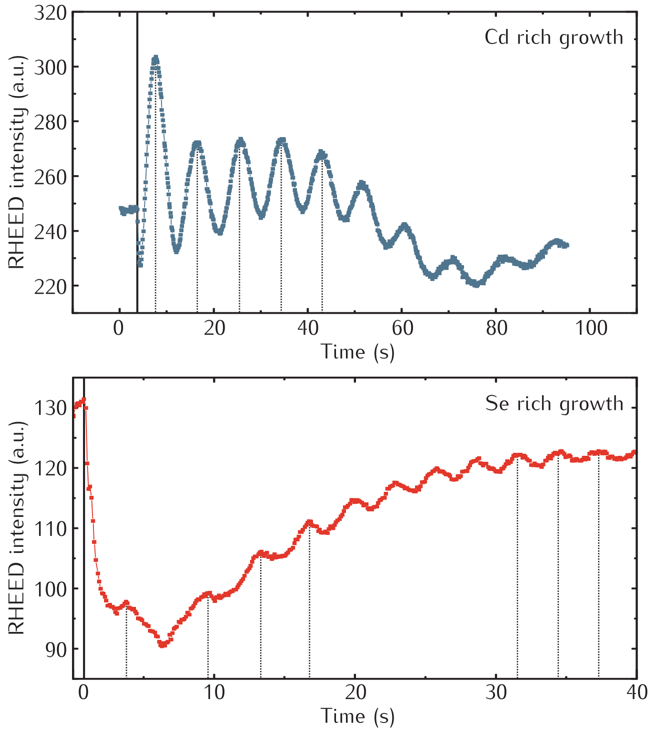

Figure 6.6: RHEED intensity oscillations at the CdSe/ZnTe interface for different growth conditions. Full black lines indicate the CdSe/ZnTe interface. Dotted lines are drawn as guide to the eyes to highlight the periodicity of the oscillations. a) CdSe grown Cd-rich conditions, the RHEED oscillations are periodic. b) CdSe grown Se-rich conditions, the RHEED intensity oscillations periods are not uniform.

the interface behave unexpectedly. The oscillations are not periodic. The period decreases with time before reaching the nominal growth rate (expected from the calibrations), typically after ≈8 periods, as shown in Fig. 6.6. This phenomenon is not symmetrical as it happens exclusively and reproducibly at the CdSe/ZnTe interface. Homo-epitaxial growth of CdSe on CdSe does not show this anomaly either. The effect of an initial burst in the Se and/or Cd flow is excluded because it would give rise to the opposite effect: a faster growth as more matter arrives onto the sample. This RHEED oscillation rate anomaly can be interpreted in different yet concurring ways. On the one hand it can be the result of an acceleration of the growth rate before stabilization at a constant rate. On the other hand, independently from the growth rate, the non-periodicity of the oscillations can represent an irregular roughening of the surface over time.

Either way, this anomaly is tentatively attributed to physical phenomena occurring at the CdSe/ZnTe interface. A possible interpretation would be the presence of an epitaxial mechanism at the interface slowing the growth rate, such as an eventual rearrangement of the atomic plane at the CdSe/ZnTe interface. Up to now, atomic rearrangements have been detected by Raman spectroscopy[188] and have been found energetically favorable by total energy calculations[189]. In both exposed theories however, the phenomenon appeared at the ZnTe/CdSe interface as well. Another possible reason for this to happen is the direct growth of a bilayer. In this case, the first oscillation would correspond to the growth of two monolayers. However, if the first oscillation period seems to be two times longer than the period after stabilization, the gradual nature of the transition seems to rule out this possibility. A alternative explanation would be the presence of segregation, with one of the two constituents of the ZnTe layer being partially incorporated in the first monolayers of the CdSe well leading to the formation of a $CdSe_{1-x}Te_x$ alloy as observed in the ZnSe/ZnTe system[190,191]. The RHEED oscillations analysis provides information about the sequence of events happening during the growth. The presence of an unexpected mechanism when CdSe is grown on ZnTe under excess of Se is very likely. However, its nature cannot be determined without chemical information. For this reason, this study is complemented by X-STM experiments. X-STM which has proven to be a valuable tool to investigate heterostructures, was used to provide information about the chemical composition of the CdSe and ZnTe interface at the atomic scale.

6.3.2 CdSe/ZnTe multiple quantum wells

6.3.2.1 Sample description

The first structure investigated by X-STM is a CdSe/ZnTe multiple quantum wells structure. The deoxidation of the p-doped InAs substrate under an Zn flux was followed by the growth of a ZnTe buffer. The MQW was made of 10 periods consisting of 7 nm CdSe on 7 nm ZnTe. The MQW was capped with 40 nm of CdSe. The growth temperature was 320° C and the CdSe wells were grown in excess of Cd with a Cd:Se ratio of 3.2. In these conditions, the RHEED oscillations at the CdSe/ZnTe interfaces do not show the anomaly mentioned earlier.

6.3.2.2 X-STM analysis

Fig. 6.7a shows a typical filled states topography image of four periods of the CdSe/ZnTe MQW grown in Cd-rich conditions. Filled state images, taken at negative bias voltages, reflect the electronic states of the valence band and indicate the distribution group-VI atoms. The MQW period is found to be 15-16 BL, *i.e.* 9.5 nm. This is thinner than the nominal value of 14 nm. The 1:1 ratio between the thickness of two layers is however respected. Some point and extended defects, *i.e.* missing rows of atoms, are observed with a higher density close the interfaces.

The contrast between the CdSe and the ZnTe layers is strong. As expected for negative voltages, the CdSe wells appear bright while the ZnTe wells appear dark. The contrast is inverted upon switching voltage polarity, as shown in Fig. 6.7b. This inversion of contrast observed between the filled- and empty-states images is attributed to the expected type-II band alignment between CdSe and ZnTe (see Fig. 6.1b). An STM height profile taken on a filled states topography image across a few periods is displayed in Fig. 6.8. The height difference between

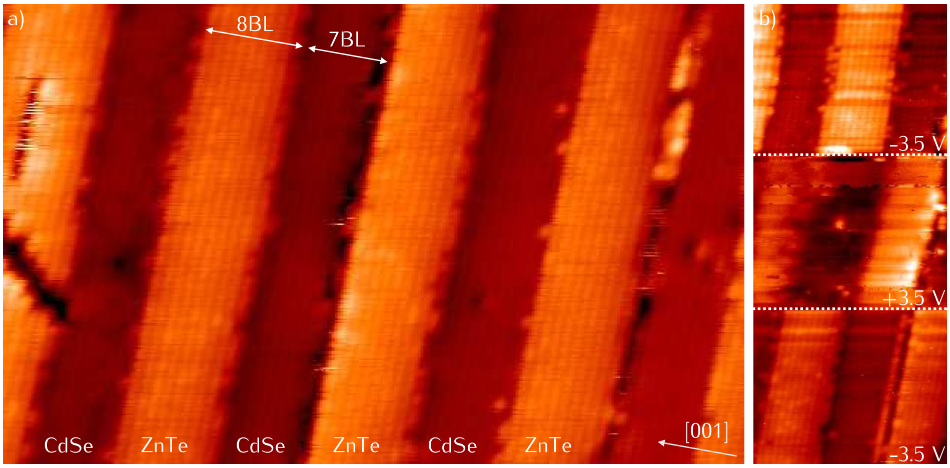

Figure 6.7: 40 nm x 33 nm filled states topography images of 4 periods of the CdSe/ZnTe MQW grown under excess of Cd. The CdSe wells appear dark and ZnTe wells appear bright.

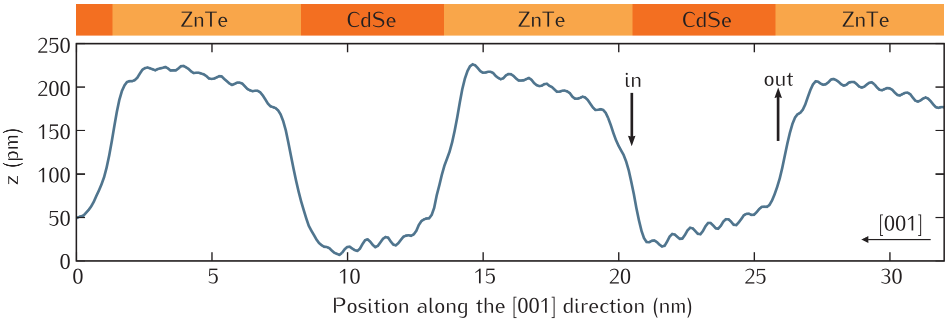

Figure 6.8: STM height profile showing the outward relaxation profile of the cleaved surface over the CdSe/ZnTe MQW averaged over 15 nm. The height variations have mainly an electronic origin which mostly reflects the valence band offset between the CdSe and the ZnTe QWs. Possible explanations for the local and reproducible slope in the profile are the presence of intermixing or different binary compounds at the interfaces.

the materials has mainly an electronic origin which mostly reflects valence band offset between ZnTe and CdSe.

The interfaces in a CdSe/ZnTe heterostructure are expected to be strain-free due to the very small lattice mismatch between these two semiconductor materials. This does not seem to be the case in this particular MQW. In the absence of strain, the STM height profile would exhibit two flat levels reproducing the valence band alignment across the MQW. Here the surface appears to be tilted differently on each type of QW. This observation is reproducible from one layer to the other and the possibility of a measurement artifact is ruled out.

Two phenomena can account for these slanted profiles. The first phenomenon

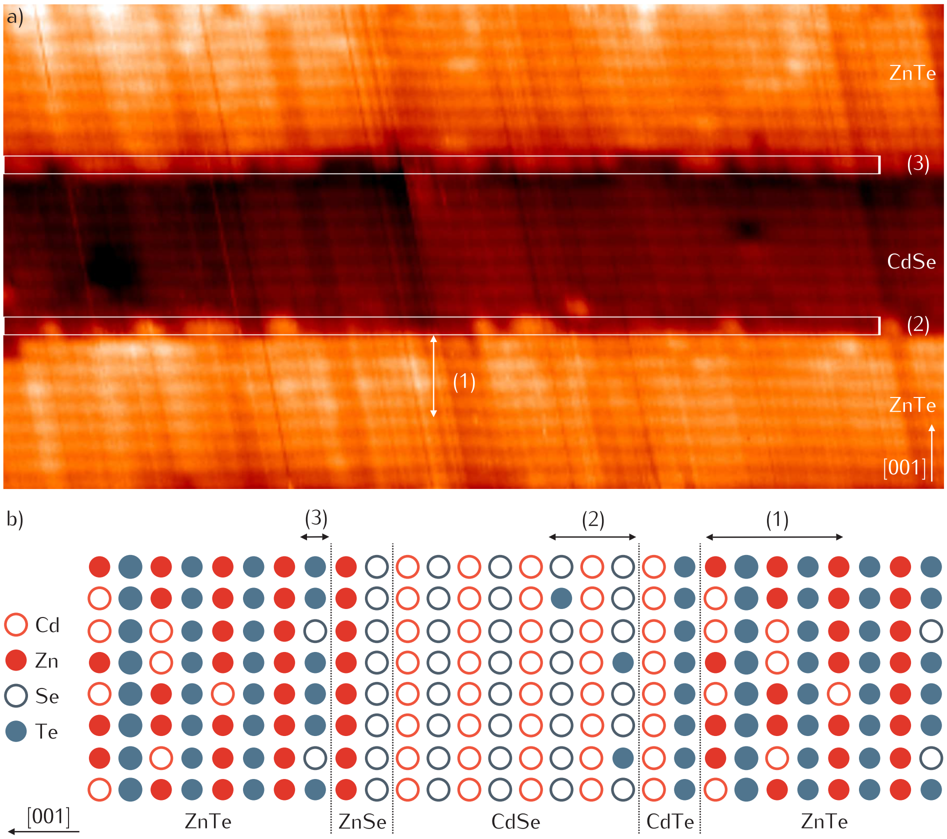

Figure 6.9: a) 30 nm x 15 nm filled states topography images of 3 periods of the CdSe/ZnTe SL grown under excess of Cd. b) Schematic illustration of the interfaces in the CdSe/ZnTe MQW as extracted form the STM data. Physical phenomena suggested to take place are numbered and indicated on the STM above. 1) Cd back-diffusion in ZnTe, 2) Te segregation in CdSe and 3) Se segregation in ZnTe.

proposed arises from the absence of common anion and cations at the CdSe/ZnTe interfaces. Thus, the bonds at the interfaces can be seen as constituting a monolayer of a different binary compound. In this system, either Cd-Te or Zn-Se bonds form at the interfaces, respectively corresponding to a monolayer of CdTe or ZnSe. These two semiconductors are not lattice matched with CdSe and ZnTe (see Fig. 6.1a). The presence of shorter or longer bonds will generate local strain at the interfaces. Consequently, upon cleavage the surface will relax through the deformation of the surface and this topographic change will add up to the electronic contrast of the STM. The sign of the relaxation and its contribution depends on the nature of the strain. A compressive strain will cause an inward relaxation and a tensile strain an outward relaxation. Here, short Zn-Se bonds lead to a compressive strain while long Cd-Te bonds lead to tensile strain. The nature of the surface relaxation at the interfaces is indicated by arrows in Fig. 6.8.

The ZnTe/CdSe interfaces relax inwards, while CdSe/ZnTe interfaces relax outwards. This suggests that Zn-Se bonds are present at ZnTe/CdSe interfaces, whereas Cd-Te bonds form at the CdSe/ZnTe interfaces. This configuration is schematically illustrated in Fig. 6.9b. It is important to note that X-STM can only resolve a single monolayer with difficulty. Therefore the electronic contrast from a possible ZnSe or CdTe monolayer does not appear clearly in the filled states topography images. The second possible explanation for the slopes in the STM profile is based on similar arguments. Intermixing would in the same way induces strain in the crystal. Both segregation and diffusion phenomena can give rise to intermixing. The strong electronic contrast between CdSe and ZnTe makes it difficult to resolve the presence of a low intermixing level. The layers appear as almost pure binary compounds.

A larger magnification, as in Fig 6.9a, allows for a more detailed investigations. Three observations are made which are numbered in the filled states topography image and the schematic representation of the heterostructure. (1) A number of brighter atoms appear inside the ZnTe wells, which are identified as Cd atoms. It also appears to be a gradient in Cd starting from the CdSe/ZnTe interface. At first sight, the Cd seems to be back diffusing from that interface. Determining a precise concentration profile is not trivial. Here, the strong electronic contrast prevents the comparison of the experimental relaxation profile of the cleaved surface with the one calculated by the method presented in chapter 2. In comparison, the CdSe well does not show any intermixing. (2) Bright atoms are found in the first CdSe bilayer which are identified as Te atoms considering that the anion sub-lattice is imaged here. (3) The dark and local contrasts at the ZnTe/CdSe interface are interpreted as Se atoms. A strong contrast is found as the anion sub-lattice is imaged in this image. The first ZnTe bilayer has on average a darker contrast which can be the signature of an ZnSe interface and/or a Se segregation limited to the first bilayer. Overall, the interfaces in this CdSe/ZnTe MQW are well-defined and sharp within one bilayer.

6.3.2.3 Strain relaxation calculations

To explore the relevance of the different phenomena suggested above, the relaxation of the cleaved surface expected for each scenario was modeled by means of the finite element based method described in chapter 2. Figure 6.10 allows to compare the relaxations calculated for each scenario with the experimental profile (black line). The experimental profile was obtained from filled states image taken at -3.5 V. At this voltage and because of the large bandgap, the electronic contribution to the apparent height is still substantial. This electronic contribution is not accounted for in the calculated profiles. Beside the model based on nominal structure, five 2D models of the MQW have been developed. In blue: the results of models including the back-diffusion of Cd in ZnTe as seen in the filled state image shown in Fig. 6.9. In red: the results of models including the segregation of Te in CdSe, a phenomenon expected to take place at the CdSe/ZnTe interface. In orange: the result of a model including 1 ML ZnSe at the ZnTe/CdSe interface and 1 Ml of CdTe at the CdSe/ZnTe interface. In dotted lines: the results of model including those binary compounds at the interfaces.

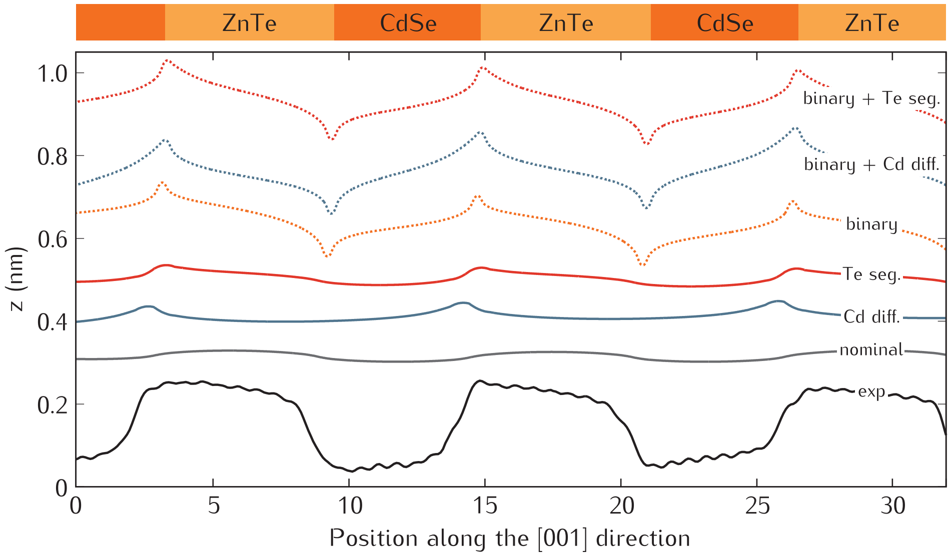

Figure 6.10: Experimental and calculated outward relaxation profiles of the CdSe/ZnTe MQW. Profiles have been calculated for structures without (full lines) and with (dotted lines) binary monolayers at the interfaces. Additional phenomena have been taken into account: Te segregation in CdSe (blue), Cd back-diffusion in ZnTe (red).

The concentration of Te segregating and the concentration of Cd back-diffusing have been modeled by exponential function. This description is in agreement with concentration profile of dopants like Mn in GaAs[78] or isolectronic atoms like In in GaAs[44]. The exponential decay of those concentrations is described by the function $x = x_0\,[1-\kappa]^z$, with x the fraction of Te or Cd in a given monolayer, κ the fraction of Te or Cd, respectively segregating and back-diffusing to the next monolayer, $z = 0$ the start of the QW and positive z representing the growth direction. Here, x_0 is fixed at 0.5 and κ to 0.5. In others the first monolayers contains 50% of Cd or Te and the concentration decreased by half with every monolayer. By adjusting the initial fraction of Cd or Te x_0 and κ until the calculated outward relaxation profile reproduces the outward relaxation profile measured by X-STM, the concentration profile in the CdSe well can be determined. Here the experimental profile can not be fitted exactly because of the electronic contribution to the apparent height. However the trends, *i.e.* the slopes, can be simulated. The nominal structure (in grey) clearly does not account for the observed surface relaxation. Varying x_0 and κ determining the Te segregation and the Cd back-diffusion only partially reproduces the experimental profile. The trend is correct but the magnitude of the relaxation is to low. Considering Zn-Se and Cd-Te interfaces increases greatly the relaxation of the cleaved surface. This is in better agreement with the experimental profile. Indeed, the height difference is very large and can only be attributed with difficulty to the 0.6 eV valence band offset between CdSe and ZnTe. From these simulations, it appears that the presence of Te segregation and Cd the back-diffusion is likely. From the X-STM analy-

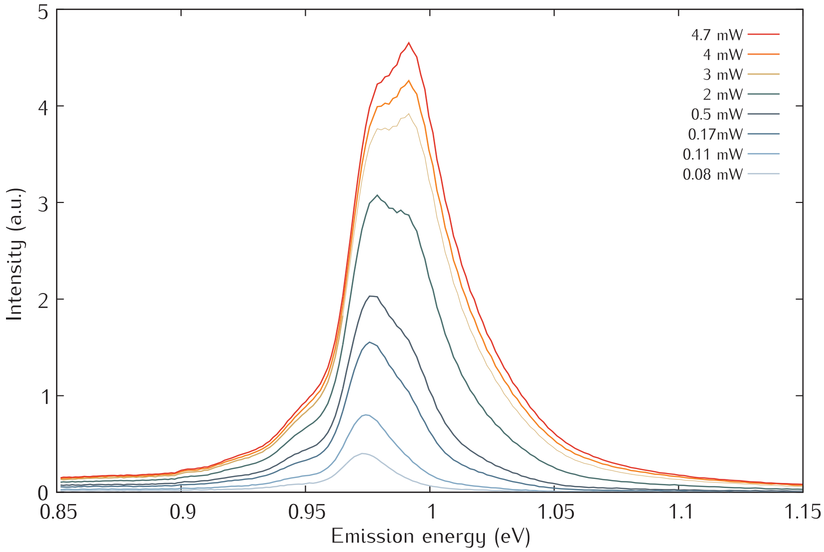

Figure 6.11: Photoluminescence spectra of the CdSe/ZnTe MQW for different excitation powers. The optical emission occurs around 0.97 eV. The emission energy shifts towards higher energies with increasing excitation power.

sis, the hypothesis of having Zn-Se and Cd-Te interfaces can not be completely validated. Furthermore, high resolution X-ray diffraction experiments on similar CdSe/ZnTe MQWs support the idea of a ZnSe monolayer forming at the one of the interfaces. Transmission electron microscopy characterization should soon give new insights, refining the ideas presented here.

6.3.2.4 Optical properties

This CdSe/ZnTe MQW was characterized by means of photoluminescence (PL) experiments. In Fig. 6.11, the photoluminescence spectra of this heterostructure as a function of the excitation power is shown. Each peak can be fitted with a simple Lorentzian curve, despite the visible double component of unknown origin. The emission occurs around 0.97 eV, that is well below the bandgap of CdSe and ZnTe. This is the result of the type-II band alignment across this MQW. Electrons are confined in the CdSe wells, whereas holes are confined in the ZnTe wells. Mourad *et al.*, recently reported a VBO of 0.75 eV between CdSe and ZnTe. Consequently, the carrier recombination at this interface should occur at 1.0 eV. (see Fig. 6.1b). The lower energy measured here is attributed to the bending of the bands in this CdSe/ZnTe MQW. This MQW structure allows for a bending of the bands over a large scale in order to align the Fermi levels as schematically illustrated in the inset of Fig. 6.12. The emission energy shifts towards higher energies with increasing excitation power. This blue shift is explained by a combination of band bending effect and band filling at each interface. The spatial separation of electrons and holes induces an electric field at the interfaces *i.e.*

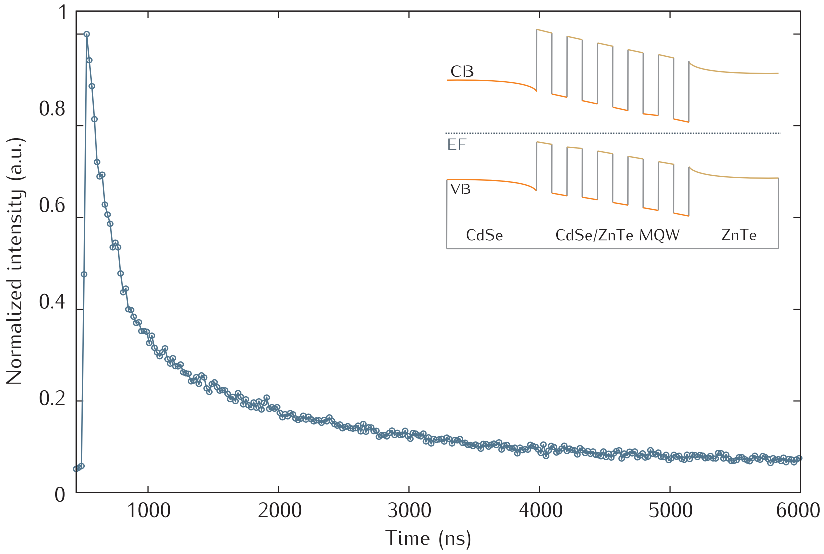

Figure 6.12: Time dependence of the photoluminescence of the CdSe/ZnTe MQW. The decay time, in the order of microsecond, is explained by the limited overlap between electron and holes wave functions for this relatively large period of 9.5 nm. Inset: schematics of the suggested bending of the semiconductor bands across the CdSe/ZnTe MQW.

a band bending. As the power is increased electrons and holes are confined in triangular potential wells close to the interface. The carrier population found at higher energy levels results in the blue shift of the emitted PL. A more complete study, not presented here, shows that this shift in energy seems to be proportional to the power $P^{2/9}$ rather than $P^{1/3}$. This points out towards the recombination of free carriers instead of excitons (no Coulomb interaction involved)[186].

The time dependence of the PL is shown in Fig. 6.12. The decay in the MQW structure is clearly hyperbolic and can be fitted with hyperbola curve to the power of 2 or 3/2. Additionally, an exponential component is added to obtain a better fit the experimental curve, which is attributed to presence of defects. From this analysis, it is difficult to conclude about the excitonic character of the recombination. The decay time of the PL emission in the order of microseconds. As expected, this recombination time is orders of magnitude higher than for heterostructures with a type-I band alignment. This is again explained by the different spatial location of electrons and holes. The relatively large period of the MQW (9.5 nm) results in a lower overlap between electron and holes wave function.

To summarize, the CdSe/ZnTe MQW imaged by X-STM is very close from its nominal description. The QW thickness ratio is correct. The interfaces are sharp within one bilayer. Some strain is present at the interfaces which may be due to well-defined Cd-Te and Zn-Se bonds at the interfaces or a low degree of intermixing. The CdSe wells are pure, while the ZnTe wells show some Cd intermixing. Nonetheless, evidences of type II band alignment are found in the

STM analysis and photoluminescence characterization. Unfortunately, structural defects are likely to be present considering the quality of the cleavage. From this study, the Cd-rich growth CdSe/ZnTe superlattices, with periods of a few monolayers, is promising. Sharp interfaces should be achieved and the optical emission energy controlled. Furthermore, for shorter periods, the structure can be considered as an ordered alloy and effects due to the interfaces is supposedly negligible.

6.3.3 CdSe/ZnCdTe multiple quantum wells

6.3.3.1 Sample description

The second structure investigated by X-STM is a CdSe/ZnCdTe multiple quantum well structure. The deoxidation of the p-doped InAs substrate under an As flux was followed by the growth of a ZnTe buffer. The MQW was made of 14 periods consisting of 7 nm CdSe on 7 nm ZnCdTe. The growth temperature was 340° C and the CdSe wells were grown in excess of Se with a Cd:Se ratio lower than 0.5. During the growth of ZnTe, a $c(2 \times 2)$ surface reconstruction is visible. During the growth of CdSe, a $c(2 \times 1)$ surface reconstruction is visible. In these conditions, the RHEED oscillations at the CdSe/ZnTe show the anomaly mentioned earlier.

6.3.3.2 X-STM analysis

Fig. 6.13a shows a filled states topography image, taken at -3.5 V, of four periods of the CdSe/ZnCdTe MQW grown in Se rich conditions. Filled state images, taken at negative bias voltages, reflect the electronic states of the valence band and indicate the distribution of group-VI atoms. As expected, the CdSe wells appear dark and the ZnCdTe wells bright reflecting the valence band alignment between the two materials. The ZnCdTe wells are 5 BL (3 nm) thick that is clearly thinner than the 14 BL (8.5 nm) wide CdSe wells. A physical reason for the discrepancy between nominal and measured thicknesses is excluded and attributed instead to an inaccurate calibration of the growth rates. The ZnCdTe is a ternary alloy and exhibits an inhomogeneous contrast. A number of brighter atoms appear inside the CdSe wells, which are identified as Te atoms. They appear to be distributed in a gradient starting at the CdSe/ZnCdTe interface. Consequently, this interface is not sharp. On the contrary, the ZnCdTe/CdSe interface is more abrupt and Te back-diffusion in CdSe does not seem to take place.

Fig. 6.13 shows an empty states topography image, taken at +3.0 V, of four periods of the same CdSe/ZnCdTe MQW at a different position. The segregation of Te in CdSe is also visible in the empty states images. Two types of local electronic contrasts are attributed to Te atoms and labeled in Fig. 6.13. Brighter atoms (1) are located in the surface layer whereas atoms labeled (2) are located in the first layer below the surface. The most striking difference between this MQW and the CdSe/CdZnTe MQW investigated in the previous section is the absence of contrast inversion between filled and empty states images. The presence of Cd in ZnTe is expected to reduce the bandgap of ZnTe. In particular, the conduction band edge should be affected and the conduction band edge lowered. But the type-II band alignment should be preserved for all concentration of Cd. The

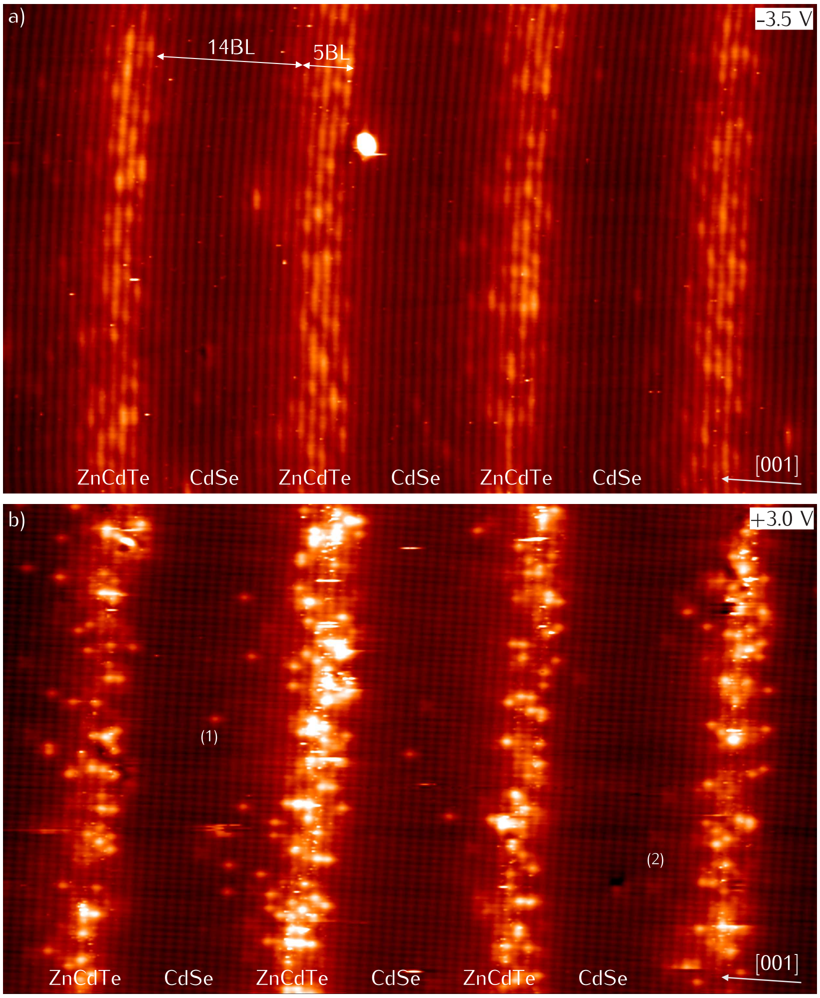

Figure 6.13: 40 nm x 33 nm filled states topography images of 4 periods of the CdSe/ZndTe MQW grown under excess of Se. The binary CdSe wells appear dark and the ternary ZnCdTe wells appear bright. (1) Te atoms in the surface layer, (2) Te atoms in the first layer below the surface.

contrast at positive bias voltage does not reflect the conduction band alignment of the structure. The unexpected observation is attributed to a combination of factors. First Cd atoms are observed as very bright spots because of the local dangling bond. It is worth noting that the Cd atoms present a much brighter contrast in the empty state image when the cation sub-lattice is imaged. The lattice is atomically resolved but the small difference in contrast between Cd atoms in the first and second monolayers does not allow to estimate the Cd concentration by simply counting. Second, the presence of Cd in ZnTe results in a number of Cd-Te bonds which are longer than the Zn-Te bonds. The ZnCdTe

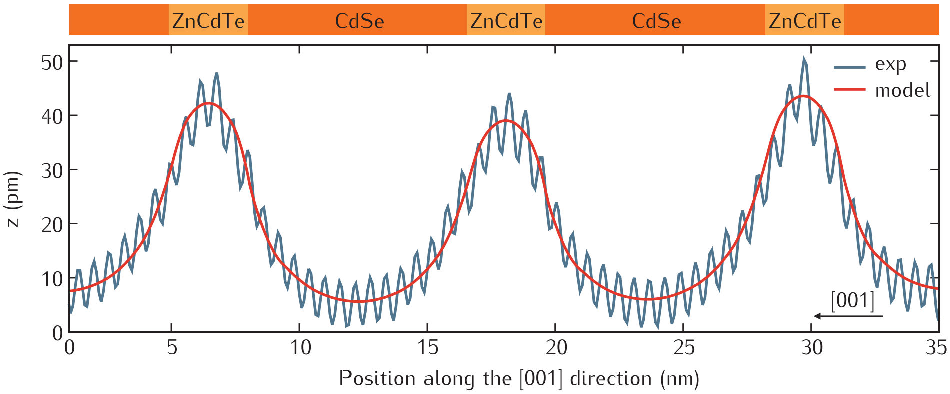

Figure 6.14: STM height profile showing the outward relaxation profile of the cleaved surface across the CdSe/ZnCdTe MQW averaged over 15 nm (blue) The height variations mainly have a topographic origin. The height variation reflects the relaxation of the strained ZnCdTe QWs upon cleavage. The red line is the result of the calculated relaxation profile for a CdSe/ZnCdTe MQW with ≈ 13% Cd in ZnTe and Te segregation in CdSe.

layers are therefore under tensile strain, leading to the outwards relaxation of the cleaved surface shown in Fig. 6.14. To summarize, the combination of the high bias voltage, the strong topographic component to the STM contrast as well as the bright electronic contrast originating from each single Cd atom is responsible for the bright contrast of the ZnCdTe layers. The Cd concentration appeared to be inhomogeneous within one well and to fluctuate greatly from one well to another. This is in agreement with the direct observations of the X-STM images.

6.3.3.3 Strain relaxation calculations

The Cd concentration in the ZnCdTe layers was determined using the finite element calculations used to simulate the outward relaxation of the cleaved surface. The input model consisted in the CdSe/$Zn_{1-x}Cd_xTe$ MQW, with x the fraction of Cd. The well thicknesses were based on the STM analysis. The segregation of Te deduced from the X-STM images was also implemented in the model. As mentioned earlier, such segregation can generally be modeled by an exponentially decaying function[44], described here by the function $y = y_0[1-\kappa]^z$, with y the fraction of Te in a given monolayer, κ the fraction of Te segregating to the next monolayer, $z = 0$ the start of the QW and positive z representing the growth direction. The three parameters, x, y_0 and κ, were adjusted until the calculated outward relaxation profile, matches the outward relaxation profile as measured by X-STM. The result is shown in Fig. 6.14. The red line is the calculated profile and the blue line is the experimental profile. This good match was found for Cd concentrations around 13% in the $Zn_{1-x}Cd_xTe$ layers. κ was set to 0.5, that is 50% of Te going to the next layer, while the initial concentration of Te in CdSe was set around 15%. Including the Te segregation was a key point to reproduce the slight asymmetry of the profile along the growth direction. It is important to stress here that the parameter space was such that both the Cd concentration x and the initial concentration of Te y_0 could be tuned in small windows of approximately 2% while keeping a reasonable fit. This is explained by the similar CdTe character arising from increasing those concentrations. Consequently, they mainly determine the magnitude of outward relaxation. From this study, the possibility of growing CdSe/ZnTe superlattices, with periods of a few monolayers, in Se-rich conditions is called into question. Without sharp interfaces, the optical emission energy of the structure is uncertain.

6.3.4 Conclusions

The X-STM study of these two MQWs brought some insight in the growth of the selenide/telluride heterostructures. The main focus has been the type and the quality of the interfaces without common cations and anions. From these two studies, it clearly appears that the growth conditions of CdSe determine the quality of the interfaces. The interfaces of the CdSe/ZnTe MQW with CdSe grown under excess of Cd appeared to be sharp and well-defined within one bilayer. The back-diffusion of Cd in ZnTe is clearly observed. Furthermore, the relaxation of the cleaved surface supports the presence of Zn-Se or Cd-Te bonds respectively at the ZnTe/CdSe and CdSe/ZnTe interfaces. On the contrary, the CdSe/ZnCdTe interfaces grown under excess of Se are not abrupt. Te atoms are found to segregate from this interface. The segregation of Te might explain the non-periodic RHEED oscillations observed at Se/Te interfaces grown under similar conditions. Unfortunately, the mechanisms behind the creation of structural defects in Cd-rich growth condition and the segregation of Te in Se-rich growth conditions have not been determined. Consequently, the growth conditions for CdSe should be chosen according to the desired functionality of the heterostructure. If, like for short period superlattices, sharp interfaces are required, Cd-rich growth is much more suited. Whereas if a low defect density is necessary a Se-rich growth is expected to perform better. Another approach to preserve both the layer quality and the interface abruptness would be to grow CdSe in Se-rich conditions and add Atomic Layer Epitaxy stages at the interfaces. With this method, each monolayer is grown in a controlled manner and any segregation phenomena should be prevented. CdSe/ZnTe superlattices grown recently with this method appear to be very promising.

References

[1] T. H. Mainan. Stimulated Optical Radiation in Ruby. *Nature*, 187:493–494, 1960.

[2] H. Nelson. Epitaxial growth from the liquid state and its application to the fabrication of tunnel and laser diodes. *RCA Review*, 24:603, 1963.

[3] J. P. van der Ziel, R. Dingle, R. C. Miller, W. Wiegmann, and W. A. Nordland. Laser oscillation from quantum states in very thin GaAs-Al0.2Ga0.8As multilayer structures. *Applied Physics Letters*, 26(8):463, 1975.

[4] A. Imamoglu, D. D. Awschalom, G. Burkard, D. P. DiVincenzo, D. Loss, M. Sherwin, and A. Small. Quantum Information Processing Using Quantum Dot Spins and Cavity QED. *Physical Review B*, 83(20), 1999.

[5] J. R. Weber, W. F. Koehl, J. B. Varley, A. Janotti, B. B. Buckley, C. G. Van de Walle, and D. D. Awschalom. Quantum computing with defects. *Proceedings of the National Academy of Sciences of the United States of America*, 107(19):8513–8, 2010.

[6] I. Buluta, S. Ashhab, and F. Nori. Natural and artificial atoms for quantum computation. *Reports on Progress in Physics*, 74(10):104401, 2011.

[7] R. Warburton. Single spins in self-assembled quantum dots. *Nature materials*, 12(6):483–93, 2013.

[8] M. D. Shulman, O. E. Dial, S. P. Harvey, H. Bluhm, V. Umansky, and A. Yacoby. Demonstration of entanglement of electrostatically coupled singlet-triplet qubits. *Science*, 336(6078):202–5, 2012.

[9] K. De Greve, P. L. McMahon, D. Press, T. D. Ladd, D. Bisping, C. Schneider, M. Kamp, L. Worschech, S. Höfling, A. Forchel, and Y. Yamamoto. Ultrafast coherent control and suppressed nuclear feedback of a single quantum dot hole qubit. *Nature Physics*, 7(11):872–878, 2011.

[10] G. D. Fuchs, G. Burkard, P. V. Klimov, and D. D. Awschalom. A quantum memory intrinsic to single nitrogen-vacancy centres in diamond. *Nature Physics*, 7(10):789–793, 2011.

[11] H. Bernien, B. Hensen, W. Pfaff, G. Koolstra, M. S. Blok, L. Robledo, T. H. Taminiau, M. Markham, D. J. Twitchen, L. Childress, and R. Hanson. Heralded entanglement between solid-state qubits separated by three metres. *Nature*, 497(7447):86–90, 2013.

[12] J. J. Pla, K. Y. Tan, J. P. Dehollain, W. H. Lim, J. J. L. Morton, D. N. Jamieson, A. S. Dzurak, and A. Morello. A single-atom electron spin qubit in silicon. *Nature*, 489(7417):541–5, 2012.

[13] D. Bimberg, M. Grundmann, and N. N. Ledentsov. *Quantum Dot Heterostructures*. Wiley, New York, 1999.

[14] C. Delerue and M. Lannoo. *Nanostructures: Theory and Modeling*. Springer: Berlin, 2004.

[15] T. Dietl. Hole-mediated ferromagnetism in tetrahedrally coordinated semiconductors. *Physical Review B*, 63(19):195205, 2001.

[16] K. A. Kikoin and V. N. Fleurov. *Transition Metal Impurities in Semiconductors*. World Scientific Pub Co Inc, 1994.

[17] A. M. Yakunin, A. Silov, P. M. Koenraad, J. Wolter, W. Van Roy, J. De Boeck, J. M. Tang, and M. E. Flatté. Spatial Structure of an Individual Mn Acceptor in GaAs. *Physical Review Letters*, 92(21):216806, 2004.

[18] S. Sanguinetti and N. Koguchi. *Droplet epitaxy of nanostructures*. Elsevier, 2013.

[19] T. Mano, T. Kuroda, S. Sanguinetti, T. Ochiai, T. Tateno, J. Kim, T. Noda, M. Kawabe, K. Sakoda, G. Kido, and N. Koguchi. Self-assembly of concentric quantum double rings. *Nano Letters*, 5(3):425–8, 2005.

[20] M. Hanke, M. Schmidbauer, D. Grigoriev, P. Schäfer, R. Khöler, T. H. Metzger, Z. M. Wang, Y. I. Mazur, and G. J. Salamo. Zero-strain GaAs quantum dot molecules as investigated by x-ray diffuse scattering. *Applied Physics Letters*, 89(5):053116, 2006.

[21] C. Heyn, A. Stemmann, A. Schramm, H. Welsch, W. Hansen, and A. Nemcsics. Faceting during GaAs quantum dot self-assembly by droplet epitaxy. *Applied Physics Letters*, 90(20):203105, 2007.

[22] B. Liang, A. Lin, N. Pavarelli, C. Reyner, J. Tatebayashi, K. Nunna, J. He, T. J. Ochalski, G. Huyet, and D. L. Huffaker. GaSb/GaAs type-II quantum dots grown by droplet epitaxy. *Nanotechnology*, 20(45):455604, 2009.

[23] M. DeJarld, K. Reyes, P. Smereka, and J. M. Millunchick. Mechanisms of ring and island formation in lattice mismatched droplet epitaxy. *Applied Physics Letters*, 102(13):133107, 2013.

[24] C. Somaschini, S. Bietti, N. Koguchi, and S. Sanguinetti. Coupled quantum dot-ring structures by droplet epitaxy. *Nanotechnology*, 22(18):185602, 2011.

[25] L. Besombes, Y. Léger, L. Maingault, D. Ferrand, H. Mariette, and J. Cibert. Probing the Spin State of a Single Magnetic Ion in an Individual Quantum Dot. *Physical Review Letters*, 93(20):207403, 2004.

[26] S. Boyer-Richard, C. Robert, L. Gérard, J.-P. Richters, R. André, J. Bleuse, H. Mariette, J. Even, and J.-M. Jancu. Atomistic simulations of the optical absorption of type-II CdSe/ZnTe superlattices. *Nanoscale research letters*, 7(1):543, 2012.

[27] G. Binnig, H. Rohrer, C. Gerber, and E. Weibel. Surfaces Studies by Scanning Tunneling Microscopy. *Physical Review Letters*, 49(1):57–61, 1982.

[28] G. Binnig, H. Rohrer, C. Gerber, and E. Weibel. Tunneling through a controllable vacuum gap. *Applied Physics Letters*, 40(2):178, 1982.

[29] A. Messiah. *Mécanique quantique*. 2nd edition, 1995.

[30] J. Bardeen. Tunnelling from a Many-Particle Point of View. *Physical Review Letters*, 6(2):57–59, 1961.

[31] J. Tersoff and R. Hamann, D. Theory and application of the Scanning Tunneling Microscope. *Physical Review Letters*, 50(25):1998–2001, 1983.

[32] J. Tersoff and D. R. Hamann. Theory of the scanning tunneling microscope. *Physical Review B*, 31(2):805–813, 1985.

[33] C. J. Chen. *Introduction to Scanning Tunneling Microscopy*. Oxford University Press, 1st editio edition, 1993.

[34] S. Y. Tong, A. R. Lubinsky, B. J. Mrstik, and M. A. V. Hove. Surface bond angle and bond lengths of rearranged As and Ga atoms on GaAs (110). *Physical Review B*, 17(8), 1978.

[35] A. Lubinsky, C. Duke, B. Lee, and P. Mark. Semiconductor Surface Reconstruction: The Rippled Geometry of GaAs(110). *Physical Review Letters*, 36(17):1058–1061, 1976.

[36] J. R. Chelikomsky and L. Cohen. Self-consistent pseudopotential calculation for the relaxed (110) surface of GaAs. *Physical Review B*, 20(10), 1979.

[37] A. Ruocco, M. Biagini, A. di Bona, S. Gambacorti, S. Valeri, and S. Nannarone. Clean and hydrogenated GaAs (110) surface-structure relaxation. *Physical Review B*, 51(4), 1995.

[38] J. L. A. Alves, K. Watari, and A. C. Ferraz. Calculated atomic structures of ZnS, Znse and ZnTe (110) surfaces. *Solid State Communications*, 87(11):1001–1004, 1993.

[39] M. D. Pashley, K. W. Haberern, R. M. Feenstra, and P. D. Kirchner. Different Fermi-level pinning behavior on n- and p-type GaAs(001). *Physical review. B*, 48(7):4612–4615, 1993.

[40] N. Ishida, K. Sueoka, and R. Feenstra. Influence of surface states on tunneling spectra of n-type GaAs(110) surfaces. *Physical Review B*, 80(7):075320, 2009.

[41] G. J. de Raad, D. M. Bruls, P. M. Koenraad, and J. H. Wolter. STM observations of GaAs(110) showing the top and bottom zig-zag rows of the surface. *Physical Review B*, 64(7):075314, 2001.

[42] R. M. Feenstra. Electrostatic potential for a hyperbolic probe tip near a semiconductor. *Journal of Vacuum Science & Technology B*, 21(5):2080, 2003.

[43] G. R. Liu and S. S. Quek Jerry. A finite element study of the stress and strain fields of InAs quantum dots embedded in GaAs. *Semicond. Sci. Technol.*, 17:630–643, 2002.

[44] P. Offermans, P. M. Koenraad, J. H. Wolter, K. Pierz, M. Roy, and P. Maksym. Atomic-scale structure and photoluminescence of InAs quantum dots in GaAs and AlAs. *Physical Review B*, 72(16):165332, 2005.

[45] P. Ebert. Nano-scale properties of defects in compound semiconductor surfaces. *Surface Science Reports*, 33(4-8):121–303, 1999.

[46] R. de Kort, M. van der Wielen, A. van Roij, W. Kets, and H. van Kempen. Zn- and Cd-induced features at the GaAs(110) and InP(110) surfaces studied by low-temperature scanning tunneling microscopy. *Physical Review B*, 63(12):125336, 2001.

[47] A. P. Wijnheijmer, J. K. Garleff, K. Teichmann, M. Wenderoth, S. Loth, and P. M. Koenraad. Single Si dopants in GaAs studied by scanning tunneling microscopy and spectroscopy. *Physical Review B*, 84(12):125310, 2011.

[48] R. de Kort, W. Kets, and H. van Kempen. A low-temperature scanning tunneling microscopy study on the Sn- and Zn-doped InP(110) surfaces. *Surface Science*, 482-485:495–500, 2001.

[49] A. Depuydt, C. Van Haesendonck, S. V. Savinov, and V. I. Panov. Low-temperature scanning tunneling microscopy of subsurface shallow dopants : depth dependence of the corrugation for the GaAs (110) surface. *Applied Physics A*, 72:209–212, 2001.

[50] K. Teichmann, M. Wenderoth, S. Loth, R. Ulbrich, J. K. Garleff, A. P. Wijnheijmer, and P. M. Koenraad. Controlled Charge Switching on a Single Donor with a Scanning Tunneling Microscope. *Physical Review Letters*, 101(7):076103, 2008.

[51] A. P. Wijnheijmer, J. K. Garleff, K. Teichmann, M. Wenderoth, S. Loth, R. Ulbrich, P. Maksym, M. Roy, and P. M. Koenraad. Enhanced Donor Binding Energy Close to a Semiconductor Surface. *Physical Review Letters*, 102(16):166101, 2009.

[52] G. Mahieu, B. Grandidier, D. Deresmes, J. Nys, D. Stiévenard, and P. Ebert. Direct Evidence for Shallow Acceptor States with Nonspherical Symmetry in GaAs. *Physical Review Letters*, 94(2):026407, 2005.

[53] S. Loth, M. Wenderoth, L. Winking, R. Ulbrich, S. Malzer, and G. Döhler. Probing Semiconductor Gap States with Resonant Tunneling. *Physical Review Letters*, 96(6):066403, 2006.

[54] S. Loth, M. Wenderoth, L. Winking, R. G. Ulbrich, S. Malzer, and G. H. Döhler. Depth Resolved Scanning Tunneling Spectroscopy of Shallow Acceptors in Gallium Arsenide. *Japanese Journal of Applied Physics*, 45(3B):2193–2196, 2006.

[55] D. Kitchen, A. Richardella, J.-M. Tang, M. E. Flatté, and A. Yazdani. Atom-by-atom substitution of Mn in GaAs and visualization of their hole-mediated interactions. *Nature*, 442(7101):436–9, 2006.

[56] J. K. Garleff, C. Çelebi, W. Van Roy, J.-M. Tang, M. E. Flatté, and P. M. Koenraad. Atomically precise impurity identification and modification on the manganese doped GaAs(110) surface with scanning tunneling microscopy. *Physical Review B*, 78(7):075313, 2008.

[57] S. Loth, M. Wenderoth, and R. Ulbrich. Asymmetry of acceptor wave functions caused by surface-related strain and electric field in InAs. *Physical Review B*, 77(11):115344, 2008.

[58] C. Çelebi, P. M. Koenraad, A. Silov, W. Van Roy, A. Monakhov, J.-M. Tang, and M. E. Flatté. Anisotropic spatial structure of deep acceptor states in GaAs and GaP. *Physical Review B*, 77(7):075328, 2008.

[59] R. M. Feenstra. Tunneling spectroscopy of the GaAs(110) surface. *Journal of Vacuum Science & Technology B*, 5(4):923, 1987.

[60] G. J. de Raad, P. M. Koenraad, and J. H. Wolter. Use of the Schiller decapitation process for the manufacture of high quality tungsten scanning tunneling microscopy tips. *Journal of Vacuum Science & Technology B*, 17(5):1946, 1999.

[61] P. M. Koenraad and M. E. Flatté. Single dopants in semiconductors. *Nature Materials*, 10(2):91–100, 2011.

[62] A. Asenov, A. R. Brown, J. H. Davies, S. Kaya, and G. Slavcheva. Simulation of Intrinsic Parameter Fluctuations in in Decananometer and Nanometer-Scale MOSFETs. *IEEE Transactions on Electron Devices*, 50(9):1837–1852, 2003.

[63] T. Shinada, S. Okamoto, T. Kobayashi, and I. Ohdomari. Enhancing semiconductor device performance using ordered dopant arrays. *Nature*, 437(7062):1128–31, 2005.

[64] M. Fuechsle, J. a. Miwa, S. Mahapatra, H. Ryu, S. Lee, O. Warschkow, L. C. L. Hollenberg, G. Klimeck, and M. Y. Simmons. A single-atom transistor. *Nature Nanotechnology*, 7(4):242–6, 2012.

[65] S. Schofield, N. Curson, M. Simmons, F. Rueß, T. Hallam, L. Oberbeck, and R. Clark. Atomically Precise Placement of Single Dopants in Si. *Physical Review Letters*, 91(13):136104, 2003.

[66] D. H. Lee and J. A. Gupta. Tunable field control over the binding energy of single dopants by a charged vacancy in GaAs. *Science*, 330(6012):1807–10, 2010.

[67] D. Lee and J. Gupta. Tunable control over the ionization state of single Mn acceptors in GaAs with defect-induced band bending. *Nano Letters*, 11:2004–2007, 2011.

[68] J. M. Tang and M. E. Flatté. Multiband Tight-Binding Model of Local Magnetism in Ga1-xMnxAs. *Physical Review Letters*, 92(4):047201, 2004.

[69] T. O. Strandberg, C. M. Canali, and a. H. MacDonald. Chern Number Spins of Mn Acceptor Magnets in GaAs. *Physical Review Letters*, 106(1):017202, 2011.

[70] F. Jelezko and J. Wrachtrup. Single defect centres in diamond: A review. *Physica Status Solidi (a)*, 203(13):3207–3225, 2006.

[71] A. J. Heinrich, J. A. Gupta, C. P. Lutz, and D. M. Eigler. Single-atom spin-flip spectroscopy. *Science*, 306(5695):466–9, 2004.

[72] A. Yakunin, A. Silov, P. M. Koenraad, W. Van Roy, J. De Boeck, and J. H. Wolter. Charge manipulation and imaging of the Mn acceptor state in GaAs by cross-sectional scanning tunneling microscopy. *Superlattices and Microstructures*, 34(3-6):539–545, 2003.

[73] J. K. Garleff, A. P. Wijnheijmer, C. N. v. d. Enden, and P. M. Koenraad. Bistable behavior of silicon atoms in the (110) surface of gallium arsenide. *Physical Review B*, 84(7):075459, 2011.

[74] A. M. Yakunin, A. Silov, P. M. Koenraad, J. M. Tang, M. E. Flatté, J. L. Primus, W. Van Roy, J. De Boeck, A. M. Monakhov, K. S. Romanov, I. E. Panaiotti, and N. S. Averkiev. Warping a single Mn acceptor wavefunction by straining the GaAs host. *Nature materials*, 6(7):512–5, 2007.

[75] J. K. Garleff, A. P. Wijnheijmer, A. Y. Silov, J. van Bree, W. Van Roy, J. M. Tang, M. E. Flatté, and P. M. Koenraad. Enhanced binding energy of manganese acceptors close to the GaAs(110) surface. *Physical Review B*, 82(3):035303, 2010.

[76] T. S. e. Pantelides. *Deep centers in Semiconductors: A State of the Art Approach.* Gordon and Breach, Philadelphia, 2nd edition, 1992.

[77] A. Richardella, D. Kitchen, and A. Yazdani. Mapping the wave function of transition metal acceptor states in the GaAs surface. *Physical Review B*, 80(4):045318, 2009.

[78] M. Bozkurt, V. A. Grant, J. M. Ulloa, R. P. Campion, C. T. Foxon, E. Marega, G. J. Salamo, and P. M. Koenraad. Atomic scale characterization of Mn doped InAs/GaAs quantum dots. *Applied Physics Letters*, 96(4):042108, 2010.

[79] A. Nazmul, S. Sugahara, and M. Tanaka. MBE growth, structural, and transport properties of Mn δ-doped GaAs Layers. *Journal of Crystal Growth*, 251(1-4):303–310, 2003.

[80] E. F. Schubert, H. S. Luftman, and L. C. Hopkins. Fermi-level-pinning-induced impurity redistribution in semiconductors during epitaxial growth. *Physical Review B*, 42(2):1364–1369, 1990.

[81] K. Sato, J. Kudrnovský, P. H. Dederichs, O. Eriksson, I. Turek, B. Sanyal, G. Bouzerar, H. Katayama-Yoshida, V. A. Dinh, T. Fukushima, H. Kizaki, and R. Zeller. First-principles theory of dilute magnetic semiconductors. *Reviews of Modern Physics*, 82(2):1633–1690, 2010.

[82] K. Sato, H. Katayama-Yoshida, and P. H. Dederichs. High Curie Temperature and Nano-Scale Spinodal Decomposition Phase in Dilute Magnetic Semiconductors. *Japanese Journal of Applied Physics*, 44(No. 30):L948–L951, 2005.

[83] H. Katayama-Yoshida, K. Sato, T. Fukushima, M. Toyoda, H. Kizaki, V. A. Dinh, and P. H. Dederichs. Theory of ferromagnetic semiconductors. *Physica Status Solidi (a)*, 204(1):15–32, 2007.

[84] T. Dietl. Origin and control of ferromagnetism in dilute magnetic semiconductors and oxides (invited). *Journal of Applied Physics*, 103(7):07D111, 2008.

[85] E. Malguth, A. Hoffmann, and M. R. Phillips. Fe in III-V and II-VI semiconductors. *Physica Status Solidi (b)*, 245(3):455–480, 2008.

[86] K. Pressel, A. Dornen, G. Ruckert, and K. Thonke. Charge-transfer transitions and pseudoacceptor states of iron in gallium phosphide. *Physical Review B*, 47(24):16267–16273, 1993.

[87] M. C. van der Wielen, A. J. van Roij, and H. van Kempen. Direct observation of Friedel oscillations around incorporated SiGa dopants in GaAs by low-temperature scanning tunneling microscopy. *Physical Review Letters*, 76(7):1075–1078, 1996.

[88] D. Kitchen, A. Richardella, P. Roushan, J.-M. Tang, M. Flatté, and A. Yazdani. Hole-mediated interactions of Mn acceptors on GaAs (110) (invited). *Journal of Applied Physics*, 101(9):09G515, 2007.

[89] D. Chadi. Spin-orbit splitting in crystalline and compositionally disordered semiconductors. *Physical Review B*, 16(2):790–796, 1977.

[90] H. Hjalmarson, P. Vogl, D. Wolford, and J. Dow. Theory of Substitutional Deep Traps in Covalent Semiconductors. *Physical Review Letters*, 44(12):810–813, 1980.

[91] P. Vogl and J. Baranowski. No Title. *Acta Physica Polonica A*, 67(133), 1985.

[92] G. F. Koster and J. C. Slater. Simplified Impurity Calculation. *Physical Review*, 96(5), 1954.

[93] C. Çelebi, J. K. Garleff, A. Silov, A. Yakunin, P. M. Koenraad, J.-M. Tang, and M. E. Flatté. Surface Induced Asymmetry of Acceptor Wave Functions. *Physical Review Letters*, 104(8):086404, 2010.

[94] H. Prüser, M. Wenderoth, P. E. Dargel, A. Weismann, R. Peters, T. Pruschke, and R. G. Ulbrich. Long-range Kondo signature of a single magnetic impurity. *Nature Physics*, 7(3):203–206, 2011.

[95] B. C. Stipe, M. A. Rezaei, and W. Ho. Single-Molecule Vibrational Spectroscopy and Microscopy. *Science*, 280(5370):1732–1735, 1998.

[96] L. C. Davis. Impurity-Assisted Inelastic Tunneling: Many-Electron Theory. *Physical Review B*, 2(6):1714–1732, 1970.

[97] A. Bayman, P. K. Hansma, and W. C. Kaska. Shifts and dips in inelastic-electron-tunneling spectra due to the tunnel junction environment. *Physical Review B*, 24(5):2449–2455, 1981.

[98] B. N. Persson and A. Baratoff. Inelastic Electron Tunneling from a Metal Tip: The Contribution from Resonant Processes. *Physical Review Letters*, 59(3):339–342, 1987.

[99] A. Baratoff and B. N. J. Persson. Theory of the local tunneling spectrum of a vibrating adsorbate. *Journal of Vacuum Science & Technology A*, 6:331–335, 1988.

[100] B. Clerjaud. Transition-metal impurities in III-V compounds. *J. Phys. C: Solid State Phys.*, 18:3615, 1985.

[101] M. A. Kastner. Artificial atoms. *Physics Today*, 46:24, 1993.

[102] G. Narvaez, G. Bester, and A. Zunger. Excitons, biexcitons, and trions in self-assembled (In,Ga)As\GaAs quantum dots: Recombination energies, polarization, and radiative lifetimes versus dot height. *Physical Review B*, 72(24):245318, 2005.

[103] J.-W. Luo and A. Zunger. Geometry of epitaxial GaAs/(Al,Ga)As quantum dots as seen by excitonic spectroscopy. *Physical Review B*, 84(23):235317, 2011.

[104] P. Bhattacharya and Z. Mi. Quantum-Dot Optoelectronic Devices. In *Proceedings of the IEEE*, volume 95, pages 1723–1740, 2007.

[105] P. Martyniuk and A. Rogalski. Quantum-dot infrared photodetectors: Status and outlook. *Progress in Quantum Electronics*, 32(3-4):89–120, 2008.

[106] G. Scalari, C. Walther, M. Fischer, R. Terazzi, H. Beere, D. Ritchie, and J. Faist. THz and sub-THz quantum cascade lasers. *Laser & Photonics Review*, 3(1-2):45–66, 2009.

[107] E. A. Zibik, T. Grange, B. A. Carpenter, N. E. Porter, R. Ferreira, G. Bastard, D. Stehr, S. Winnerl, M. Helm, H. Y. Liu, M. S. Skolnick, and L. R. Wilson. Long lifetimes of quantum-dot intersublevel transitions in the terahertz range. *Nature Materials*, 8(10):803–7, 2009.

[108] A. Tredicucci. Quantum dots: Long life in zero dimensions. *Nature Materials*, 8(10):775–6, 2009.

[109] T. Akiyama, M. Ekawa, M. Sugawara, K. Kawaguchi, A. Kuramata, H. Ebe, and Y. Arakawa. An ultrawide-band semiconductor optical amplifier having an extremely high penalty-free output power of 23 dBm achieved with quantum dots. *IEEE Photonics Technology Letters*, 17(8):1614–1616, 2005.

[110] S. Strauf, N. G. Stoltz, M. T. Rakher, L. A. Coldren, P. M. Petroff, and D. Bouwmeester. High-frequency single-photon source with polarization control. *Nature Photonics*, 1(12):704–708, 2007.

[111] A. Mellor, A. Luque, I. Tobias, and A. Marti. The influence of quantum dot size on the sub-bandgap intraband photocurrent in intermediate band solar cells. *Applied Physics Letters*, 101(13):133909, 2012.

[112] A. D. Yoffe. Advances in Physics Low-dimensional systems : Quantum size effects and electronic properties of semiconductor microcrystallites (zero- dimensional systems) and some quasi-two-dimensional systems. *Advances in Physics*, 51(2):799–890, 2002.

[113] X. Li, Y. Wu, D. Steel, D. Gammon, T. H. Stievater, D. S. Katzer, D. Park, C. Piermarocchi, and L. J. Sham. An all-optical quantum gate in a semiconductor quantum dot. *Science*, 301(5634):809–11, 2003.

[114] C. L. Salter, R. M. Stevenson, I. Farrer, C. A. Nicoll, D. A. Ritchie, and A. J. Shields. An entangled-light-emitting diode. *Nature*, 465(7298):594–7, 2010.

[115] S. Kiravittaya, A. Rastelli, and O. G. Schmidt. Advanced quantum dot configurations. *Reports on Progress in Physics*, 72(4):046502, 2009.

[116] J. T. Robinson, A. Rastelli, O. Schmidt, and O. D. Dubon. Global faceting behavior of strained Ge islands on Si. *Nanotechnology*, 20(8):085708, 2009.

[117] N. Koguchi. New selective molecular-beam epitaxial growth method for direct formation of GaAs quantum dots. *Journal of Vacuum Science & Technology B*, 11(3):787, 1993.

[118] K. Watanabe, N. Koguchi, and Y. Otoh. Fabrication of GaAs Quantum Dots by Modified Droplet Epitaxy. *Japanese Journal of Applied Physics*, 39(2):79–81, 2000.

[119] M. Abbarchi, T. Kuroda, T. Mano, K. Sakoda, C. A. Mastrandrea, A. Vinattieri, M. Gurioli, and T. Tsuchiya. Energy renormalization of exciton complexes in GaAs quantum dots. *Physical Review B*, 82(20):201301, 2010.

[120] Z. M. Wang, K. Holmes, J. L. Shultz, and G. J. Salamo. Self-assembly of GaAs holed nanostructures by droplet epitaxy. *Physica Status Solidi (a)*, 202(8):R85–R87, 2005.

[121] A. Urbanczyk, J. G. Keizer, P. M. Koenraad, and R. Notzel. Long wavelength (>1.55 μm) room temperature emission and anomalous structural properties of InAs/GaAs quantum dots obtained by conversion of In nanocrystals. *Applied Physics Letters*, 102(7):073103, 2013.

[122] J. G. Keizer, M. Jo, T. Mano, T. Noda, K. Sakodam, and P. M. Koenraad. Structural atomic-scale analysis of GaAs/AlGaAs quantum wires and quantum dots grown by droplet epitaxy on a (311)A substrate. *Applied Physics Letters*, 98(19):193112, 2011.

[123] C. Somaschini, S. Bietti, N. Koguchi, and S. Sanguinetti. Fabrication of multiple concentric nanoring structures. *Nano Letters*, 9(10):3419–24, 2009.

[124] C. Somaschini, S. Bietti, A. Scaccabarozzi, E. Grilli, and S. Sanguinetti. Self-Assembly of Quantum Dot-Disk Nanostructures via Growth Kinetics Control. *Crystal Growth & Design*, 12(3):1180–1184, 2012.

[125] C. Somaschini, S. Bietti, N. Koguchi, and S. Sanguinetti. Shape control via surface reconstruction kinetics of droplet epitaxy nanostructures. *Applied Physics Letters*, 97(20):203109, 2010.

[126] A. Ohtake. Surface reconstructions on GaAs(001). *Surface Science Reports*, 63(7):295–327, 2008.

[127] J. G. Keizer, J. Bocquel, P. M. Koenraad, T. Mano, T. Noda, and K. Sakoda. Atomic scale analysis of self assembled GaAs/AlGaAs quantum dots grown by droplet epitaxy. *Applied Physics Letters*, 96(6):062101, 2010.

[128] J. G. Keizer, M. Bozkurt, J. Bocquel, T. Mano, T. Noda, K. Sakoda, E. C. Clark, M. Bichler, G. Abstreiter, J. J. Finley, W. Lu, T. Rohel, H. Folliot, N. Bertru, and P. M. Koenraad. Shape control of quantum dots studied by cross-sectional scanning tunneling microscopy. *Journal of Applied Physics*, 109(10):102413, 2011.

[129] A. Nemcsics, L. Tóth, L. Dobos, and A. Stemmann. Facetting of the self-assembled droplet epitaxial GaAs quantum dot. *Microelectronics Reliability*, 51(5):927–930, 2011.

[130] A. Rastelli and H. von Känel. Island formation and faceting in the SiGe/Si() system. *Surface Science*, 532-535:769–773, 2003.

[131] A. Rastelli, M. Stoffel, J. Tersoff, G. Kar, and O. Schmidt. Kinetic Evolution and Equilibrium Morphology of Strained Islands. *Physical Review Letters*, 95(2):026103, 2005.

[132] G. Costantini, A. Rastelli, C. Manzano, P. Acosta-Diaz, G. Katsaros, R. Songmuang, O. G. Schmidt, H. V. Känel, and K. Kern. Pyramids and domes in the InAs/GaAs(001) and Ge/Si(001) systems. *Journal of Crystal Growth*, 278(1-4):38–45, 2005.

[133] C.-D. Lee, C. Park, H. J. Lee, S. K. Noh, K.-S. Lee, and S.-J. Park. Formation of self-assembled GaAs/AlGaAs quantum dots by low-temperature epitaxy. *Applied Physics Letters*, 73(18):2615, 1998.

[134] K. Reyes, P. Smereka, D. Nothern, J. M. Millunchick, S. Bietti, C. Somaschini, S. Sanguinetti, and C. Frigeri. Unified model of droplet epitaxy for compound semiconductor nanostructures: Experiments and theory. *Physical Review B*, 87(16):165406, 2013.

[135] J. H. Neave, P. J. Dobson, B. A. Joyce, and J. Zhang. Reflection high-energy electron diffraction oscillations from vicinal surfaces - a new approach to surface diffusion measurements. *Applied Physics Letters*, 47(2):100, 1985.

[136] S. Bietti, C. Somaschini, and S. Sanguinetti. Crystallization kinetics of Ga metallic nano-droplets under As flux. *Nanotechnology*, 24(20):205603, 2013.

[137] J. Crank. *The Mathematics of Diffusion*. Clarendon Press. Oxford, 1955.

[138] K. Ohta, T. Kojima, and T. Nakagawa. Anisotropic surface migration of Ga atoms on GaAs (001). *Journal of Crystal Growth*, 95:71–74, 1989.

[139] V. P. LaBella, D. W. Bullock, Z. Ding, C. Emery, W. G. Harter, and P. M. Thibado. Monte Carlo derived diffusion parameters for Ga on the GaAs(001)-(2x4) surface: A molecular beam epitaxy-scanning tunneling microscopy study. *Journal of Vacuum Science & Technology A*, 18(4):1526, 2000.

[140] J. Hirth and G. A. I. Pound. Coefficients of evaporation and condensation. *Journal of Physical Chemistry*, 64:619–26, 1960.

[141] M. Jo, T. Mano, and K. Sakoda. Unstrained GaAs Quantum Dashes Grown on GaAs(001) Substrates by Droplet Epitaxy. *Applied Physics Express*, 3(4):045502, 2010.

[142] S. Adorno, S. Bietti, and S. Sanguinetti. Annealing induced anisotropy in GaAs/AlGaAs quantum dots grown by droplet epitaxy. *Journal of Crystal Growth*, pages 1–4, 2012.

[143] J. G. Keizer, A. B. Henriques, A. D. B. Maia, A. A. Quivy, and P. M. Koenraad. Atomically resolved study of the morphology change of InAs/GaAs quantum dot layers induced by rapid thermal annealing. *Applied Physics Letters*, 101(24):243113, 2012.

[144] Z. M. Wang, B. L. Liang, K. A. Sablon, and G. J. Salamo. Nanoholes fabricated by self-assembled gallium nanodrill on GaAs(100). *Applied Physics Letters*, 90(11):113120, 2007.

[145] A. Stemmann, T. Koppen, M. Grave, S. Wildfang, S. Mendach, W. Hansen, and C. Heyn. Local etching of nanoholes and quantum rings with In(x)Ga(1-x) droplets. *Journal of Applied Physics*, 106(6):064315, 2009.

[146] C. Heyn, A. Stemmann, and W. Hansen. Dynamics of self-assembled droplet etching. *Applied Physics Letters*, 95(17):173110, 2009.

[147] C. Heyn. Kinetic model of local droplet etching. *Physical Review B*, 83(16):165302, 2011.

[148] A. Stemmann, C. Heyn, T. Koppen, T. Kipp, and W. Hansen. Local droplet etching of nanoholes and rings on GaAs and AlGaAs surfaces. *Applied Physics Letters*, 93(12):123108, 2008.

[149] C. Heyn, A. Stemmann, R. Eiselt, and W. Hansen. Influence of Ga coverage and As pressure on local droplet etching of nanoholes and quantum rings. *Journal of Applied Physics*, 105(5):054316, 2009.

[150] T. F. Kelly and M. K. Miller. Invited review article: Atom probe tomography. *The Review of scientific instruments*, 78(3):031101, 2007.

[151] A. D. Giddings, J. G. Keizer, M. Hara, G. J. Hamhuis, H. Yuasa, H. Fukuzawa, and P. M. Koenraad. Composition profiling of InAs quantum dots and wetting layers by atom probe tomography and cross-sectional scanning tunneling microscopy. *Physical Review B*, 83(20):205308, 2011.

[152] S. Sanguinetti, K. Watanabe, T. Kuroda, F. Minami, Y. Gotoh, and N. Koguchi. Effects of post-growth annealing on the optical properties of self-assembled GaAs/AlGaAs quantum dots. *Journal of Crystal Growth*, 242(3-4):321–331, 2002.

[153] V. Mantovani, S. Sanguinetti, M. Guzzi, E. Grilli, M. Gurioli, K. Watanabe, and N. Koguchi. Low density GaAs/AlGaAs quantum dots grown by modified droplet epitaxy. *Journal of Applied Physics*, 96(8):4416, 2004.

[154] W. Feng, F. Chen, W. Q. Cheng, Q. Huang, and J. M. Zhou. Influence of growth conditions on Al-Ga interdiffusion in low-temperature grown AlGaAs/GaAs multiple quantum wells. *Applied Physics Letters*, 71(12):1676, 1997.

[155] J. M. Moison, C. Guille, F. Houzay, F. Barthe, and Van Rompay M. Surface segregation of third-column atoms in group III-V arsenide compounds: Ternary alloys and heterostructures. *Physical review. B, Condensed matter*, 40(9):6149–6162, 1989.

[156] N. Kleemans, J. van Bree, M. Bozkurt, P. van Veldhoven, P. Nouwens, R. Nötzel, A. Silov, P. M. Koenraad, and M. E. Flatté. Size-dependent exciton g factor in self-assembled InAs/InP quantum dots. *Physical Review B*, 79(4):045311, 2009.

[157] Y.-A. Liao, W.-T. Hsu, S.-H. Huang, P.-C. Chiu, J.-I. Chyi, and W.-H. Chang. Band alignment tuning of InAs quantum dots with a thin AlGaAsSb capping layer. *Applied Physics Letters*, 102(17):173104, 2013.

[158] J. M. Ulloa, I. W. D. Drouzas, P. M. Koenraad, D. J. Mowbray, M. J. Steer, H. Y. Liu, and M. Hopkinson. Suppression of InAs/GaAs quantum dot decomposition by the incorporation of a GaAsSb capping layer. *Applied Physics Letters*, 90(21):213105, 2007.

[159] C.-T. Huang, Y.-C. Chen, and S.-C. Lee. Improved photoresponse of InAs/GaAs quantum dot infrared photodetectors by using GaAs(1-x)Sb(x) strain reducing layer. *Applied Physics Letters*, 100(4):043512, 2012.

[160] J. M. Ulloa, P. M. Koenraad, E. Gapihan, A. Letoublon, and N. Bertru. Double capping of molecular beam epitaxy grown InAs/InP quantum dots studied by cross-sectional scanning tunneling microscopy. *Applied Physics Letters*, 91(7):073106, 2007.

[161] J. G. Keizer, E. C. Clark, M. Bichler, G. Abstreiter, J. J. Finley, and P. M. Koenraad. An atomically resolved study of InGaAs quantum dot layers grown with an indium flush step. *Nanotechnology*, 21(21):215705, 2010.

[162] M. Jo, T. Mano, and K. Sakoda. Morphological control of GaAs quantum dots grown by droplet epitaxy using a thin AlGaAs capping layer. *Journal of Applied Physics*, 108(8):083505, 2010.

[163] H. Saito, V. Zayets, S. Yamagata, and K. Ando. Room-Temperature Ferromagnetism in a II-VI Diluted Magnetic Semiconductor Zn1-xCrxTe. *Physical Review Letters*, 90(20):207202, 2003.

[164] D. Ferrand, J. Cibert, A. Wasiela, C. Bourgognon, S. Tatarenko, G. Fishman, T. Andrearczyk, J. Jaroszynski, S. Koleśnik, T. Dietl, B. Barbara, and D. Dufeu. Carrier-induced ferromagnetism in p-Zn1-xMnxTe. *Physical Review B*, 63(8):085201, 2001.

[165] A. Tribu, G. Sallen, T. Aichele, R. André, J.-P. Poizat, C. Bougerol, S. Tatarenko, and K. Kheng. A high-temperature single-photon source from nanowire quantum dots. *Nano letters*, 8(12):4326–9, 2008.

[166] T. Aichele, A. Tribu, G. Sallen, J. Bocquel, E. Bellet-Amalric, C. Bougerol, J.-P. Poizat, K. Kheng, R. André, S. Tatarenko, and H. Mariette. CdSe quantum dots in ZnSe nanowires as efficient source for single photons up to 220K. *Journal of Crystal Growth*, 311(7):2123–2127, 2009.

[167] J. Kasprzak, M. Richard, S. Kundermann, A. Baas, P. Jeambrun, J. M. J. Keeling, F. M. Marchetti, M. H. Szymanska, R. André, J. L. Staehli, V. Savona, P. B. Littlewood, B. Deveaud, and L. S. Dang. Bose-Einstein condensation of exciton polaritons. *Nature*, 443(7110):409–14, 2006.

[168] I. Sellers, V. Whiteside, I. Kuskovsky, a. Govorov, and B. McCombe. Aharonov-Bohm Excitons at Elevated Temperatures in Type-II ZnTe/ZnSe Quantum Dots. *Physical Review Letters*, 100(13):136405, 2008.

[169] W. Faschinger, S. Ferreira, and H. Sitter. Doping limitations in wide gap II-VI compounds by Fermi level pinning. *Journal of Crystal Growth*, 151(3-4):267–272, 1995.

[170] A. Kley and J. Neugebauer. Atomic and electronic structure of the GaAs/ZnSe(001) interface. *Physical review. B, Condensed matter*, 50(12):8616–8628, 1994.

[171] M. C. Tamargo. Structural characterization of GaAs/ZnSe interfaces. *Journal of Vacuum Science & Technology B*, 6(2):784, 1988.

[172] D. Li, J. M. Gonsalves, N. Otsuka, J. Qiu, M. Kobayashi, and R. L. Gunshor. Structure of the ZnSe/GaAs heteroepitaxial interface. *Applied Physics Letters*, 57(5):449, 1990.

[173] S. Guha, H. Munekata, F. K. LeGoues, and L. L. Chang. Growth mode and dislocation distribution in the ZnSe/GaAs (100) system. *Applied Physics Letters*, 60(26):3220, 1992.

[174] T. Gleim, L. Weinhardt, T. Schmidt, R. Fink, C. Heske, E. Umbach, P. Grabs, G. Schmidt, L. W. Molenkamp, B. Richter, A. Fleszar, and H. P. SteinruÌĹck. Energy level alignment at zinc blende Cd(Mn)Se/ZnTe/InAs(100) interfaces. *Applied Physics Letters*, 81(20):3813, 2002.

[175] L. Ouyang, J. Fan, S. Wang, X. Lu, Y. H. Zhang, X. Liu, J. K. Furdyna, and D. J. Smith. Microstructural characterization of thick ZnTe epilayers grown on GaSb, InAs, InP and GaAs (100) substrates. *Journal of Crystal Growth*, 330(1):30–34, 2011.

[176] A. Wierts, J. M. Ulloa, C. CÌğelebi, P. M. Koenraad, H. Boukari, L. Maingault, R. AndreÌĄ, and H. Mariette. Cross-sectional scanning tunneling microscopy study on II-VI multilayer structures. *Applied Physics Letters*, 91(16):161907, 2007.

[177] C. Çelebi, O. Ari, and R. T. Senger. Cleavage induced rows of missing atoms on ZnTe (110) surface. *Physical Review B*, 87(8):085308, 2013.

[178] M. Grün, A. Haury, J. Cibert, and A. Wasiela. The nitrogen acceptor energy in ZnTe measured by Hall effect and optical spectroscopy. *Journal of Applied Physics*, 79(9):7386, 1996.

[179] T. Baron, S. Tatarenko, K. Saminadayar, N. Magnea, and J. Fontenille. Plasma nitrogen doping of ZnTe, Cd(1-x)Zn(x)Te, and CdTe by molecular beam epitaxy. *Applied Physics Letters*, 65(10):1284, 1994.

[180] T. Baron, K. Saminadayar, and N. Magnea. Nitrogen doping of Te-based II-VI compounds during growth by molecular beam epitaxy. *Journal of Applied Physics*, 83(3):1354, 1998.

[181] N. Samarth, H. Luo, J. K. Furdyna, S. B. Qadri, Y. R. Lee, A. K. Ramdas, and N. Otsuka. Growth of cubic (zinc blende) CdSe by molecular beam epitaxy. *Applied Physics Letters*, 54(26):2680, 1989.

[182] G. Brill, Y. Chen, P. M. Amirtharaj, W. Sarney, D. Chandler-Horowitz, and N. K. Dhar. Molecular beam epitaxial growth and characterization of Cd-based II-VI wide-bandgap compounds on Si substrates. *Journal of Electronic Materials*, 34(5):655–661, 2005.

[183] V. A. Kaygorodov, I. V. Sedova, S. V. Sorokin, A. A. Sitnikova, O. Nekrutkina, T. V. Shubina, A. A. Toropov, V. S. Sorokin, and S. V. Ivanov. Molecular Beam Epitaxy of Low-Strained CdSe/CdMgSe Heterostructures on InAs(001) Substrates. *Physica Status Solidi (b)*, 229(1):19–23, 2002.

[184] Y. M. Park, R. Andre, J. Kasprzak, L. S. Dang, and E. Bellet-Amalric. Molecular beam epitaxy of CdSe epilayers and quantum wells on ZnTe substrate. *Applied Surface Science*, 253(16):6946–6950, 2007.

[185] H. Luo, N. Samarth, F. C. Zhang, a. Pareek, M. Dobrowolska, J. K. Furdyna, K. Mahalingam, N. Otsuka, W. C. Chou, a. Petrou, and S. B. Qadri. Molecular beam epitaxy of a low strain II-VI heterostructure: ZnTe/CdSe. *Applied Physics Letters*, 58(16):1783, 1991.

[186] D. Mourad, J.-P. Richters, L. Gérard, R. André, J. Bleuse, and H. Mariette. Determination of valence-band offset at cubic CdSe/ZnTe type-II heterojunctions: A combined experimental and theoretical approach. *Physical Review B*, 86(19):195308, 2012.

[187] C. Bodin, J. Cibert, W. Grieshaber, L. Si Dang, F. Marcenat, A. Wasiela, P. H. Jouneau, G. Feuillet, D. Hervé, and E. Molva. Growth, structural, and optical properties of II-VI layers: (001) CdMnTe grown by molecular-beam epitaxy. *Journal of Applied Physics*, 77(3):1069, 1995.

[188] S. L. Zhang, C. L. Yang, Y. T. Hou, Y. Jin, Z. L. Peng, J. Li, and S. X. Yuan. Defect-like nature of the interface in AB/CD-type superlattices. *Physical Review B*, 52(3), 1995.

[189] S.-F. Ren. Study of reconstruction at interfaces of CdSe/ZnTe superlattices by total energy calculations. *Journal of Vacuum Science & Technology B*, 13(4):1711, 1995.

[190] H. S. Lee, J. Y. Lee, T. W. Kim, D. U. Lee, D. C. Choo, and M. D. Kim. Simultaneous existence and atomic arrangement of CuPt-type and CuAu-I type ordered structures near ZnTe/ZnSe heterointerfaces. *Journal of Applied Physics*, 91(9):5657, 2002.

[191] H. S. Lee, J. Y. Lee, T. W. Kim, D. U. Lee, D. C. Choo, and H. L. Park. Coexistence behavior of the CuPt(B)-type and the CuAu-I-type ordered structures in highly strained Cd(x)Zn(1-x)Te/GaAs heterostructures. *Applied Physics Letters*, 79(11):1637, 2001.

Summary

Exploration of natural and self-assembled quantum structures.

The work presented in this thesis addresses specific issues for natural and self-assembled quantum structures. In the case of impurities in semiconductor crystals, the influence of electrostatic conditions on the electronic configuration of these dopants is investigated. The main challenge is to find the relation between the intrinsic properties of the impurities and their interactions with environment. In the case of self-assembled nanostructures, the relation between structural properties of nanostructures, like dimensions, chemical composition and interfaces and their conditions of assembly is investigated. The main goal is progressing towards homogenous and reproducible systems composed of several identical nanostructures.

The core of the investigations reported here were carried out at the atomic scale using Scanning Tunneling Microscopy (STM) and Spectroscopy (STS). This technique, representing by itself a direct application of a quantum effect called tunneling, is one of the most powerful tool developed to probe structures and single impurities at the nanoscale. STM and STS experiments were performed in cross-sectional geometry allowing the study of buried nanostructures and sub-surface impurities. The principles of Scanning Tunneling Microscopy on semiconductors surfaces are presented in chapter 1 and the applied experimental techniques are presented in Chapter 2. The rest of the thesis is divided in three exhaustive chapters dedicated to different quantum systems, addressing thereby different questions.

A natural quantum system is presented consisting of single Fe atoms in GaAs in chapter 3. The main reasons for studying this particular system are the nuclear spin of Fe impurities and the large binding energy of their acceptor level. Transition metals like Cr, Mn or Fe have partially filled *d*-shells, an attractive characteristic along the line of learning more about magnetic interactions at the atomic scale. Traditionally, transition metals are incorporated in semiconductors materials for one of the following reasons. They bring localized magnetic moments in the crystals which may interact and give rise to ferromagnetism. Several mechanisms are proposed, like carrier-mediated ferromagnetism. Fe impurities in GaAs were found to interact antiferromatically and therefore do not represent of system of interest in the field of diluted magnetic semiconductors. Transition metals atoms are also found in semiconductors materials in order to give them a semi-insulating properties. Transitions metals impurities introduce deep levels in the bandgap of most semiconductors which act as charge traps. The most common cases are Cr impurities in GaAs or Fe impurities in InP which are available as commercial wafers. Similarly, Fe impurities in GaAs reduces the conductivity. That being said, the main motivation for studying Fe in GaAs remains the exploration of fundamental physical processes. So far, only relatively shallow dopants have been investigated by STM and STS. Until now, Mn dopants in GaAs, with a binding energy of 113 meV, were the deepest dopants studied with these techniques. Their spatially distribution but also the spatial structure of their acceptor wave function were determined. Despite a higher binding energy, it appears from the X-STM studies that the Mn acceptor state has, like shallow acceptors, a relatively strong host-like character. Fe dopants in GaAs, with a binding energy of 510 meV, are the first deep and subsurface impurities for which an impurity-like character is expected. Another difference with previous studies is the multivalent character of Fe acceptors in GaAs. This system represents therefore an opportunity to establish the relation between a large binding energy and higher localization of the impurities states and the possibility a electronic or magnetic manipulation of these states. Besides, the manipulation of a single Fe impurity falls into the scope of the emerging field of solotronics. In this chapter, it is shown that a dilute distribution of the Fe impurities allows for imaging and manipulating the core d-states of a single Fe impurity. The electronic manipulation of the Fe states leads to STM observations similar to those on shallower dopants. Interestingly however, it was determined that the initial and final state not only have different charge states but also different valence states and spins. The observation of a disc around single Fe atoms in filled states images is a clear manifestation of such changes in charge and valence states of Fe impurities from $(Fe^{3+})^0$ to $(Fe^{2+})^-$. The isoelectronic Fe^{3+} configuration is the neutral state of the Fe acceptor, imaged at positive bias voltage. This statement is supported by the STS data indicating the presence of two levels, attributed to Fe, in the bandgap of GaAs. The relative position of these levels in is good agreement with the one established from optical spectroscopy experiments for the crystal field split states of e and t_2 symmetry of the $3d$-states of a single Fe impurity in GaAs. Moreover, the good agreement between the experimental localization of these states and the theoretical one provided by tight-binding calculations suggests that the anisotropy observed in the spatially resolved spectroscopy data can be directly linked to the symmetry of the orbitals as described by the group theory. The spatial mapping of the wave function of deep core d-states of an impurity by itself represents a stimulating achievement in the field of single impurities in semiconductors. The evidence of internal transition occurring on the Fe acceptor upon tunneling complete this solid picture of the energy levels of Fe dopants in GaAs.

In chapter 5 and chapter 6, two different self-assembled quantum systems are presented. These semiconductor nanostructures were grown by Molecular Beam Epitaxy. The two type of structures differ by the dimensionality of the quantum confinement pursed as well as by the material system: quantum dots in III-V semiconductors in the first case and multiple quantum wells in II-VI semiconductors in the second case. The study of self-assembled GaAs strain-free quantum dots in AlGaAs is presented in chapter 5. The major reason for investigating this specific structures is finding and assessing a reproducible method to grow quantum dots with specific optical emission. The conventional Stranski-Krastanov growth method can not be used here because GaAs and AlGaAs are lattice matched materials. Instead a more recent epitaxial technique is used called Droplet Epitaxy. Droplet Epitaxy is based on the kinetically limited processes of crystallization and diffusion. Consequently, a large number of degrees of freedom are available. This method has led to fabrication of a large variety of nanostructures like quantum dots, disc and rings. The absence of strain in GaAs/AlGaAs heterostructures is an particularly interesting characteristic considering that strain can not only shift the position of the energy levels in a quantum dot but also strongly influences the quantum dot formation. The systematic study reported here shows the change in morphology of the strain-free GaAs/AlGaAs quantum dots as a function of several growth parameters, like crystallization temperature, As flux and volume of Ga deposited. The experimental results are in good agreement with the analytical model proposed based on Ga diffusion dynamics and crystallization during the exposure of the Ga liquid droplet to the As flux. The ability to control QD faceting and aspect ratio of GaAs/AlGaAs DE-QDs is demonstrated. The QD shape is determined by the diffusion of Ga from the droplet on the As terminated surface during the As supply. QD faceting undergoes a continuous transition dependent on the initial droplet radius and the diffusion length at the crystallization conditions. The QD morphology is maintained upon capping. These results show that it is possible to introduce a detailed engineering of the DE-QD electronic properties, like electron state energies separation and electron-phonon interaction, via growth condition shape control. In fact, the QD shape can *a-priori* be designed on the basis of the droplet dimension and the expected diffusion length at the crystallization conditions, through the simple analytical relations. Furthermore, the chemical composition and the interfaces of these quantum dots is analysed in detail, giving insights in the crystallization process and its limitations. X-STM and Atom Probe Tomography data show that the fabrication of GaAs/AlGaAs QDs by Droplet Epitaxy is subject to phenomena altering the final dimensions and chemical composition of the QDs. Several processes are reported which may be connected to each other; local drilling of the substrate below the QD, interface broadening, Al intermixing and Ga depletion above high aspect ratio QDs. Preventing those phenomena is essential to keep the control of the QD morphology achieved by the fine tuning of the growth parameters. From this investigation, the key factors seem to be the temperature and the kinetics of the crystallization and the annealing steps. Understanding and controlling those is expected to allow for the suppression of these unwanted phenomena. Consequently, an effort has been made to achieve the precise height control of these GaAs/AlGaAs quantum dots by engineering the capping layer. The method used for that purpose, called flushing, resulted in a very promising and accurate control over the quantum dot height. The fundamental mechanism based on annealing, suggest here, was found to be similar to the case of SK-QDs. However the partial capping of the QDs depends on the diffusion processes and is hence expected to be material or composition dependent.

The investigations by STM of II-VI semiconductor structures are presented in chapter 6. The initial interest in analysis II-VI nanostructures was to study the incorporation of Mn impurities inside CdTe quantum dots. This system has been investigated thoroughly by means of optical spectroscopy but lack the structural characterization at the nanoscale. In this chapter, this exotic class of semiconductors which are the selenium and tellurium based II-VI semiconductors is first presented. Then, a study of the p-type doping of ZnTe achieved by introducing N atoms is presented, which was meant as first step towards the study of Mn doping of ZnTe. The complete absence of segregation or diffusion of N atoms incorporated in ZnTe in a temperature range of 300°C to 360°C is reported. However, the creation of a large number of point defects along with the incorporation of N in ZnTe is also revealed, which will strongly affect the electrical and transport properties of N-doped ZnTe crystals. Finally, a full study of CdSe/ZnTe and CdSe/ZnCdTe multiple quantum wells is presented, focusing on the quality of the interfaces. These specific systems are fabricated for their optoelectronics properties. The type-II band alignment expected in these multiple quantum wells structures should allow for the efficient absorption of light in a tunable energy range. This prospect are however dependent on the quality of the heterostructures and in particular of the interfaces. From the two X-STM studies presented here, it clearly appears that the growth conditions of CdSe determine the structural quality of the interfaces which do not share common anion or cations. The interfaces of the CdSe/ZnTe MQW with CdSe grown under excess of Cd appeared to be sharp and well-defined within one bilayer. The back-diffusion of Cd is clearly observed. Furthermore, the relaxation of the cleaved surface support the presence of Zn-Se and Cd-Te bonds respectively at the ZnTe/CdSe and CdSe/ZnTe interfaces. On the contrary, the CdSe/ZnCdTe interfaces grown under excess of Se are not abrupt. Te atoms are found to segregate from this interface. The segregation of Te might explain the non-periodic

RHEED oscillations observed at Se/Te interfaces grown under similar conditions. The mechanisms behind the creation of structural defects in Cd-rich growth condition and the segregation of Te in Se-rich growth conditions have not been determined. Consequently, it is suggested that the growth conditions for CdSe should be chosen according to the desired functionality of the heterostructure. If, like for short period superlattices, sharp interfaces are required, Cd-rich growth is much more suited. Whereas if a low defect density is necessary a Se-rich growth is expected to perform better.

Acknowledgements

The work presented in this thesis is not the result of the work and aspiration of a single person, but the achievement of large and diverse collaborations. For this reason, I would like to acknowledge every person that contributed directly to this work or supported my efforts.

First of all, I would like to thank my promotor and supervisor Paul Koenraad for giving me the opportunity to carry out my PhD project within his group. I am very grateful for the confidence and the freedom he gave me through the last four years. His expertise and enthusiasm have often paved the way to success. By his side, I learned not only physics but I also discovered the academic world.

My move to the Photonics and Semiconductor Nanophysics group in Eindhoven was instigated by the previous collaboration with the Semiconductor Nanophysics group at the CEA/Institut Néel in Grenoble during my final master project. I would like to thank Henri Mariette, my second promotor, for giving the opportunity to carry out my first two research projects on II-VI semiconductors nanostructures within his group. These two projects have been the most inspiring and have transformed my curiosity for solid-state physics into a strong interest for low-dimensional semiconductor structures. In this perspective, joining the PSN group in Eindhoven has been a great choice. I could not name a better place to investigate the different facets of semiconductors physics at the nanoscale scale. The variety of topics within my PhD project has been very stimulating.

I am extremely very grateful to all the persons I collaborated with in the last four years. Collaborating requires discipline. I would like to thank everyone for their professionalism and availability. Regarding the work on single impurities, I would like to warmly thank Michael Flatté and Victoria Kortan for their excellent theoretical work and their always valuable insights which have given a greater dimension to my experiments. It has been a pleasure to work with them. I would like to thank Bryan Gallagher and Richard Campion for providing us with exotic transition metal atoms in semiconductor samples. I enjoyed our meeting during the SemiSpinNet events as well as during my two months stay at the University of Nottingham. I have very good memories of this short stay. For that I would like to thank Andrew Rushforth and all the students I met at the faculty. I would like to thank Taakaki Mano and Stefano Sanguinetti for providing samples and sharing their knowledge about Droplet Epitaxy. I am very glad that I had the opportunity to work with the experts of this field. I would like to thank Lionel Gérard and Regis André for persevering in making II-VI semiconductors samples for me. I remember fondly our meetings in Grenoble and discussions about this always more complicated project. Finally, some projects not mentioned in this thesis included additional cooperation. I would like to thank Takashi Kita for the doped quantum dots samples and Bruce Wessels for the magnetic semiconductor layers.

I am very grateful to all committee members for reading my dissertation and providing valuable comments on their field of expertise.

I would like to thank everyone who daily or weekly supported my PhD project and myself. I was very pleased by the dynamism of the PSN group.

I have no doubt that my first circle of colleagues has had a strong influence on the progress of my PhD project. I am immensely grateful to Murat and Joris. I could not have wished better training to the STM world. With their absolutely different character, they taught me everything I needed to perform and analyse STM measurements, that is succeed in my PhD. I was very much inspired by their dedication to this work. I would like to thank all the other persons who allowed for a smoother running of the STM lab: Jens, Ineke, Samuel and Erwin. I enjoyed sharing technical and physics knowledge with them. I wish all the best to the new STM students: Davide, Rianne, Christian. Roommates have occupied a special place in my PhD world. In particular when they experienced it all. I would like to thank Joost for his constant interest and support to my projects. I felt lucky and enjoyed working at his side in the last four years.

Experimental physics research would be much more difficult without the presence of technically qualified persons. I would like to thank Frank, René, Rian, Jos, Peter and Martine for their support. It was nice to daily being able count on their practical skills. Technicalities can be your worse enemy, especially administrative ones. For helping with this matter, I would like to warmly thank the secretaries of group PSN. Margriet and Annebee as well as Thérèse-Anne and Simone. They made my life within the university much simpler. I wish I had not made their life more difficult.

The diversity in personality among my colleagues has been the most pleasant and entertaining. I would like to thank Milo for being like an old friend, Simone for the SEM images and being so positive, Alessandro for catalyzing the social life of the PhD students in the group, Döndü for the company during the late writing evenings, Sebastien for alone representing France and giving valuable advices. Coffee breaks have always been enjoyable moments thanks to many students: Erwin, Joost, Davide, Rianne, Rosalinda, Leonardo, Sartoon, Anthony, Thuy, Diana, Ikaros, Dick, Michele, Adam and all the others less present. In these moments, I also appreciated the diverse discussions with Andrei Silov, Rob van der Heijden, Erik Bakkers, Jos Haverkort and Andrea Fiore. I had the chance to share my projects with students and wish to thank them for their work and efforts: Steven on the nerve-racking LT-MFM project, and Guido very dedicated to the exciting Fe impurity project.

Because there is sometime a life next to the PhD project, I would like to say that I will have good memories of the evenings at the restaurant, at the cinema, at Milo's place or at the TUe with my colleagues and friends. I would like to thank Jelle for being a good friend and distracting me from the invading PhD projects. I mostly discovered the Netherlands through my sport activity. I fondly remember my table tennis team and training mates. I had a very good time training and competing with them around Eindhoven.

I would like to thank all my friends, who despite being hundreds of kilometer away have been supporting me: Pierre, Mylène, Loïc but also Georg and James. Keeping in touch with them has not always been easy. Nevertheless, the few moments together meant a lot to me. Most of them are now wandering towards new and further horizons. I wish them all the best and hope to see them again soon.

Un agradecimiento muy especial para mi familia Colombiana, que pesar de la distancia, siempre manifestó mucho interés en los momentos cruciales de mi tesis y estuvo atenta a mis avances. Enfin, un grand merci à ma famille la plus proche pour leur écoute et leur aide dans les moments de doute. Je remercie chaleureusement ma sœur Sofía et mes frères, Antonio et Andrés pour leurs encouragements durant toutes ces années. Finalement, je souhaite exprimer toute ma gratitude à mes parents pour leur amour et leur soutien inconditionnel durant toutes mes d'études.

List of publications

J. Bocquel, V. R. Kortan, M. E. Flatté and P. M. Koenraad. *Mapping the core states of a single Fe impurity in GaAs*. Under preparation.

J. Bocquel, T. Mano and P. M. Koenraad. *Precise height control of GaAs/AlGaAs Droplet Epitaxy Quantum Dots*. Under preparation.

L. Gérard, **J. Bocquel**, R. André, P.M. Koenraad and H. Mariette. *Towards sharp interfaces between zinc-blende CdSe and ZnTe: a structural and optical study*. Under preparation.

J. Bocquel, S. Bietti, J. G. Keizer, T. Mano, P. M. Koenraad, and S. Sanguinetti. *Precise Shape Control in GaAs/AlGaAs Droplet Epitaxy Quantum Dots*. Submitted for publication to Crystal Growth&Design.

S. Mauger, **J. Bocquel**, P. M. Koenraad, C. Feeser, N. Parashar, and B. W. Wessels. *Disorder in Mn doped InSb studied at the atomic scale by cross-sectional STM*. Submitted for publication to Physical Review Letters.

J. Bocquel, V. R. Kortan, R. P. Campion, B. L. Gallagher, M. E. Flatté and P. M. Koenraad. *Core state manipulation of single Fe impurities in GaAs by STM*. Physical Review B **87**, 075421 (2013)

J. G. Keizer, M. Bozkurt, **J. Bocquel**, P. M. Koenraad, T. Mano, T. Noda, K. Sakoda, E. C. Clark, M. Bichler, G. Abstreiter, J. J. Finley, W. Lu, T. Rohel, H. Folliot, and N. Bertru. *Shape control of QDs studied by cross-sectional scanning tunneling microscopy*. Journal of the Korean Physical Society **58**, 1244 (2011)

J. G. Keizer, M. Bozkurt, **J. Bocquel**, P. M. Koenraad, T. Mano, T. Noda, K. Sakoda, E. C. Clark, M. Bichler, G. Abstreiter, J. J. Finley, W. Lu, T. Rohel, H. Folliot, and N. Bertru. *Shape control of QDs studied by cross-sectional scanning tunneling microscopy*. Journal of Applied Physics **109**, 102413 (2011)

J. G. Keizer, **J. Bocquel**, P. M. Koenraad, T. Mano, T. Noda, and K. Sakoda. *Atomic scale analysis of self assembled GaAs/AlGaAs quantum dots grown by droplet epitaxy*. Applied Physics Letters **96**, 062101 (2010)

Not part of this thesis

T. Aichele, A. Tribu, G. Sallen, **J. Bocquel**, E. Bellet-Amalric, C. Bougerol, J. Poizat, K. Kheng, R. André, S. Tatarenko and H. Mariette. *CdSe quantum dots in ZnSe nanowires as efficient source for single photons up to 220 K*. Journal of Crystal Growth **311**, 2123 (2009)

Curriculum vitae

Juanita Bocquel
born 27st of September 1986 in Nantes, France

2009-2013	PhD student at the Eindhoven University of Technology, Photonics and Semiconductor Nanophysics group, The Netherlands.
2007-2009	Master of Sciences in Physics, Université Joseph Fourier, Grenoble, France. Master project at the Institut Néel, Semiconductor Nanophysics group, Grenoble, France. *Study of tellurium segregation during the epitaxy of the II-VI heterostructures.* Internship at the Institut Néel, Semiconductor Nanophysics group, Grenoble, France. *VLS growth of CdSe nanowires.*
2004-2007	Bachelor of Sciences in Physics, Specialization in Chemistry, Université de Nantes, France. Erasmus Programme, Rostock Universität, Germany.
1997-2004	High School La Colinière, Nantes, France.